Draft version April 28, 2022
Typeset using LaTeX **preprint** style in AASTeX631

In the Trenches of the Solar-Stellar Connection. VI. Total EclipSS

Thomas Ayres[1] and Derek Buzasi[2]

[1] *Center for Astrophysics and Space Astronomy, 389 UCB, University of Colorado, Boulder, CO 80309, USA; Thomas.Ayres@Colorado.edu*

[2] *College of Arts and Sciences, Florida Gulf Coast University, Fort Myers, FL 33965, USA; dbuzasi@fgcu.edu*

ABSTRACT

Ecliptic-poles Stellar Survey (EclipSS: 2018–2019) collected HST/COS 1150–1420 Å spectra of 49 FGK dwarfs at high Ecliptic latitudes. These regions are favored by the scanning programs of TESS (high-precision optical light curves) and eROSITA (repeated X-ray visits over a half-decade), which can provide vital ancillary support to explore high-energy "stellar activity." The present study is a follow-on, focused on new Chandra/HRC-I 0.1–2.4 keV, COS 1340–1720 Å, and TESS photometry of the ten FUV-brightest EclipSS members; but also including archival X-ray pointings and HST far-ultraviolet spectra of thirteen representative solar neighborhood FGK dwarfs, together with high-energy irradiances of the Sun, for context. The EclipSS dK + dM binary HD 41004 proved exceptional. The ultra-short TESS period (1.3 d) appears to be associated with the red dwarf secondary, possibly about to engulf a close-orbiting brown-dwarf companion. The current study describes the emission-line profiles of a high-resolution subset of the full sample, finding the non-Gaussian line shapes (sharper peaks, broader wings) and redshifts of $\sim 10^5$ K features to be remarkably independent of activity; quantifies X-ray and FUV "variability bias" based on several multiple-epoch campaigns; builds enhanced flux–flux diagrams (e.g., X-rays versus C IV) for the whole sample; dissects the total coronal radiative loss by wavelength (1–250 Å "hard to ultra-soft X-rays," 250–1150 Å "EUV," and 1150–1700 Å "FUV") as a function of activity; and constructs an associated "XUV" proxy flux to empirically test models of the convective turnover time, τ_c. The associated Rossby number, *Ro*, is closely aligned to terrestrial and cosmic magnetic dynamo theories, and offers the prospect of a one-parameter description of stellar high-energy activity (relevant, for example, to host-star ionizing fluxes impacting exoplanets).

Keywords: stars: activity — ultraviolet: stars — X-rays: stars — techniques: spectroscopic

1. INTRODUCTION

Preceding installments of the "Trenches" series (Papers I–V) were intended to set a broad context for our Sun among the more distant, more diverse, solar-type stars, especially in kilovolt soft X-rays ($T \sim$ 1–10 MK) and far-ultraviolet emissions (FUV: 1150–1700 Å: $T \sim 10^4$–10^5 K). These high-energy radiations are external manifestations of a magnetic engine—the dynamo—that operates deep inside the stellar interior (Parker 1970), but delivers magnetic flux to the stellar surface layers, ultimately energizing the decidedly non-classical corona, some hundred times, or more, hotter than the photosphere beneath. The best way to set a context for the current study is to review the results of the previous Series contributions, which flow naturally into the new "Total EclipSS" effort.

Paper I (Ayres 2020) presented solar X-ray (0.2–2 keV) and UV (1150–3200 Å) fluxes, collected by satellite irradiance instruments that view the Sun as a star, over a time frame encompassing 1.5 sunspot cycles (the declining half of Cycle 23 and all of Cycle 24). The solar trends were contrasted internally, as well as against equivalent long-term high-energy time series of the nearby Sun-like stars α Centauri A (G2 V) and B (K1 V). The solar/stellar fluxes were scaled by bolometric values[1], e.g., f_X/f_{BOL} for f_X, the observed X-ray intensity. Bolometric normalization compensates for the different sizes and distances of stars, and has been used throughout the Trenches series.

The solar trends of various important emission species were arrayed in "flux–flux" diagrams—scatter plots of pairs of normalized fluxes, for example hot coronal X-rays ($T \sim$ 1–2 MK for the Sun) versus cool chromospheric Mg II 2800 Å ($\sim$ 8000 K)—for which each measurement pair, representing a single x-y point in the diagram, was recorded at the same time, or as close to simultaneously as possible. Such flux–flux comparisons typically show power-law correlations between the different species, usually with hot tracers, like X-rays, displaying steep trends relative to cooler emissions, such as Mg II (in that example, the power-law index is $\alpha \sim 3$). In fact, many of the solar flux–flux tracks exhibited mild curvature, which had not been seen in previous, albeit cruder, stellar surveys (e.g., Ayres et al. 1995). The solar flux–flux relationships carry information, in a globally averaged sense, concerning how the heating of different "layers" of the outer atmosphere evolves with increasing activity. The fact that the trends are so systematic suggests that there are strong connections between the heating of different atmospheric layers under widely differing states of magnetic activity. Furthermore, the flux–flux power laws could be useful in the stellar context for estimating, for example, the strength of H I 1215 Å Lyα from an observed flux of, say, the Mg II 2800 Å hk doublet. Even in the nearest stars, Lyα—the brightest emission in the FUV and important in the ionization of planetary atmospheres—is strongly absorbed by interstellar atomic hydrogen, whereas the Mg II resonance features are much less affected (see, e.g., Youngblood et al. 2022).

The second part of Paper I extended the solar flux–flux comparisons to α Centauri A (G2 V) and B (K1 V) (hereafter AB), which are similar to the Sun in many respects; although the system is mildly metal-rich, probably a Gyr older than the Sun, and the G2 primary, which is 10 % more massive than the Sun, is further along its evolutionary trajectory. The stellar flux–flux trends showed good agreement between α Cen A and the Sun, both of which are similar in X-ray and FUV activity levels. The cooler K dwarf, α Cen B, is more active than the Sun, but generally its power laws followed extrapolations of the solar/α Cen A relations. There were a few notable differences, which later (e.g., Paper III and present Paper VI) were seen to be common among the later spectral types. The

[1] The bolometric flux, f_{BOL}, is the total stellar radiative output over all wavelengths, as measured per cm^2 at Earth.

solar-stellar comparisons suggested that the Sun is not unusual in its high-energy properties, at least within the small local circle of Sun-like stars.

Paper II (Ayres 2021b) extended the solar analysis of Paper I to the extreme ultraviolet wavelengths (EUV: roughly, 100–1150 Å), again utilizing irradiance instruments that view the Sun as an unresolved source, i.e., as a star. The EUV hosts a number of important emission lines from a wide variety of species including, especially, numerous stages of highly ionized iron. The dominant emissions in the solar EUV spectrum are He II 303 Å and C III 977 Å, both of which have counterparts in the FUV (He II 1640 Å and the C III 1175 Å multiplet)[2]. The EUV emissions, like H I Lyα in the FUV, are key sources of ionization and drivers of photochemistry in planetary atmospheres (e.g., Airapetian et al. 2020). Unfortunately, stellar EUV radiation is mostly hidden from view at Earth, blocked by interstellar atomic hydrogen absorption below the Lyman edge at 912 Å, even along the short sight lines to the nearest stars. Nevertheless, flux–flux correlations between solar EUV and FUV species, as derived in Paper II, can provide some guidance concerning how to scale the unseen EUV emissions of a star from the more easily observed FUV counterparts.

Paper III described the 2018–2019 Ecliptic poles Stellar Survey (EclipSS: Ayres 2021a), which collected moderate-resolution ($\lambda/\Delta\lambda \sim 18{,}000$) short-FUV (1150–1420 Å) spectra of 49 late-type FGK dwarfs, using the sensitive COS instrument on HST. The EclipSS targets were drawn from candidates in the North and South Ecliptic polar regions, because these areas were due to receive enhanced attention from then upcoming all-sky scanning missions TESS (Transiting Exoplanet Survey Satellite: Ricker et al. 2015; high-precision optical photometry to detect exoplanet occultations, but also stellar rotation periods and white-light flares) and eROSITA (Extended Roentgen Survey with an Imaging Telescope Array: Predehl et al. 2016; repeated X-ray visits over a half-decade to track coronal properties and variability), which could provide crucial ancillary information not easily obtained by other means. The EclipSS targets were vetted to ensure Main Sequence (MS) status and low-confusion surrounding star fields to simplify the interpretation of the relatively low-resolution TESS and eROSITA imaging. The EclipSS stars were restricted to a Gaia G-magnitude range suitable for COS, TESS, and eROSITA, but otherwise represented a minimally biased sample.

The short-FUV emission lines of the 49 EclipSS members were juxtaposed, again in flux–flux diagrams, to the comparable emissions of the Sun and α Cen AB (from Paper I). The EclipSS sample was not pre-selected by activity level (which was unknown for these distant, $d \sim$25–100 pc, mostly anonymous dwarfs); consequently the majority of the members were relatively inactive, like the Sun and its neighbor α Cen A, forming a cloud of points near the solar position in a flux–flux diagram. However, about 20 % of the sample were more active, transcending α Cen B at the peak of its magnetic cycle, and extending the power laws to higher normalized fluxes. Moreover, there was a more diverse collection of spectral types in the EclipSS sample than represented by the Sun and the α Cen twins, including several F-types, which are at the edge of convection, so to speak; and potentially have quite different modes of dynamo action than their cooler, more deeply convective G/K cousins. In this extended comparison—although limited to the short-FUV lines and excluding Lyα, which was too contaminated by geocoronal emission in the COS spectra—generally all the spectral types followed similar power laws, although there was the suggestion of slight separations

[2] The two He II transitions are, respectively, the Lyα and Bα equivalents for hydrogen-like singly ionized helium.

between the classes in some cases. The most active star of the sample was the K dwarf HD 41004. More on this, as it turns out, fascinating object later.

Paper IV (Ayres et al. 2021) returned to the Sun, to construct disk-average high spectral resolution ($\lambda/\Delta\lambda \sim 5{\times}10^4$) line profiles of key UV species—C II 1334 Å and 1335 Å, Si IV 1393 Å, and Mg II 2796 Å—from spatially resolved whole-Sun stigmatic spectral scans recorded by the Interface Region Imaging Spectrograph satellite (IRIS: De Pontieu et al. 2014) at different phases of the solar cycle. The aim was to explore how the various emitting regions on the solar surface print through to the spatial average, to help decode the unresolved UV line shapes of other stars. All three solar diagnostics showed a preference for the wide-spread cellular magnetic supergranulation pattern, more so for hotter Si IV than cooler Mg II (the latter has a significant contribution from transient intra-cellular shock waves, of non-magnetic origin). Notably, optically thin Si IV displayed a conspicuous bright ring around the edge of the Sun, whereas optically thick Mg II was suppressed at the limb by scattering. This behavior introduced a conspicuous "hook" in the spatially resolved Si IV versus Mg II flux–flux diagram at low Mg II intensities.

An intriguing finding was that although the variations in the disk-average line fluxes were relatively modest over the solar cycle (only a 50 % increase of Si IV 1393 Å from cycle MIN to MAX, most extreme of the three diagnostics), the spatially resolved line fluxes (in $2''{\times}2''$ bins) extended up to, and beyond, values seen in the disk-averages of very active G-type dwarfs (which can have Si IV normalized fluxes more than ten times the solar average). The conclusion was that parts of the Sun—the intense cores of active regions—mirror at a small scale the global behavior of Sun-like dwarfs at the extremes of magnetic activity. This finding could be useful for modelers, as well for developing, say, more robust EUV–FUV scaling laws applicable to the more active young suns (by appealing to the upper ends of spatially resolved solar flux–flux correlations).

A further significant finding was that the sub-Gaussian line shape of Si IV 1393 Å seen in the disk-average solar spectrum (namely, a more sharply peaked line core on top of broader wings compared to a pure-Gaussian), could be followed down to the finest $2''$ spatial scales in the IRIS mosaics. This behavior conflicted with earlier ideas that the non-Gaussian line shape could be a bi-modal combination of narrow and broad pure-Gaussian components arising in distinctly different, spatially separated kinematic environments, which nevertheless were blended together in the disk average. Instead, the sub-Gaussian line shape might be pointing to a pervasive non-Maxwellian process (e.g., Dudik et al. 2017) operating on small spatial scales (e.g., in magnetic knots of the supergranulation network), which prints up into the spatially averaged profile.

Paper V (Ayres 2021c) carried the high spectral resolution dissection of solar disk-average line profiles of Paper IV back to the stars; specifically α Cen AB, and a new addition, the nearby bright mid-F subgiant Procyon (α CMi A: F5 IV-V). All three stars had unique time series of UV spectra extending back as much as a decade, obtained by HST's high-precision Space Telescope Imaging Spectrograph (STIS), with superior resolutions of R = 45,000–100,000 in the FUV and 100,000 in the near-ultraviolet (NUV: 1700–3200 Å), especially for the Mg II h & k resonance doublet at 2800 Å (hereafter, hk). Procyon's $L_{\rm X}/L_{\rm BOL}$ index sits above that of the average Sun but below α Cen B's mean, indicating that the subgiant is in the lower tier of activity, but not at the bottom. Curiously, long-term time series of Procyon's coronal X-rays were remarkably flat. The highly stable coronal emissions of Procyon were all the more surprising given that α Cen AB and the Sun all show dramatic cyclical changes in $L_{\rm X}/L_{\rm BOL}$, reaching a factor of ten (MIN to MAX) in the solar case (in the 0.2–

2 keV reference X-ray band adopted in that study). The UV emissions of Procyon also were steady over the decade of intermittent monitoring by STIS, which—given the flat-line X-ray behavior—was not surprising since late-type stars tend to display much less variability in the UV than at higher energies.

On top of the odd flat-line X-ray behavior, Procyon exhibited a curious factor-of-ten deficiency in its X-ray emissions relative to subcoronal transitions such as C IV 1548 Å ($T \sim 1{\times}10^5$ K). However, Paper V demonstrated that Procyon's X-rays appeared to be normal compared to chromospheric ($T \lesssim 1{\times}10^4$ K) emissions like Mg II hk, so the X-ray deficiency could be an equally odd over-exuberance on the part of the 10^5 K subcoronal species. Given the rather unusual behavior of Procyon in X-rays and FUV emissions, one might be tempted to ascribe the energization of Procyon's outer atmosphere to an entirely different type of process than operates in cooler stars (acoustic wave heating was championed at one point in the past: Simon & Drake 1989). However, Paper V also showed that the shapes and Doppler shifts of the high-resolution FUV line profiles of Procyon were very similar to those of α Cen AB (and the Sun), which instead suggested that the energization mechanisms are very similar among these stars, spanning a significant range of surface temperature and gravity.

The current project is a follow-on to the original EclipSS survey of Paper III, now focusing on a subsample of the ten most active EclipSS targets, as gauged by FUV emission-line brightness. The observational objective was to obtain X-ray pointings by Chandra, using its HRC-I camera, and additional FUV coverage with COS (long-FUV: 1340–1720 Å), generally close in time to the HRC-I epochs. In parallel, TESS provided rotation periods for the subsample, based on the multi-sector light curve coverage achieved for these high Ecliptic latitude targets (a prime motivation for the original survey). As will be shown later, the near continuous coverage over many TESS 27-d sectors was crucial, even for stars with rotation periods of only a few days. One of these follow-on objects, HD 41004, proved to be rather unusual, as described in more detail later.

Several additional candidates (the "Related" objects) were combined with the EclipSS subsample to fill out the G spectral types, in keeping with the general focus of the Trenches series on Sun-like stars. The additional targets were related in the sense that they have existing X-ray and full-coverage FUV measurements, in most instances in at least two separated epochs; and also have reliable rotation periods, mainly from long-term monitoring of chromospheric Ca II H & K emission (near 3950 Å; hereafter HK).

A set of "Reference" late-type stars was also added: α Centauri AB and Procyon, all recorded for a decade, or more, in X-rays by Chandra HRC-I and in the FUV by STIS; ξ Bootis A (G7 V) and B (K5 V) and 70 Ophiuchi A (K0 V) and B (K4 V), by HRC-I and COS in a recent multi-year joint Chandra/HST campaign; and finally ϵ Eridani (K2 V), captured by XMM-Newton in the X-rays, and STIS and COS in the FUV, also over several-year timescales commensurate with the short few-year activity cycle of this iconic, debris-disk, planet-hosting K dwarf (Coffaro et al. 2020). All eight Reference stars had sufficient multi-year coverage to at least crudely assess X-ray and FUV variability, on time scales relevant to their analogs of the 11-year magnetic sunspot cycle. The Sun was included as the ninth member of the Reference group based on X-ray and FUV irradiance measurements ("Sun as a star") during recent Cycle 24.

One important departure of the present work relative to the previous contributions of this Series was the adoption of an extended X-ray reference bandpass, 0.1–2.4 keV (5.2–125 Å), compared to

the previous 0.2–2 keV (6.2–62 Å). There were historical reasons to prefer the latter over the former, but a more compelling motivation in the current study was to have a broader, more inclusive, X-ray energy band to more carefully account for the overall coronal radiative energy losses. This issue will be discussed in more detail later.

The current study describes the behavior of the high-resolution STIS line shapes as a function of FUV activity; presents variability assessments of those targets with multi-year coverage; and constructs enhanced flux–flux diagrams, including X-rays, compared with the previous EclipSS effort, which was limited just to the short FUV. Further, armed with rotational periods for the carefully selected and uniformly observed X-ray and FUV sample members, it was possible to empirically test several proposed models of the convective turnover time versus effective temperature, relevant to distributions of activity parameters against the Rossby number, more closely aligned to magnetic dynamo theories than either the rotational velocity or the rotation period on their own. In fact, the systematic behavior of the X-ray plus EUV/FUV fluxes in the Rossby system offers a potential way to achieve a one-parameter characterization of the high-energy emissions of a late-type star, relevant, for example, to broad surveys of the impacts of host-star ionizing fluxes on orbiting exoplanets (see, also, Johnstone et al. 2021).

2. OBSERVATIONS

2.1. *The Stellar Players*

The main objective of the original EclipSS project was to obtain reference FUV spectra of a moderately large sample of late-type stars, near solar type, to prepare for ancillary information forthcoming from missions like TESS (optical photometry) and eROSITA (X-rays), which had not yet been launched when the original HST proposal was submitted. The all-sky planet-hunter TESS was especially anticipated, because the broad-band optical light curves of cool stars can display modulations, often subtle, due to surface magnetic activity, best known from the example where dark starspots rotate into and out of view (mimicking planetary transits, but on longer time scales). In fact, the main source of optical variability for low-activity stars like the Sun are the spatially extensive plage areas that normally surround the starspots (together forming "active regions") and which are slightly brighter than the ambient photosphere in visible light, especially near the limb.

As mentioned earlier, the choice of targets at high Ecliptic latitudes enhances the photometric coverage by TESS (and also eROSITA), owing to the layout of the TESS cameras and the 27-d stepped Sun-synchronous observing strategy (eROSITA is similar, although with a more traditional continuous great-circle scanning program, precessing 1° per day, like the predecessor ROSAT all-sky survey (RASS: Voges 1993) in the early 1990s). As described later, the longer duration TESS stares on the EclipSS targets are valuable to distinguish between the fundamental rotation period, and any harmonics, and to extend sensitivity to longer rotation periods beyond the grasp of a single 27-d sector. Furthermore, sometimes the rotational modulations are more obvious than at other times, thus the longer the photometric series, the better the chances of catching the source when it is "on."

The central aim of the new project was to obtain baseline coronal X-ray measurements with Chandra, coinciding with the initial eROSITA operations, and additional FUV coverage with HST/COS, to build on the original survey. The top ten targets of EclipSS, in terms of FUV brightness, were chosen for the new effort, and preliminary rotation periods were derived from the TESS sectors available at the time of the joint Chandra/HST proposal.

However, the ten stars of the EclipSS subsample were viewed as insufficient, in numbers, for the contemplated broader "Total EclipSS" effort. A prime consideration was that any comparison of high-energy properties of stars versus their rotation rates can suffer from ambiguities associated with poorly known stellar variability, especially if the available material was collected in only a single, or a few, epochs. Such variability can arise simply from the rotational modulations of surface activity alluded to earlier, long-term changes connected to a magnetic cycle, or transient events such as flares. Without an understanding what that variability might be like for certain classes of stars, it would be difficult to craft a convincing story concerning the high-energy rotation-activity connection, or any other such correlations.

One way to estimate the high-energy variability of a star, or group of stars, is rather brute-force, but effective; namely, to obtain long-term time series of X-ray and/or FUV emissions; analogous to what was done by O. C. Wilson, and successors, at the Mt. Wilson Ca II HK "chromospheric cycles factory" (Wilson 1978). This, nevertheless, is a challenging prospect for space observatories such as Chandra or HST, for which observing time is highly competed and annual peer reviews are ill-suited for sustaining long-term efforts. Despite the obstacles, several late-type stars, as described below, have been captured over time scales up to a decade, or more, jointly by Chandra and HST, in coronal soft X-rays and sub-coronal FUV emissions, respectively; and similar efforts have been carried out, although exclusively in X-rays, by XMM-Newton (e.g., Favata et al. 2008; Robrade et al. 2012; Orlando et al. 2017; Coffaro et al. 2020). The most valuable multiple observations would span at least one starspot cycle, and ideally more than one.

The second way to assess stellar high-energy variability is less direct, but in some ways more practical; namely, to accumulate one-off observations of a large number of stars with ostensibly similar rotational properties, and allow the natural variability of the individual objects to emerge through the sample standard deviations of the various diagnostic fluxes. To be commensurate with the EclipSS subsample, targets in this category should also have well-determined rotation periods (e.g., from HK surveys). Ideally, targets would be found that had more than one X-ray or FUV measurement, but perhaps not enough to qualify for the "Cycles" group highlighted earlier.

Table 1 summarizes fundamental properties of the ultimately selected program stars for Total EclipSS. The initial ten entries are the FUV-active subsample of the original EclipSS survey, which have, now, two epochs of FUV spectroscopy with HST/COS, reliable rotation periods from multiple TESS sectors, and an X-ray pointing by Chandra, often contemporaneous with the COS observation.

The second group, the Related objects, is a set of five G-type dwarfs that have Ca II HK rotation periods (considered the gold standard here), as well as corroborating $v \sin i$ measurements; one or more high-quality FUV spectra from HST (COS and/or STIS); and at least two coronal X-ray measurements (one typically from the RASS; the other from XMM-Newton or Chandra). The Related objects fill out the EclipSS subsample in terms of Sun-like stars, the major focus of the Trenches series.

The third group, the Reference sample, is a somewhat motley collection of nine very nearby bright stars, including the Sun, which have been subjected to multiple observations in the X-rays and FUV, in some cases for more than a decade; and which also have reasonably secure rotation periods, either through historical (or contemporary in one case) HK monitoring, or accurate $v \sin i$ measurements together with knowledge of the likely spin-axis orientation (e.g., from a binary orbit). As alluded above, the role of the Reference sample is to demonstrate the degree of temporal variability in FUV

emissions and coronal X-rays that arbitrary dwarf stars might experience. This historically poorly known "activity variability bias" has long been a major thorn in large-scale surveys that attempt to link high-energy emission properties of Sun-like stars to auxiliary parameters such as rotation period or age, because it could not be known whether any dispersion of the single-epoch fluxes around a mean trend was due to single observations drawn from a distribution of time-variable samples, or whether the underlying functional relationship with respect to the ancillary parameter has its own intrinsic fuzziness (for example, because the true correlation is multivariate).

Table 1. Summary of Stellar Properties

HD Num	Alt. Name	Type	d	G	$(BP-RP)$	$\upsilon_{\rm R}$	$T_{\rm eff}$	$\log g$	[Fe/H]	$f_{\rm BOL}$
			(pc)	— (mag) —		(km s^{-1})	(K)	(cm s^{-2})		(10^{-8})
1	2	3	4	5	6	7	8	9	10	11
EclipSS Subsample										
24636	TIC 238196350	F3	57.1	7.038	0.530	+14.6	6770	···	···	3.58
38459	TIC 235066737	K1	37.1	8.294	1.003	+26.5	5270	4.5	+0.2	1.18
39755	TIC 149631289	F2	81.2	7.752	0.533	+2.0	6760	···	···	1.85
41004[a]	TIC 219152539	K1	39.0	8.408	1.084	+42.5	5080	4.4	+0.2	1.10
62850	TIC 340459410	(G0)	32.9	7.041	0.785	+17.9	5880	4.4	···	3.57
150706	TIC 159511543	G0	28.2	6.870	0.776	−17.1	5900	4.5	···	4.17
156559	TIC 198407592	F2	81.6	7.794	0.548	−18.0	6700	···	···	1.78
172669	TIC 229738635	(G0)	36.0	7.428	0.791	−6.8	5860	···	···	2.50
180712	TIC 243278327	F8	45.1	7.835	0.770	−13.5	5920	4.4	···	1.71
185239	TIC 275626011	(F5)	81.6	8.046	0.600	+11.0	6500	···	···	1.41
Related objects (G-type dwarfs)										
10700	τ Cet	G8	3.65	3.300	1.051	(−16.6)	5080	4.6	−0.5	123
20630	κ Cet	G5	9.28	4.656	0.859	+19.2	5650	4.5	+0.1	32.5
39587	χ^1 Ori	G0	8.70	4.242	0.796	−15.5	5840	4.5	···	47.0
72905	π^1 UMa	G1	14.4	5.499	0.804	−13.0	5820	4.6	···	14.8
129333	EK Dra	(G5)	34.4	7.524	0.873	−21.5	5610	4.5	+0.1	2.32
Reference sample										
···	Sun	G2	···	−26.91[b]	0.82[b]	+0	5772	4.438	+0.08[b]	···
22049	ϵ Eri	K2	3.22	3.466	1.140	(+16.4)	4930	4.6	−0.1	108

Table 1 *continued on next page*

Table 1 *(continued)*

HD Num	Alt. Name	Type	d	G	$(BP-RP)$	$\upsilon_{\rm R}$	$T_{\rm eff}$	$\log g$	[Fe/H]	$f_{\rm BOL}$
			(pc)	— (mag) —		(km s^{-1})	(K)	(cm s^{-2})		(10^{-8})
1	2	3	4	5	6	7	8	9	10	11
61421 A	α CMi A[c]	F5	3.51	···	(0.567)	[+5.0±0.4]	6560	4.0	+0.00	1790
128620	α Cen A	G2	1.338	···	(0.813)	[−21.5±1.0]	5800	4.3	+0.24	2718
128621	α Cen B	K1	1.338	···	(1.021)	[−23.9±1.6]	5230	4.5	+0.22	899
131156 A	ξ Boo A	G7	6.75	4.480	0.925	+1.5	5450	4.6	−0.2	39.1
131156 B	ξ Boo B	K5	6.75	6.430	1.518	+2.3	4220	5.0	−0.2	9.08
165341 A	70 Oph A	K0	5.11	3.987	1.004	(−9.7)	5250	4.5	···	62.7
165341 B	70 Oph B	K4	5.11	5.539	1.486	(−10)	4300	4.7	···	19.9

NOTE—Values for the EclipSS stars were updated from Paper III based on Gaia Early Data Release 3 (EDR3)[3]. Col. 3 spectral types are from SIMBAD, except for a few cases (parenthetical values) for which the SIMBAD types were inconsistent with the Gaia $(BP-RP)$ colors, and new types were estimated from the latter: see Paper III. Col. 4 distances are from Gaia parallaxes (or in some cases Hipparcos). Col. 5 G magnitudes and Col. 6 $(BP-RP)$ colors are from Gaia EDR3 (except for the bright stars not in Gaia, for which values were estimated). Col. 7 radial velocities mainly are from Gaia (DR2), with a few exceptions originating from SIMBAD (parenthetical values) or STIS FUV chromospheric emission lines (square brackets). Values for ξ Boo and 70 Oph refer to specific epochs or time ranges (e.g., Gaia DR2): the radial velocity amplitudes amount to several km s^{-1} for both binaries, over the century-long orbits. Col. 8 lists effective temperatures from Paper V for the Sun, α Cen AB, and Procyon; and from a $T_{\rm eff}-(BP-RP)$ transformation (Casagrande et al. 2021) for the remaining stars. Col. 9 surface gravities and Col. 10 metallicities were aggregated from SIMBAD compilations, if available. Col. 11 bolometric fluxes are in erg cm^{-2} s^{-1}, from Paper V for α Cen AB and Procyon, and based on a revised version of eq. A1 of Paper III (see note (b), below) for the other stars using the updated EDR3 magnitudes and colors (latter determines the effective temperature upon which the bolometric correction described in Casagrande & VandenBerg 2014 was based).
[a] Binary (Hipparcos: 1991 epoch): position angle= 176°; separation= 0.54″; $\Delta Hp = 3.68$ mag. The secondary is an early-M Main sequence star, orbited by a $\sim 19 M_{\rm J}$ brown dwarf with a 1.3 d period (Santos et al. 2002).
[b] $G_\odot = -26.907\pm0.006$ mag; $(BP-RP)_\odot = 0.815\pm0.018$ mag (Casagrande et al. 2021); ${\rm BC}_\odot = +0.081\pm0.003$ (based on Casagrande & VandenBerg 2014); $(f_{\rm BOL})_\odot = 1.361\times10^6$ erg cm^{-2} s^{-1} at 1 AU; $(f_{\rm BOL})_\star = (2.53\pm0.02)\times10^{[-(G_\star+{\rm BC}_\star)/2.5]}$ erg cm^{-2} s^{-1} at Earth.
[c] Procyon: F5 IV–V (+DZQ).

Some comments concerning specific objects are in order. Most of the EclipSS subsample are relatively anonymous 7th–8th magnitude field stars, without any special characteristics worth mentioning (unlike the much closer Related objects and Reference sample whose proximity has inspired numerous in-depth studies of their properties, circumstances, and environments). The one exception is HD 41004, as described next. Comments on the Related and Reference members follow.

HD 41004, in the EclipSS subsample, is a hierarchical multiple system consisting of an early-K primary, orbited by a Jovian-mass planet with a 2.6 yr period (Zucker et al. 2004); and an early-M secondary, 3.7 (H_p) magnitudes fainter with a current (circa 2022) separation of only 0.″2 (according to the ephemeris in the Sixth Catalog of Orbits[4]). The red dwarf has a brown dwarf (BD) companion

[4] See: http://www.astro.gsu.edu/wds/orb6/orb6ephem.html .

in a tight orbit with a short, 1.3 d period (Santos et al. 2002, Zucker et al. 2003). The dM + BD pair has, by far, the largest tidal interaction parameter in the Scharf (2010) study of 29 star-planet systems, thanks to the large mass of the BD ($\sim 19 M_{\rm J}$) and the small orbital separation ($\sim 7\,R_\star$ for the small M dwarf). See Ayres & Buzasi (2021) for additional comments on HD 41004. Further discussion will also be presented later, when the TESS light curves for the EclipSS subsample are introduced.

Tau Ceti, first of the Related objects, is a nearby ($d \sim 4$ pc), iconic, low-activity, metal-poor late-G dwarf; 1 Gyr, or more, older than the Sun. The activity properties of τ Cet have been discussed at length by Judge et al. (2004). Tau Cet has a relic debris disk, although much less massive than that of ϵ Eri (see below), and a retinue of planets, perhaps as numerous as the Sun's. Although τ Cet is classified as late-G, its Gaia colors are more like that of an early-K. Possibly the MK classification was affected by the 0.5 dex metal deficiency. Tau Cet is important to the present study as an anchor at the low side of the activity distribution, falling just below the average $L_{\rm X}/L_{\rm BOL}$ of the Sun and α Cen A, but several tenths of a dex lower in some of the line emissions (particularly the Si series), probably partly due to the reduced metallicity of the star.

Kappa Ceti is a solar-neighborhood ($d \sim 9$ pc) mid-G dwarf, somewhat cooler than the Sun. It has solar metallicity and an age of a few hundred Myr. Over the next 4 Gyr, κ Cet will slowly evolve to solar temperature. There is a faint companion about $4'$ away. Kappa Cet has been a popular target of the "Sun in Time" program (e.g., Güdel et al. 1997, and references therein), because of its status as an analog of the young Sun.

Chi^1 Orionis is at the same distance ($d \sim 9$ pc) as κ Cet, and like HD 41004 has a dim M-dwarf companion, with a current speckle-measured separation of $0.''5$, a period of 14 yr, $\Delta H_p \sim 3.2$ mag, and an estimated mass of $0.15\,M_\odot$ (König et al. 2002). If the dM companion has a normal activity level for its age (few hundred Myr) and mass, it would not be expected to contribute significantly to the X-ray and FUV luminosity of the system, outshined at high energies by its larger active partner. Chi^1 Ori is another prized young (few hundred Myr) analog of the Sun, potentially shedding light on the high-energy irradiation of planets in our own Solar System during the period prior to the Late Heavy Bombardment (at ∼600 Myr). However, χ^1 Ori will eventually evolve to a hotter temperature than the Sun, achieving a spectral type of late-F on the mid-life Main sequence. Chi^1 Ori has close to solar metallicity.

Pi^1 Ursa Majoris is another young-Sun analog, somewhat further away ($d \sim 14$ pc) than χ^1 Ori, but similarly active in X-rays and the FUV. Pi^1 UMa, lacking stellar companions, has the advantage of a cleaner object; but the fainter fluxes relative to χ^1 Ori, owing to the larger distance, is somewhat of a disadvantage. Nevertheless, at least in the FUV, π^1 UMa can be observed in HST's Continuous Viewing Zone (CVZ). The increased integration time during the un-occulted orbits can compensate for the lower flux levels. Pi^1 UMa has near-solar abundances.

EK Draconis is more distant than the other Related objects, at $d \sim 34$ pc, but is important to the present study to anchor the high side of the activity distribution. EK Dra is thought to be Pleiades

age (120 Myr), although some authors have argued that the fast rotation of the G dwarf, and its high activity level, point to a younger age, 50–70 Myr. However, the rotation-age-activity relation can be broken at young ages, where a much larger dispersion in intrinsic spin periods is found than at older ages, because the birth conditions of the stars have not yet been fully erased by the negative feedback of coronal wind breaking (see, e.g., Ayres 1997, and references therein). Like a number of the previously described stars, EK Dra has a faint M-dwarf companion, in this case with a 45 yr highly eccentric orbit, attaining an apastron of 0.″8 and a periastron of 0.″2 (König et al. 2005). The primary has a mass of 0.9 $M_{\odot}$ and the secondary, 0.5 $M_{\odot}$. The secondary is several magnitudes fainter. The secondary was accidentally recovered in a deep-exposure HST/STIS CCD acquisition image taken in 2014, a few years after the predicted apastron, with a separation and position angle as expected from the König et al. ephemeris (see Ayres 2015). In the latter time-domain study, the secondary was excluded from the small 0.″2×0.″2 slot used in an initial part of the program involving STIS (taking advantage of the high wavelength precision of that instrument), but was inside the larger 2.″5-diameter COS aperture for the second part of the program, which covered key phases of the 2.7 d rotational period with four high-sensitivity pointings. The M-type secondary was not clearly visible in any of the COS FUV spectral images, consistent with predictions of a negligible contribution based on young stars similar to EK Dra A and B (Ayres 2015). EK Dra displayed a conspicuous FUV flare decay during the first COS pointing only a half-hour after the end of the initial STIS observation, due to a "superflare" outburst between the two closely spaced visits. Nevertheless, the initial STIS observation and three COS pointings after the first COS visit, spaced over the ensuing ∼40 hr, were remarkably constant in their FUV flux levels. Like τ Cet, the Gaia colors of EK Dra are redder than expected for the G2 classification. Namekata et al. (2021) have described recent superflaring activity of EK Dra, captured by TESS as well as ground-based observatories.

The Sun, α Centauri AB, and Procyon have been key players in the Trenches series, and constitute the main part of the Reference sample. Their parameters were taken from Paper V, where also an extensive discussion of the fundamental properties of Procyon was presented. There were reports of a Habitable-Zone planet in orbit around α Cen B (Dumusque et al. 2012), but the claim was challenged on the basis of systematic effects introduced by the impact of the K star's activity on the radial velocity (RV) time series (Rajpaul et al. 2016). The α Cen binary of very bright, very close stars (6″–10″ separation in the current decade) is especially inimical to direct planetary imaging. Further, the Doppler-reflex technique similarly is disturbed by scattered-light interference from the B component during RV spectroscopy of A (and vice versa). The α Cen system is metal-rich compared to the Sun by about 0.2 dex, whereas Procyon is solar-normal. Alpha Cen A is 10 % more massive than the Sun, α Cen B is 10 % less massive, and Procyon is 50 % more massive. The Alpha Cen system likely is older than the Sun, by perhaps 1 Gyr, and the A component is slightly more evolved than the Sun. Procyon is much younger (age∼2 Gyr) than the Sun, but nevertheless has moved beyond the Main sequence into the initial subgiant branch thanks to its higher mass, and thus faster nuclear evolution.

Epsilon Eridani ($d \sim 3.2$ pc) is slightly closer than Procyon, and is the second brightest K dwarf (after α Cen B, which is similar in spectral type, but significantly older). Epsilon Eri is more active

than α Cen B, displaying an intense, rich emission-line spectrum in Chandra Low-Energy Transmission Grating Spectrometer (LETGS) images (Ayres 2014). The apparent coronal temperature, $\sim$4 MK, is hotter than those of Procyon and α Cen B (at its activity cycle peak), which both are $\sim$2 MK. Epsilon Eri has a well-known debris disk, generally a signature of youth ($\sim$ 500 Myr), and a confirmed planetary companion in a seven-year orbit, well outside the Habitable Zone. The metallicity of the K dwarf is slightly less than solar, although the reported values might be affected by the enhanced magnetic activity of the young star.

Xi Bootis is a solar-neighborhood ($d \sim 7$ pc) binary with a late-G primary and mid-K secondary. The orbit is eccentric ($e \sim 0.5$), with a period of 152 yr. The AB separation on the sky varies between 2.″1 and 7.″3. The secondary currently (for the 2020–2030 decade) is midway between apastron and periastron, at a separation of 4″–5″. The masses of the components are $0.90\,M_\odot$ and $0.66\,M_\odot$. The age of the system is estimated to be a few hundred Myr, and the metallicity is essentially solar.

70 Ophiuchi is another solar-neighborhood visual binary. At $d \sim 5$ pc, it is even closer than ξ Boo. The primary is slightly later than ξ Boo A, with spectral type K0; while the secondary, at K4, is slightly earlier than ξ Boo B. The orbit is similarly eccentric, with a period of 88 yr. The AB separation varies between 1.″5 and 6.″8, with B currently (for the 2020–2030 decade) near apastron. The masses of 70 Oph AB are very similar to those of ξ Boo: $0.89\,M_\odot$ and $0.73\,M_\odot$. The system age, based on the Ca II HK indices, is about 2 Gyr, significantly older than ξ Boo, but less than half the age of the Sun or α Cen AB. Abundances are solar.

The Total EclipSS sample is illustrated in Figure 1 in a Hertzsprung-Russell (H–R) diagram, on top of PARSEC evolutionary tracks (Bressan et al. 2012). The original EclipSS stars, minus the subsample, are the smaller gray circles, while the subsample members are indicated in colors as well as external dark plus signs (red to highlight the special case of HD 41004). The five Related G-types are unadorned yellow circles (orange for G8 τ Cet). The Reference stars are larger, annotated circles (see legend at upper right). The gray shaded band is the Zero-Age Main Sequence (ZAMS) on the lower edge and the 50 % MS lifetime on the upper edge. Solid curves are MS and post-MS evolutionary tracks beginning at $1\,M_\odot$ (the Sun is marked by $\odot$, partly hidden), marching toward hotter temperatures in increments of $0.1\,M_\odot$. Dashed curves are pre-MS Hayashi tracks beginning again at the Sun, then dropping toward the cooler temperatures in increments of $0.1\,M_\odot$. All the Total EclipSS symbols are color-coded by spectral type according to the legend at lower left.

2.2. *X-ray Observations*

2.2.1. *Energy Range Considerations and Emission-Measure Models*

One important departure of the present work relative to the previous contributions of this Series is the adoption of an extended X-ray reference energy bandpass, 0.1–2.4 keV (5.2–125 Å), compared to the 0.2–2 keV (6.2–62 Å) utilized earlier. There were historical reasons to prefer the latter over the former, specifically the ROSAT mission in the 1990's, for which the broader band was the default "full energy range," quoted, for example, for the RASS detections, but the narrower band was chosen

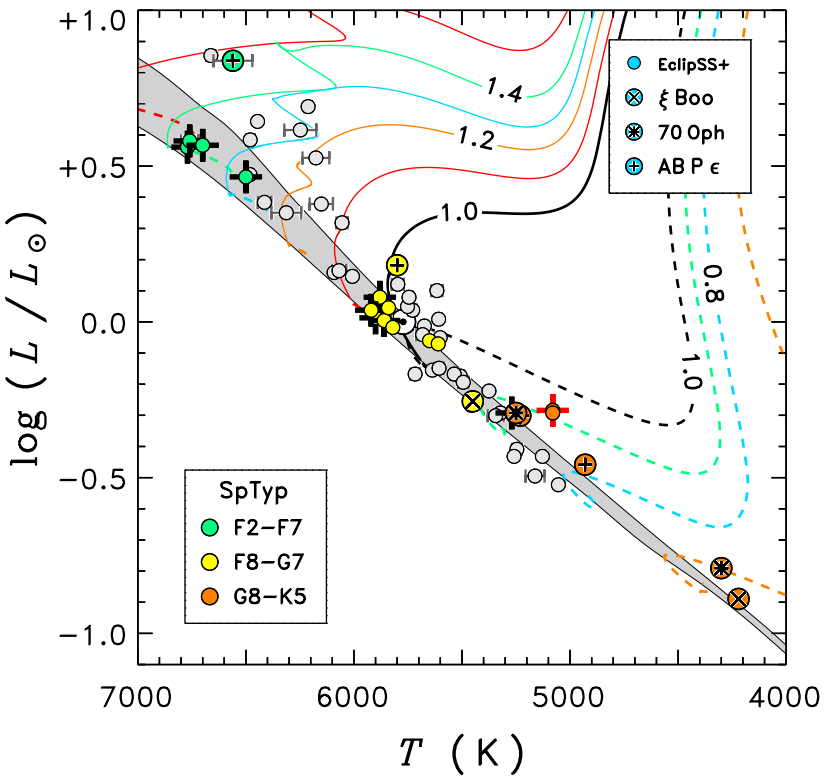

Figure 1. H–R diagram of the Total EclipSS sample. Gray shaded band is the ZAMS along the lower edge and the 50 % MS lifetime along the upper edge. Solid curves are MS/post-MS evolutionary tracks, beginning at the Sun, and extending to hotter temperatures in steps of 0.1 $M_{\odot}$ (annotations are $M/M_{\odot}$). Dashed curves are pre-MS Hayashi tracks, shown for the Sun and several lower mass models. Sample members are color-coded by spectral type according to the legend at lower left. In the legend at upper right, "EclipSS+" refers to the original EclipSS sample (the subsample dots are in colors with external dark ticks; the other EclipSS members are gray) plus the five Related G-type dwarfs (unadorned, but color-coded dots). For the Reference sample, ξ Boo and 70 Oph are self-explanatory; "AB"= α Cen; "P"= Procyon; and "ϵ"= ϵ Eri. The Sun is marked by an $\odot$ symbol, partly obscured by several of the other points.

for one of the important derivative catalogs—the WGACAT[5]—to eliminate the lowest and highest pulse-height channels of the main ROSAT detector—an imaging proportional counter (PSPC)—which were less well calibrated than the interior channels 24–200 (corresponding to 0.24–2 keV, or 6.2–52 Å). Nevertheless, the Chandra HRC-I camera, used extensively in this work, has good soft response up to, and beyond, 100 Å. A key goal of the present study was to identify the major sources of atmospheric high-energy radiative losses associated with stellar surface magnetic activity, consequently extending the X-ray bandpass to lower, and higher, energies to obtain better coverage of the spectral distribution was a natural choice. In particular, the specific energy range can strongly affect the comparison of stars of Sun-like low activity (that have soft X-ray spectra with a significant 62–125 Å contribution) to the more active G-type dwarfs, with harder spectra for which the 62–125 Å part of the total is minor. This can be demonstrated quantitatively as follows.

[5] see: https://heasarc.gsfc.nasa.gov/W3Browse/rosat/wgacat.html

Wood et al. (2018) have published model Emission Measure Distributions (EMD), which describe the basic coronal plasma properties as a function of temperature[6], for a series of reference X-ray surface flux densities (F_X in erg cm^{-2} s^{-1} at the star)[7] as a proxy for the coronal radiative power. The study was based on a careful analysis of high-quality energy-resolved Chandra LETGS spectra of about twenty late-type dwarfs (several of which are in common to the present project).

Figure 2 illustrates the Wood EMD models, normalized to their peak values. (In reality, the absolute levels of the EMDs increase rapidly with increasing $\log F_X$: see Wood et al.) The tabulated Wood models are for $\log F_X = 4.0$–7.5 in steps of 0.5 (curves highlighted in blue). The EMDs typically show multiple components, with the main, lowest temperature, peak migrating systematically to higher temperatures with increasing F_X; and with the more minor, higher temperature bumps also moving in concert to higher temperatures, and in some cases proliferating. An additional EMD was extrapolated for $\log T = 3.75$ K to accommodate the low-activity, cool-corona dwarf τ Cet. Further, the coarse grid of EMDs were interpolated onto the intermediate values (steps of 0.25) to aid in the various convolutions described below. The intermediate EMD curves are highlighted in red.

In the current study, the EMDs play a primary role in the calculation of source-specific Energy Conversion Factors (ECF: the X-ray flux is the product of the ECF and the observed background-corrected count rate) for the various X-ray instruments, by a convolution of temperature-dependent ECFs with the relative EMDs for the $\log F_X$ appropriate to the target star. An important secondary role is to calculate source-specific flux ratios between different energy bands, for example 0.1–2.4 keV versus 0.2–2 keV, again through a convolution of temperature-dependent ratios and the relative EMDs.

Each temperature-dependent point on the ECF "test function" relation is yet another convolution, now between an energy-resolved spectrum calculated from a plasma emission model at a specific $\log T$, correcting for interstellar extinction if appropriate (i.e., to obtain the "unabsorbed" flux), and the energy-dependent effective area (response function) of the instrument in question over a specified energy band (the response is unity for the simple flux ratios). These various test functions can easily be derived for specific instruments using the WebPIMMS tool[8] or equivalent X-ray spectral synthesis (e.g., Ayres 2014).

Figure 3 depicts several of these test functions. The left panel illustrates energy band flux ratios. The red-outlined curve refers to the (0.1–2.4 keV) / (0.2–2 keV) ratio. Note the steeply rising values toward the lower temperatures reflecting the increasing importance of the 0.1–0.2 keV interval for the softest sources (like the Sun), which contains a forest of emissions from the iron and nickel M-shells. This was a prime motivation to adopt the broader energy band as the reference for the Total EclipSS stars. At higher temperatures, the ratio bottoms out and begins to rise slowly to the right, in response to the increasing contribution from the 2.0–2.4 keV band, which contains mainly emissions from high ionization stages of heavy elements. The blue-outlined symbols (same as red curve up to $\log T \sim 7$, but falling below at higher temperatures) is the flux ratio of 0.1–2.4 keV versus 0.2–12 keV. This ratio is relevant to converting XMM–Newton catalog fluxes (4XMM-DR11[9], "ep8 band") quoted in

[6] The "stellar" volume EMD defined by Wood et al. is the logarithmic temperature derivative of the volume integral of the squared electron density. The flux of, say, a given line transition then, schematically, is an integral over $\log T$ of the EMD times a contribution function that involves ionization ratios, the elemental abundance (which might be altered in the corona by chemical fractionation effects), and the thermal excitation of the transition.

[7] F_X and f_X/f_{BOL} are closely related: $F_X = \sigma\, T_{eff}^4\, (f_X/f_{BOL})$, where σ is the Stefan-Boltzmann constant. The effective temperature factor, T_{eff}^4, varies by 0.8 dex from mid-K dwarfs to early-F dwarfs, whereas both F_X and f_X/f_{BOL} span at least 4 dex.

[8] see: https://cxc.harvard.edu/toolkit/pimms.jsp

[9] see: https://heasarc.gsfc.nasa.gov/W3Browse/xmm-newton/xmmssc.html

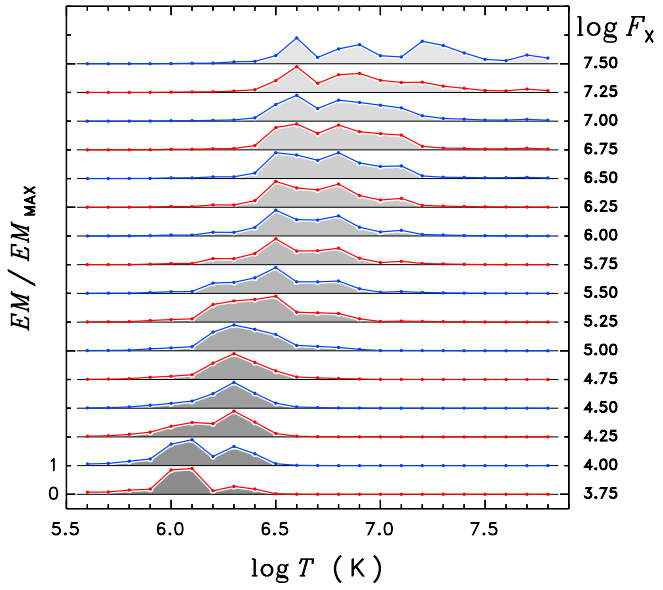

Figure 2. Normalized Wood et al. Relative Emission Measure Distributions ordered by the stellar X-ray surface flux log F_X, and offset in the y-axis for clarity. The EMDs highlighted in blue are the original models. Those highlighted in red are extrapolated/interpolated versions

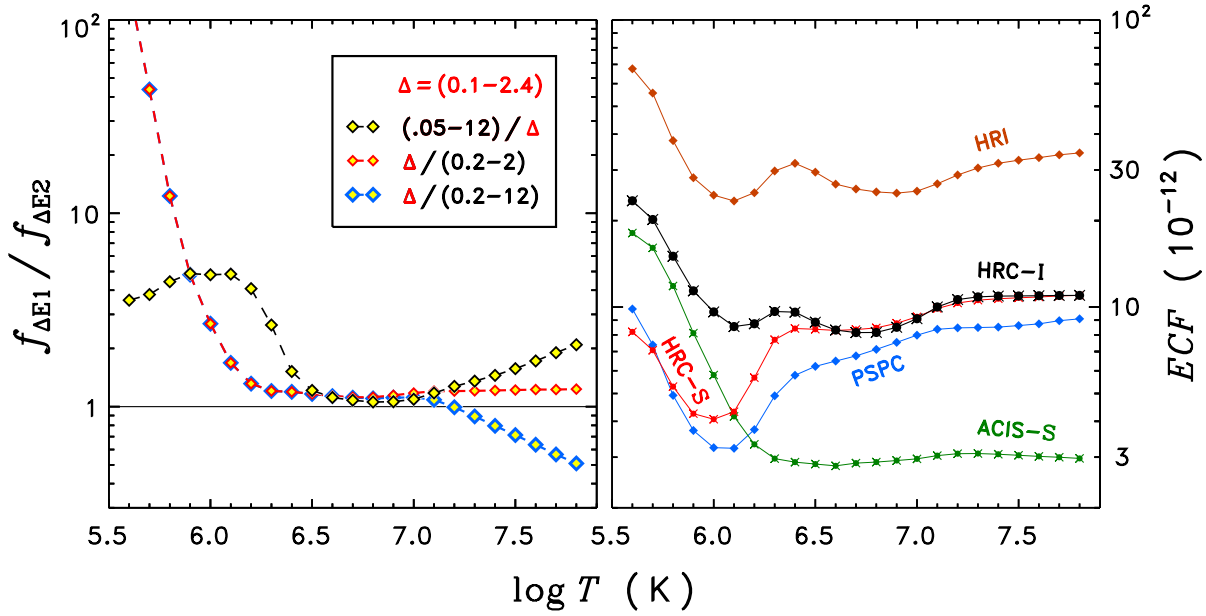

Figure 3. *Left panel:* X-ray flux ratios for various reference energy bands, according to the legend. *Right panel:* Temperature-dependent ECFs for the several indicated X-ray instruments.

the higher energy band to the lower energy 0.1–2.4 keV reference. The downward jog above log $T \sim 7$ reflects the increasing contribution from emissions above 2.4 keV.

Finally, the yellow diamonds trace the ratio of the "total" soft X-ray flux, 0.05–12 keV, versus the reference 0.1–2.4 keV flux. The 0.05–0.10 keV region (125–250 Å) covers the short EUV and contains

numerous bright emissions from various moderate-to-high ionization stages of iron (and nickel), some of which are strongly enhanced at the higher temperatures (e.g., Fe XV, Fe XVI), but most of which favor the cooler range of coronal conditions (e.g., Fe IX, Fe X). The higher-energy 2.4–12 keV band is dominated by He-like and H-like iron lines and the bremsstrahlung continuum. The upper energy limit is somewhat arbitrary, but is pragmatic in the sense that it corresponds to the high-energy cutoff of the XMM EPIC camera system alluded to above. For normal late-type stars, whether the upper limit is 6 keV, 10 keV, or 12 keV, would make no practical difference in terms of the total X-ray flux emitted by the stellar corona. The ratio curve shows a significant uptick at the cooler temperatures; then a minimum at $\log T \sim 6.8$, where the dominant contribution to the 0.05–12 keV total comes from the 0.1–2.4 keV part; followed by a rise toward hotter temperatures reflecting the increasing participation of the harder energies beyond 2.4 keV.

The wavelengths longward of 250 Å up to 1150 Å are characterized by isolated emission lines from generally lower ionization states, such as He II, C III, O V, and O VI (see, e.g., Paper II). The trend continues into the FUV, with species such as C III, Si III, Si IV, C IV, and N V, for the temperature range above about 5×10^4 K. H I 1215 Å Lyα dominates the emission of cooler plasma ($T\lesssim2\times10^4$ K) in the FUV, although the NUV Mg II doublet near 2800 Å provides the bulk of the chromospheric cooling below about 10^4 K, exceeding the flux of Lyα by a factor of 2.3 for the Sun (Paper I). (Lyα dominates the cooling of the upper chromosphere, above 10^4 K.)

The curves in the right panel of Fig. 3 are temperature-dependent EFCs for various instruments of interest to the present study. The lower the curve, the more sensitive the instrumental response at that temperature. Dark dots and crosses refer to the Chandra HRC-I camera, circa 2020, the main source of the X-ray detections described here. Red dots, also crossed, are for the companion HRC-S detector, circa 2020, which has a significantly better soft response than HRC-I at lower temperatures, by design (but a higher detector background and smaller field of view). The green curve with crossed dots is for the Chandra ACIS-S CCD, circa 2002, early in the mission before the more recent soft degradation of the camera had occurred (due to build-up of organic contamination on the optical blocking filters). Early ACIS-S had similar soft response to that of contemporary HRC-I, but much better sensitivity at $\log T > 6.0$. The two curves marked with diamonds illustrate 1990s ROSAT. The upper orange distribution is for the High-Resolution Imager (HRI), which utilized a microchannel plate intensified camera system, a predecessor to the Chandra HRC. The lower blue curve is for the PSPC, a more traditional (at the time) gas-filled imaging proportional counter. The ROSAT HRI was not very sensitive, but achieved significantly higher spatial resolution than the PSPC (5″ versus 25″), which was important in crowded stellar fields, or for close binaries like α Cen. Conversely, the PSPC had much higher sensitivity, similar to that of HRC-S, but low spatial resolution compared with the contemporary solid-state cameras. (Although the discussion has focused on the detector systems, it should be kept in mind that the sensitivity to X-rays also is shaped by the design and quality of fabrication of the telescope optics out in front.)

All the detector curves, and two of the flux ratios, display steep increases with decreasing plasma temperature. Thus, convolutions against the low-log $F_{\rm X}$ EMDs will be biased toward the elevated, low-temperature test-curve values. On the other hand, the high-log $F_{\rm X}$ EMD curves face generally flatter ECFs, so the convolved values will be less dependent on the specific EMD model. The various targets of the Total EclipSS program were observed by different instruments in different epochs. ECF curves like those displayed in Fig. 3 were constructed for various combinations of epoch and

interstellar extinction for the specific circumstances of the targets of the program, and convolved with the appropriate EMDs to provide appropriate ECF calibration curves to apply in the optimization scheme described later.

2.2.2. *Chandra X-ray Observatory*

The High-Resolution Camera (HRC-I) of Chandra X-ray Observatory has been uniquely valuable in the study of nearby bright late-type stars, especially coronal dwarfs of all activity levels. HRC-I is immune to "optical loading," the impact of low-energy photons on CCD-type X-ray detectors, which requires mitigation by extra blocking filters or shortened frame times. HRC-I also avoids "pile-up," the accumulation of multiple X-ray events in a single cell of a CCD detector during the integration cycle. HRC-I retains excellent sensitivity to the softer X-ray emission typical of low-activity coronae like the Sun's, whereas the cooled CCD detectors of Chandra have lost significant low-energy response owing to long-term accumulation of molecular contamination on their fixed optical blocking filters.

On the other hand, HRC-I lacks meaningful energy resolution compared to the CCD cameras, which typically achieve modest but useful $E/\Delta E \sim 50$. However, as noted previously, detailed EMD models have been derived for a number of nearby bright coronal stars, thanks to high-resolution X-ray spectra from Chandra's LETGS ($E/\Delta E \sim 500 - 1000$; e.g., Wood et al. 2018, and references to previous work therein).

Finally, the arcsecond spatial resolution of HRC-I has been essential to capture the coronal emissions of several key late-type close visual binary systems, including α Cen, ξ Boo, and 70 Oph of the present study. These systems are important because the fundamental stellar parameters, especially mass and age, can more precisely be established than for isolated field stars, thanks to astrometric and radial-velocity orbits and evolutionary considerations. The physically closer the binary components are, the more valuable the system, because of the likelihood that at least one, and possibly more, complete orbits have been recorded within the past 100 years of "modern" astronomical measurements. At the same time, the current proximity on the sky of the components in the aforementioned binaries makes them unsuited for observations by other contemporary X-ray observatories, such as XMM-Newton, Swift, and NuSTAR, as well as more recent eROSITA, all of which have resolutions $\gtrsim 10''$ compared to Chandra's $1''$.

The ten EclipSS subsample stars were approved in a Chandra Cycle 22 program (jointly with HST), called the "Bad Attitude Project." Because of aging insulation in the equipment bay of the Chandra satellite bus, there are pointing orientations where the hydrazine propellant tanks suffer excess solar heating, which presents a threat to the mission if they were to fail catastrophically. Consequently, these attitudes are categorized as "bad," and the planners must ensure that targets at those orientations are observed in such a way as to manage the heating. The additional burden on scheduling has forced the Chandra Project to put restrictions on targets that perpetually are at the bad attitudes, which unfortunately includes the high Ecliptic latitudes of the EclipSS stars, which otherwise are favorable for the reasons mentioned earlier. Despite the attitude challenges, the Cycle 22 targets were approved, probably helped by the relatively short, scheduling-friendly exposures proposed.

The Chandra HRC-I pointings on the EclipSS subsample were carried out mainly in late-2020. Exposure times were 5–10 ks, based on scaling the observed short-FUV fluxes according to prevailing X-ray/FUV correlations. This rubric worked well for the G and K dwarfs, but underestimated the exposures for the early-F sample members, most of which, in hindsight, showed a similar X-ray/FUV

deficiency as described earlier for Procyon. Nevertheless, all the targets were detected at significant flux levels.

X-ray monitoring observations of four of the Reference group—α Cen AB, Procyon, and the Sun—have already been described in previous Paper V. The two new binaries, ξ Boo and 70 Oph, are part of a relatively recent long-term joint Chandra/HST X-ray/FUV project called "Cycles and the Seven Dwarfs" (counting α Cen AB and Procyon in the dwarf total; although somewhat of a stretch for the latter, a borderline subgiant (class IV-V)), which also made use of HRC-I on the high-energy side, because of the excellent soft response and angular resolution. The Chandra "Cycles" program obtains two 5 ks pointings on each of the systems annually (plus a single 2-orbit HST/COS observation of each binary). To date, four Chandra (and two HST/COS) observations of ξ Boo and 70 Oph have been secured, most recently 2021 October (70 Oph). The two primaries are $\sim$1 cnt s^{-1} sources, while the secondaries are down about a factor of five. Thus a 5 ks exposure is more than adequate to detect both components, but nevertheless guards against misinterpreting transient flares as the normal X-ray level in that epoch. Some variability is present in a few of the ξ Boo and 70 Oph light curves, but more muted than a classical flare, and perhaps just the normal state of affairs for such stars. The new Chandra observations of the EclipSS subsample and the two Reference binaries are summarized in Table 2.

Table 2. Chandra HRC-I Pointings

Target	ObsID	$\mathrm{UT_{mid}}$	t_{exp}	δx	δy	b	CR	f_X	f_X/f_{BOL}	$\log L_{\mathrm{X}}$
		(yr)	(ks)	($''$)	($''$)		(cnt s^{-1})	(10^{-12})	(10^{-7})	(erg s^{-1})
1	2	3	4	5	6	7	8	9	10	11
EclipSS Subsample										
HD 24636	23397	2020.821	5.06	+0.65	+0.28	0.037	0.020±0.002	0.18±0.02	49±5	28.84
HD 38459	23401	2020.949	5.12	+0.44	−0.11	0.036	0.031±0.003	0.27±0.03	231±22	28.65
HD 39755	23402	2021.370	5.07	−0.88	−0.20	0.039	0.011±0.002	0.10±0.02	52±10	28.88
HD 41004	23403	2020.947	5.10	+1.10	+0.26	0.036	0.124±0.005	1.09±0.04	(1.00±0.04)×10^3	29.30
HD 62850	23399	2020.944	4.93	+0.21	+0.20	0.041	0.211±0.007	1.86±0.06	522±17	29.38
HD 150706	23400	2020.841	5.11	+0.32	−0.04	0.039	0.099±0.005	0.87±0.04	208±11	28.92
HD 156559	23396	2020.877	5.07	−0.17	−0.28	0.039	0.004±0.001	0.04±0.01	20±5	28.46
HD 172669	23404	2021.023	10.01	+0.03	−0.20	0.038	0.008±0.001	0.07±0.01	29±4	28.05
HD 180712	23405	2020.951	9.99	+0.12	−0.12	0.036	0.010±0.001	0.09±0.01	52±5	28.34
HD 185239	23398	2020.976	9.84	+0.39	−0.20	0.040	0.013±0.001	0.11±0.01	81±6	28.96
HD 131156 A (ξ Boo A)										
	22657	2020.296	5.10	−0.05	+0.02	0.040	1.701±0.019	14.79±0.17	378±4	28.91
	22658	2020.926	5.11	+0.71	+0.58	0.042	1.529±0.018	13.28±0.16	340±4	28.86

Table 2 *continued on next page*

Table 2 *(continued)*

Target	ObsID	UT_{mid}	t_{exp}	δx	δy	b	CR	f_X	f_X/f_{BOL}	$\log L_X$
		(yr)	(ks)	($''$)	($''$)		(cnt s^{-1})	(10^{-12})	(10^{-7})	(erg s^{-1})
1	2	3	4	5	6	7	8	9	10	11
	22659	2021.382	5.10	−0.84	−0.25	0.038	1.411±0.017	12.26±0.15	313±4	28.83
	22660	2021.259	5.05	−0.61	+1.30	0.039	1.634±0.018	14.20±0.16	363±4	28.89
									349±25	
HD 131156 B (ξ Boo B)										
	22657	2020.296	5.10	−4.76	+2.42	0.040	0.322±0.008	2.80±0.07	309±8	28.18
	22658	2020.926	5.11	−4.05	+2.86	0.042	0.242±0.007	2.11±0.06	233±7	28.06
	22659	2021.382	5.10	−5.55	+1.97	0.038	0.202±0.006	1.77±0.05	195±6	27.98
	22660	2021.259	5.05	−5.35	+3.51	0.039	0.307±0.008	2.67±0.07	294±8	28.16
									258±46	
HD 165341 A (70 Oph A)										
	22663	2020.110	5.08	−3.13	+0.94	0.040	0.662±0.012	5.78±0.10	92±2	28.26
	22664	2020.479	4.98	−3.68	+0.63	0.040	0.779±0.013	6.79±0.11	108±2	28.33
	22666	2021.599	5.05	−3.59	+0.16	0.038	0.903±0.014	7.86±0.12	125±2	28.39
	22665	2021.761	5.07	−3.31	+0.87	0.041	0.902±0.014	7.85±0.12	125±2	28.39
									113±14	
HD 165341 B (70 Oph B)										
	22663	2020.110	5.08	+2.58	−2.53	0.040	0.166±0.006	1.48±0.05	74±3	27.66
	22664	2020.479	4.98	+2.05	−2.84	0.040	0.131±0.005	1.17±0.04	59±2	27.56
	22666	2021.599	5.05	+2.21	−3.21	0.038	0.135±0.005	1.21±0.04	61±2	27.58
	22665	2021.761	5.07	+2.50	−2.48	0.041	0.172±0.006	1.53±0.05	77±3	27.68
									68±8	

NOTE—Col. 4 exposure duration includes compensation for dead-time. Cols. 5 and 6 positional offsets are with respect to target coordinates specified in the original proposal: the binaries are dominated by the relative orbits. Col. 7 is the background count rate, b, in cnt ks^{-1} $(''){}^{-2}$, measured in a large annulus centered on the source (inner radius 130$''$, outer radius 165$''$). Col. 8 count rate (CR) was collected in a $r = 1.''5$ detect cell, and corrected for the 95 % encircled energy fraction. Cited uncertainty is Poisson. Col. 9 X-ray flux at Earth (0.1–2.4 keV; erg cm^{-2} s^{-1}) was calculated from the CR using a source-specific ECF based on an optimization scheme involving the Wood EMD models.

The Chandra HRC-I event lists were processed as described in Ayres (2014), utilizing a $r = 1.''5$ detect cell (95 % encircled energy), and a background annulus with an inner radius of 130$''$ and outer radius of 165$''$ centered on the source. Figure 4 illustrates postage-stamps of the HRC-I pointings

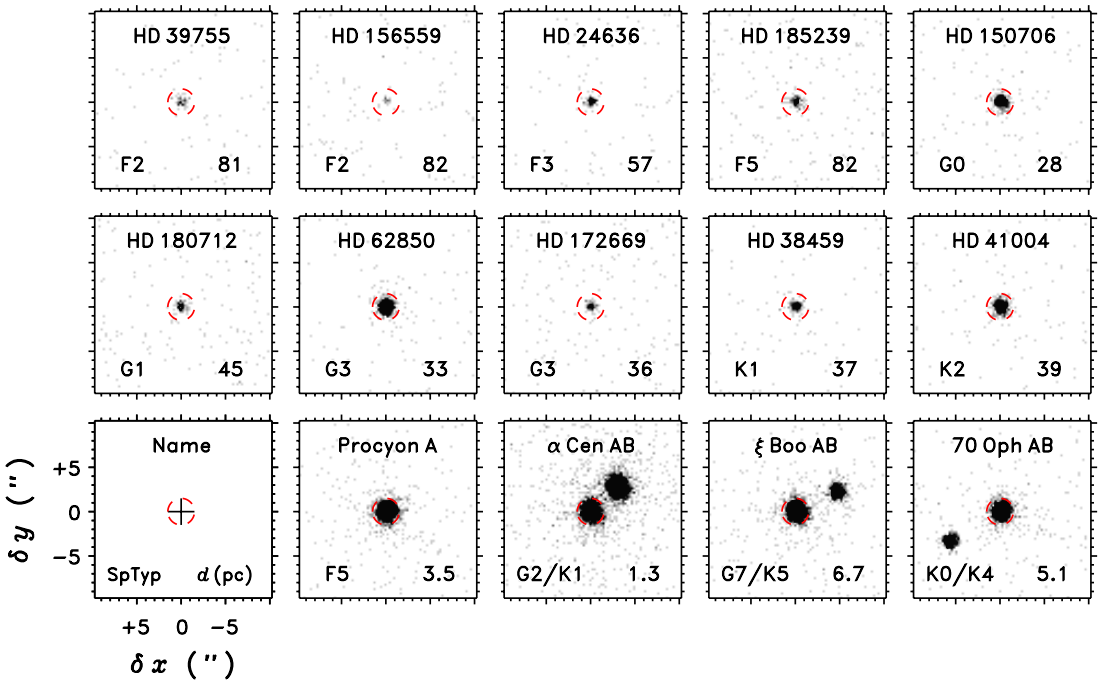

Figure 4. Rogues gallery of the Chandra HRC-I pointings on the EclipSS subsample (upper two rows), and several of the Reference stars (bottom row). The individual maps are 20″ on a side, and the X-ray events were binned into 0.″25 pixels. The reverse gray scale saturates at 5 cnt px^{-1}. Exposures were 5–10 ks. The $r = 1.''5$ detect cells (95 % encircled energy) are red dashed.

on the EclipSS subsample, as well as representative exposures of several of the Reference stars from specific epochs.

ECFs were derived for the different targets according to an optimization scheme, to be described shortly, based on convolving ECF test functions, such as illustrated in Fig. 3, with the Wood EMD models. For the EclipSS subsample, the test function was for circa-2020 HRC-I based on a mildly absorbed ($N_{\rm H} = 3{\times}10^{18}$ cm^{-2}), solar-abundance APEC plasma emission model. The EclipSS subsample targets are 30–80 pc from the Sun, in a relatively low-density ISM bubble (see Paper III, and references therein). Much of the apparent interstellar absorption occurs closer to the Sun, thus adopting the same column density $N_{\rm H}$ for all the subsample members was viewed as reasonable, and in any case the influence of interstellar extinction is relatively minor. The "Cycles" targets, ξ Boo AB and 70 Oph AB, were assigned a similar test function, although with $N_{\rm H} = 1{\times}10^{18}$ cm^{-2}, given the proximity of those systems (all within 10 pc).

In the Ayres (2014) study of α Cen AB (and peripherally also Procyon), count-rate-dependent ECFs for the 0.2–2 keV band were developed specifically for each object based on emission-measure modeling of the respective soft LETGS spectra. Fortuitously, the available three epochs of LETGS pointings on AB, taken over about 11 years, happened to capture coronal low and high states of both stars, so the hardening of each SED toward the cycle MAX could be tracked (see, also, Wood et al. 2018). In the present study, with the updated 0.1–2.4 keV energy range, new ECFs were derived for each individual pointing on α Cen AB and Procyon, using the Wood EMD modeling strategy described below. The test functions were based on the unabsorbed 0.1–2.4 keV flux predicted by

WebPIMMS for Chandra HRC-I, circa 2010, and a lightly absorbed ($N_{\rm H} = 4{\times}10^{17}$ cm^{-2} for AB and $1.2{\times}10^{17}$ for Procyon; from Wood et al. 2018), solar-abundance APEC model.

Also as noted in Paper V, the HRC-I camera has declined in sensitivity by about 20 % since 2010, thus a nominal 2 % per year degradation was adopted to correct the ECF2010 fluxes to the subsequent epochs (zero degradation was assumed for 2000–2010). Because of the switch to the new reference energy band, revised X-ray measurements of α Cen AB and Procyon are provided in Appendix A, Tables A1 and A2, respectively. Table A1 also lists two new HRC-I pointings on AB, which, for scheduling reasons, were conducted close together rather than with the normal semiannual spacing. Unfortunately, there was no contemporaneous HST/STIS pointing available to match to the new Chandra observations, so the recent X-ray measurements of AB will not appear in the X-ray/FUV flux–flux diagrams presented later.

Finally, solar X-ray fluxes over the period 2009.0–2020.0, corresponding to recent, albeit modest, Cycle 24, were recalculated from the FISM2 daily records (see Paper V) for the extended 0.1–2.4 keV reference energy range. No ECF was involved because FISM2 already provides spectrally resolved absolute flux densities (adjusted to a distance of 1 AU), so the revision merely required modifying the flux integration wavelength limits. For the purposes of display later on, the daily solar values were averaged in 81-day bins (equivalent to three solar rotations) to suppress rotational modulations in favor of long-term evolution due to the magnetic cycle. The (logarithmic) average solar X-ray luminosity over this period was $\log L_{\rm X} = 27.00$ erg s^{-1} in the new energy bandpass. Given the rather tepid nature of Cycle 24, that estimate undoubtedly is on the low side compared to more vigorous solar cycles, by perhaps several tenths of a dex. Further, the range in $L_{\rm X}$ from solar MIN to MAX in the new reference energy band (for Cycle 24) is only a factor of four, whereas in the previous, harder energy bandpass the cycle contrast was more like a factor of ten. Again, the cycle contrasts in both energy bands likely would be significantly larger in a stronger solar cycle.

2.2.3. *X-ray Measurements of the Other Stars*

The remaining targets of Total EclipSS, all nearby bright stars, have various provenances for the X-ray fluxes used here, typically the 1990s ROSAT RASS and in some cases dedicated PSPC (and/or HRI) pointings; plus one of the Chandra cameras or XMM-Newton EPIC (which itself has separate detector modules, pn and MOS). Epsilon Eri was a special case (part of the reason for inclusion in the Reference group). The K dwarf was the subject of a recent multi-year monitoring program with XMM-Newton 2013–2019 (Coffaro et al. 2020), but also was recorded by XMM-Newton a decade earlier, in 2003. Here, the ϵ Eri X-ray fluxes were taken from the 4XMM-DR11 catalog (via the HEASARC Browse interface[10]) ep8 values (0.2–12 keV). 4XMM-DR11 includes a recent 2019 pointing not in the Coffaro et al. study. A conversion factor ($\sim$ 1.30) was calculated, using the previously mentioned EMD scheme, to translate the 0.2–12 keV fluxes to the reference 0.1–2.4 keV bandpass. Among the nine epochs in common with Steltzer et al., and noting that the 0.2–12 keV ep8 band essentially is identical to the 0.2–2 keV reference utilized by Coffaro et al. for a moderate-activity $\log F_{\rm X} \sim 5.8$ source like ϵ Eri (0.2–12 keV fluxes would be $\sim$2 % *higher* than 0.2–2 keV for the appropriate $\log F_{\rm X} = 5.75$ EMD model), the 4XMM-DR11 fluxes are systematically 15 % *lower*, which likely reflects differences in the processing methodology, but is an insignificant offset for the purposes here, where the normalized X-rays of the target stars range over orders of magnitude.

[10] See: https://heasarc.gsfc.nasa.gov/cgi-bin/W3Browse/w3browse.pl

Most of the five Related stars have X-ray measurements exclusively from ROSAT and XMM-Newton (4XMM-DR11). The exceptions are κ Cet and τ Cet. The former has two ACIS-S exposures, ∼14 ks each, in late-2019 about a month apart. Tau Cet has two deep (∼ 50 ks) Chandra pointings as well, with the ACIS-S and HRC-S cameras, separated by about 18 years. There also is a 4XMM-DR11 ep8 flux for τ Cet, but it is significantly (factor of two) lower than the values inferred from ROSAT and the two Chandra pointings (see below), even with a substantial correction from the 0.2–12 keV band to 0.1–2.4 keV. Tau Cet is a visually bright star so requires an extra blocking filter with the EPIC camera to avoid optical loading effects. There were indications from previous contemporaneous XMM-Newton and Chandra observations of visually bright α Cen A that the EPIC thick filter degrades the soft response of the camera. That likely was the cause of the dramatic factor of ∼20 X-ray fading of the solar twin's count rate in 2005 February reported by Robrade et al. (2005), based on EPIC observations at a time when α Cen A had fallen into a low, soft state of its ∼ 19 yr activity cycle (Ayres et al. 2008). Chandra HRC-I pointings a few months later, in 2005 October, and subsequently[11], revealed much higher X-ray fluxes for α Cen A (similar to numerous observations of the star in the 1990s by ROSAT). The HRC-I camera is a different design than EPIC, and is insensitive to optical loading. Because τ Cet is an inactive star, similar to α Cen A MIN in L_X/L_{BOL}, it too likely was adversely affected by the EPIC blocking filter, so the 4XMM-DR11 measurement was discounted. All of the other 4XMM-DR11 candidates are higher-temperature sources for which any degradation of the EPIC soft response is less important.

The ROSAT PSPC and HRI detectors and the Chandra ACIS and HRC cameras all have steep dependences of their ECFs on temperature for cool coronae ($\log T \sim 5.8$–6.0 K: see Fig. 3), unfortunately all in the same sense of increasing ECF with decreasing $\log T$. An X-ray flux estimate for τ Cet was assembled according to the $\log F_X$ optimization strategy described below, based on the ROSAT PSPC RASS flux, an average of two independent HRI pointings, ACIS-S, and HRC-S. The derived (logarithmic) X-ray surface fluxes for τ Cet were $\log F_X \sim 3.4$–4.0 erg cm^{-2} s^{-1} here, versus 3.9 from Judge et al. (2004) (based solely on ROSAT). Fluxes were averaged across the four instruments based on the optimum EMD analysis for each, yielding a standard deviation that reflects a combination of possible temporal variability as well as inter-calibration systematics. The adopted flux was $f_X \sim 2.0 \pm 0.8 \times 10^{-13}$ erg cm^{-2} s^{-1}. This corresponds to $\log L_X \sim 26.50$ erg s^{-1} for the 3.65 pc distance, essentially the same as reported by Judge et al. (2004), in the same 0.1–2.4 keV bandpass, and a factor of three below the solar Cycle 24 (logarithmic) average value ($\log L_X \sim 27.00$).

Figure 5 schematically illustrates how energy conversion factors were determined for the various X-ray observations (except XMM-Newton, because the 4XMM-DR11 catalog values already are flux-calibrated). Each curve is, on the y-axis, a calculation of the stellar X-ray surface flux given the observed count rate and a small grid of ECFs derived by convolving temperature-dependent sensitivity relations (e.g., Fig. 3) through Wood EMD models (Fig. 2), which in turn were based on grating spectra with specific associated X-ray surface fluxes (as noted on the x-axis). Where the calculated surface flux curve intersects the 1:1 line indicates the self-consistent $\log F_X$ (marked by a red plus sign); corresponding to an optimum choice of the EMD model. The corresponding optimum ECF was interpolated in the grid. The width of each curve indicates the uncertainty devolving from the input count rate. Several key targets are marked next to their curves. Procyon, ξ Boo AB, and 70 Oph AB

[11] Alpha Cen A's 2005 soft low-state persisted for another five years.

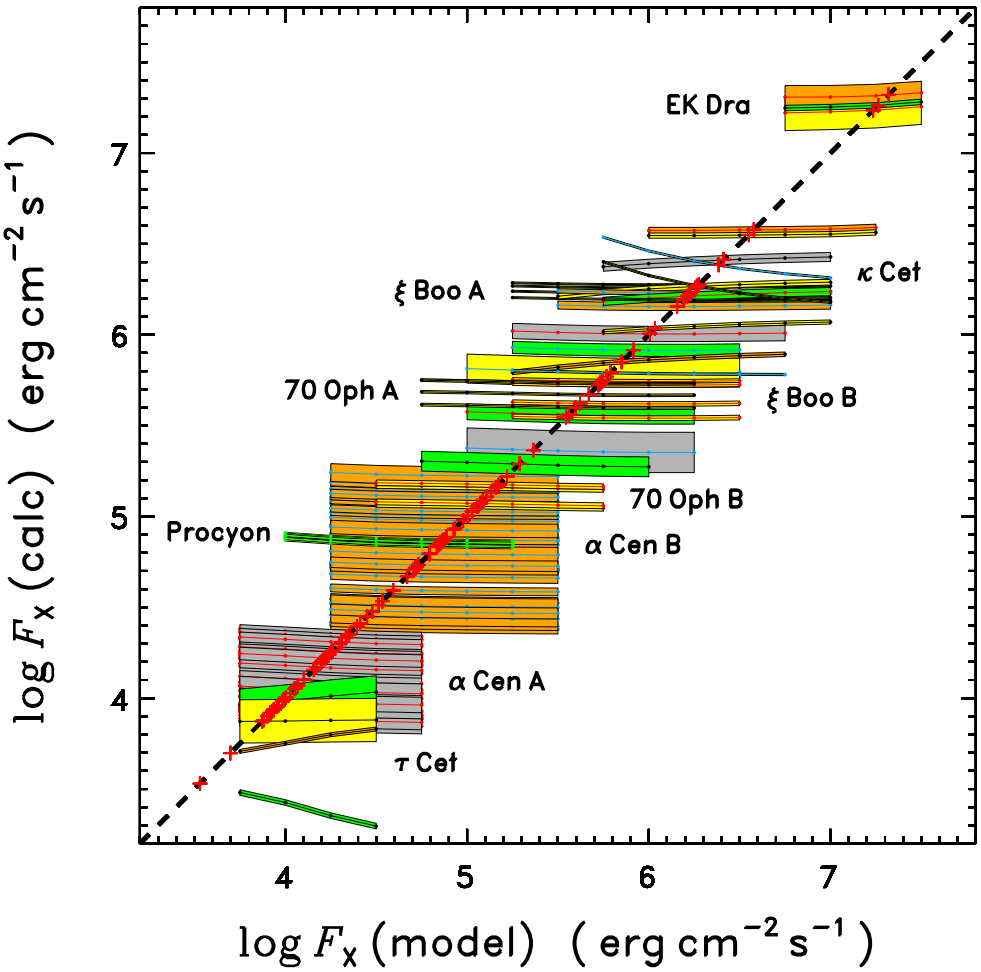

Figure 5. Determination of optimum energy conversion factors for the Total EclipSS X-ray observations (except 4XMM-DR11, which already is flux-calibrated). Each curve represents a calculation of the stellar X-ray surface flux (on y-axis) given the observed count rate (vertical width is uncertainty in the CR) and ECFs convolved through Wood EMD models; the latter are associated with specific X-ray surface fluxes (arrayed on x-axis). The intersection with the dark dashed 1:1 line indicates the optimum, self-consistent $\log F_{\rm X}$, which then implies an optimum ECF as interpolated in the model grid. Most of the illustrated slightly sloping curves are for Chandra HRC-I; the more steeply sloping relations are for ACIS-S and HRC-S; but several ROSAT PSPC and HRI examples are interspersed.

are offset for clarity. The numerous, slightly sloping curves (e.g., for α Cen A) are for the Chandra HRC-I camera. The more steeply downward sloping thin green curve for τ Cet (and two similar ones for κ Cet) are for Chandra ACIS-S. The more steeply upward sloping orange curve for τ Cet is for HRC-S. The broader yellow and green bands for τ Cet are ROSAT PSPC and HRI, respectively; and the several stripes for EK Dra also are from ROSAT. The generally broader shaded bands below EK Dra and above the block representing α Cen B are for the EclipSS subsample targets, observed with HRC-I. The relatively flat curves for Chandra HRC-I indicate that the energy response is nearly independent of coronal temperature for late-type stars of a wide range of activity levels, a desirable attribute in studies such as this.

Table 3. Other X-ray Fluxes

Target	f_X	$f_X/f_{\rm BOL}$	$\log L_{\rm X}$	Notes
	(10^{-12})	(10^{-7})	(erg s^{-1})	
1	2	3	4	5
			Related objects (G-type dwarfs)	
τ Cet	0.20±0.08	1.6±0.7	26.50	2RXS,BMWHRICAT(2),ACIS-S,HRC-S
κ Cet	8.6±1.8	265±55	28.95	2RXS,ROSPSPC,BMWHRICAT,ACIS-S(2),4XMM-DR11(3)
χ^1 Ori	12.2±0.8	259±17	29.04	2RXS,BMWHRICAT,4XMM-DR11
π^1 UMa	5.6±0.4	379±27	29.15	2RXS,ROSPSPC,4XMM-DR11
EK Dra	8.4±1.3	3620±560	30.07	2RXS,ROSPSPC(3),BMWHRICAT(4),4XMM-DR11
			Reference sample	
Sun	···	$2.61^{+1.57}_{-0.98}$	27.00	FISM2(45)[a] (1.4–5.8)
α Cen A	$5.38^{+2.25}_{-1.59}$	$1.98^{+0.83}_{-0.59}$	27.06	HRC-I(32) (1.2–3.5)
α Cen B	$13.9^{+9.8}_{-5.7}$	$15.5^{+10.8}_{-6.4}$	27.47	HRC-I(32) (5.9–39)
Procyon	12.1±0.3	6.8±0.2	28.25	HRC-I(10) (6.5–7.1)
ϵ Eri	17.6±4.1	164±38	28.34	4XMM-DR11(10)

NOTE—Col. 2 X-ray flux at Earth (0.1–2.4 keV; erg cm^{-2} s^{-1}) was calculated using source-dependent optimized ECFs for the indicated instruments (see text), and averaged over the available epochs (logarithmic averages were applied to the Sun and α Cen AB owing to the larger variations). In the Notes, FISM2 is a solar X-ray database (see Paper V); HRC-I, HRC-S, and ACIS-S are Chandra imagers; 2RXS is the Second ROSAT All-Sky Survey Bright Source Catalog (PSPC detector), ROSPSPC is a catalog of PSPC pointings, BMWHRICAT is a specialized database for the ROSAT HRI camera; and 4XMM-DR11 is a source catalog from XMM-Newton EPIC (the "ep8" flux therein is for the bandpass 0.2–12 keV, but converted to 0.1–2.4 keV, by means of source-dependent energy-band scale factors). Documentation for these catalogs can be found through https://heasarc.gsfc.nasa.gov/cgi-bin/W3Browse/w3browse.pl .) A parenthetical value appended to the catalog name is the number of independent epochs considered for that object (if more than one). The parenthetical ranges in the Notes for the initial four Reference stars are the apparent cycle MIN and MAX $f_{\rm X}/f_{\rm BOL}$ (10^{-7}) values over the available epochs (Cycle 24 for the Sun).
[a]81-d (3-rotation) averages encompassing solar Cycle 24.

Table 3 lists derived X-ray fluxes for those sample members not already included in the (new) observations of Table 2. These values were aggregated via HEASARC Browse, using source-dependent optimized ETCs for the appropriate epochs, as described above. Similarly, the 4XMM-DR11 fluxes were converted from the native 0.2–12 keV band to the reference 0.1–2.4 keV, by means of convolved energy-band scale factors (based on test functions in the left panel of Fig. 3) derived from the Wood EMD model closest to the $\log F_{\rm X}$ of the star, as deduced from other X-ray observations. Cited uncertainties are standard deviations over the various independent measurements, so when different

instruments were combined, there will be an inter-calibration aspect to the uncertainty as well as a temporal part. The Table also includes average values and ranges for the more heavily monitored Reference stars α Cen, Procyon, and the Sun.

2.3. *HST UV Spectrographs: COS and STIS*

The Chandra "Bad Attitude Project" was a joint program with HST/COS. The objective on the COS side was to fill in the FUV spectrum beyond 1420 Å, which contains the key C IV 1550 Å doublet and He II 1640 Å. The original EclipSS effort in 2018–19 was only able to collect the short-FUV spectrum of each star in the time available in the single orbit allocated to each target, using grating G130M with two CENWAVEs, 1222 Å and 1291 Å, each at FP-POS steps 3 and 4 (small grating rotations intended to help mitigate detector fixed pattern noise). The original EclipSS stars were faint enough at the normally very bright chromospheric Lyα emission feature to allow both sides of COS's cross-delayed line (XDL) detector to be activated for G130M-1291, to access the important region 1150–1290 Å on the B-side of the camera. (Many of the nearby stars of the Related and Reference groups are too bright at Lyα to activate side-B for CENWAVE 1291, but setting 1222 has Lyα in the detector gap, so is safe.) The new program focused on the subsample of the ten FUV-brightest EclipSS targets, collecting long-FUV (1420–1710 Å) spectra of each, again in a single orbit per star, using grating G160M with its 1533 Å setting and all four FP-POS steps. COS G130M-1291 overlaps with G160M-1533 in the interval 1340–1420 Å, which contains a number of important spectral features including the neutrals Cl I 1351 Å and O I 1355 Å; the moderately ionized Si IV 1400 Å doublet and O IV intersystem multiplet; and the highly ionized Fe XII 1349 Å and Fe XXI 1354 Å coronal forbidden lines. These overlap features benefit in S/N from co-adding the G130M and G160M settings observed in the different epochs, but also shed some light on the variability properties of each star, at least for those specific lines.

The new COS pointings were carried out over a two-week period in 2020 September, roughly contemporaneously with the Chandra HRC-I part described earlier. Each target was captured by means of an NUV imaging acquisition, with the Bright Object Aperture (BOA) and either MIRRORA or (attenuated) MIRRORB, depending on the NUV brightness of the star. NUV integration times ranged from 5–55 s. Following the acquisition, the G160M-1533 exposure was taken through the 2.″5-diameter Primary Science Aperture (PSA), in time-tag (T-TAG) mode, utilizing all four FP-POS steps, to fill out the orbit. The G160M exposure times ranged from 2.1–2.4 ks, depending on the target visibility. The COS pointings on the EclipSS subsample are summarized in the first part of Table 4. As noted in the Table, several of the initial September observations failed (mainly due to a balky HST gyro, which affected Guide Star acquisitions). The failed observations were repeated within about two months, still during the fall of 2020. One of the repeat observations (legoZ3010: HD 39755) also failed, but the original "unsuccessful" observation (lego07010) did manage to record two of the FP-POS steps, which was judged adequate for the subsequent analysis.

Table 4. HST COS and STIS Pointings

Target	ObsID	UT_{start}	CENWAVE	t_{exp}	RV_{corr}	Notes
		(yyyy-mm-dd.DD)	(Å)	(s)	(km s^{-1})	
1	2	3	4	5	6	7
EclipSS Subsample						
HD 24636	lego02010	2020-09-30.18	1533	2413	(+14.2, +15.2)	1–4
HD 38459	lego06010	2020-09-15.58	1533	2140	(+29.3, +36.1)	1–4
HD 39755	lego07010	2020-09-25.85	1533	1138	(+0.0, −5.9)	partial: 3,4
HD 39755	legoZ3010	2020-11-20.93	1533	2276	···	failed[a]
HD 41004	lego08010	2020-09-25.78	1533	2132	(+41.5, +47.8)	1–4
HD 62850	lego04010	2020-09-11.03	1533	2200	(+12.2, +16.8)	1–4
HD 150706	lego05010	2020-09-11.18	1533	2348	(−21.1, −17.5)	1–4
HD 156559	lego01010	2020-09-15.35	1533	0	···	failed
HD 156559	legoZ1010	2020-11-02.28	1533	2248	(−22.1, −16.4)	1–4
HD 172669	lego09010	2020-09-11.25	1533	2396	(−9.1, +5.0)	1–4
HD 180712	lego10010	2020-09-13.23	1533	0	···	failed
HD 180712	legoZ2010	2020-10-29.31	1533	1725	(−6.8, −12.1)	partial: 2,3,4
HD 185239	lego03010	2020-09-13.36	1533	2296	(+13.1, +24.1)	1–4
Related objects						
τ Cet (HD 10700)						
···	o5cy01010	2000-08-01.12	1425	1862	−16.8	PHOT
···	o5cy01020	2000-08-01.18	1425	11588	−16.2	PHOT
κ Cet (HD 20630)						
···	o5bn03050	2000-09-19.37	1425	2007	+18.3	PHOT
···	o5bn03060	2000-09-19.43	1425	5798	+18.3	PHOT
···	le4p02010	2021-02-06.29	1291	5046	+16.2	1–4
χ^1 Ori (HD 39587)						

Table 4 *continued on next page*

Table 4 *(continued)*

Target	ObsID	UT_{start}	CENWAVE	t_{exp}	RV_{corr}	Notes
		(yyyy-mm-dd.DD)	(Å)	(s)	(km s^{-1})	
1	2	3	4	5	6	7
···	o5bn02010	2000-10-03.05	1425	1870	−15.2	PHOT
···	o5bn02020	2000-10-03.10	1425	2900	−15.2	PHOT
···	o5bn02030	2000-10-03.17	1425	2000	−14.6	PHOT
···	lb3e06010	2010-03-19.28	1291	1300	−15.3	3,4
		π^1 UMa (HD 72905)				
···	lb3e26010	2010-02-28.94	1291	1300	+6.7	3,4
···	obq202010	2012-09-25.10	1425	2279	−11.6	PHOT
···	obq202020	2012-09-25.13	1425	3347	−10.2	PHOT
		EK Dra (HD 129333)				
···	lb3e34010	2010-04-22.39	1291	1160	···	not used
···	oboq01010	2012-03-27.70	1425	8880	−23.4	PHOT
···	lboq02010	2012-03-27.83	1577	1000	−8.9	1–4
···	lboq02020	2012-03-27.86	1291	1780	−22.0	1–4
···	lboq03010	2012-03-28.24	1577	1000	−14.2	1–4
···	lboq03020	2012-03-28.28	1291	1780	−20.7	1–4
···	lboq04010	2012-03-28.86	1577	1000	−10.2	1–4
···	lboq04020	2012-03-28.89	1291	1780	−21.4	1–4
···	lboq05010	2012-03-29.43	1577	1000	−7.1	1–4
···	lboq05020	2012-03-29.46	1291	1780	−19.0	1–4
		Reference stars				
		ξ Boo A (HD 131156 A)				
···	le5s10010	2020-02-27.03	1222	800	+0.9	1–4
···	le5s10020	2020-02-27.04	1533	820	+2.2	1–4
···	lea910010	2020-12-26.89	1222	800	−0.4	1–4
···	lea910020	2020-12-26.90	1533	772	+1.3	1–4

Table 4 *continued on next page*

Table 4 *(continued)*

Target	ObsID	UT_{start}	CENWAVE	t_{exp}	RV_{corr}	Notes
		(yyyy-mm-dd.DD)	(Å)	(s)	(km s^{-1})	
1	2	3	4	5	6	7
			ξ Boo B (HD 131156 B)			
···	le5s10030	2020-02-27.09	1222	940	−7.3	1–4
···	le5s10040	2020-02-27.11	1533	1000	−11.5	1–4
···	lea910030	2020-12-26.95	1222	940	+9.1	1–4
···	lea910040	2020-12-26.97	1533	908	+9.3	1–4
			70 Oph A (HD 165341 A)			
···	le5s11010	2020-07-09.57	1222	800	−6.1	1–4
···	le5s11020	2020-07-09.58	1533	812	−0.3	1–4
···	lea911010	2020-09-13.44	1222	800	−6.3	1–4
···	lea911020	2020-09-13.45	1533	764	−1.2	1–4
			70 Oph B (HD 165341 B)			
···	le5s11030	2020-07-09.63	1222	940	−8.6	1–4
···	le5s11040	2020-07-09.65	1533	984	+1.2	1–4
···	lea911030	2020-09-13.50	1222	940	−3.9	1–4
···	lea911040	2020-09-13.52	1533	896	+0.6	1–4
			ϵ Eri (HD 22049)			
···	o55p01030	2000-03-17.96	1425	2899	+17.1	PHOT
···	o55p01040	2000-03-18.03	1425	2899	+18.1	PHOT
···	ock101040	2015-02-01.08	1425	1435	+15.0	SPEC
···	lck102010	2015-02-01.35	1577	1000	+18.0	1
···	lck102020	2015-02-01.36	1611	1045	+13.4	3
···	lck103010	2015-02-02.35	1291	498	+14.5	3,4

Table 4 *continued on next page*

Table 4 *(continued)*

Target	ObsID	UT_{start} (yyyy-mm-dd.DD)	CENWAVE (Å)	t_{exp} (s)	RV_{corr} (km s^{-1})	Notes
1	2	3	4	5	6	7
···	lck103020	2015-02-02.47	1318	8137	+17.5	1,2,4
···	ldej01030	2017-03-07.33	1291	2722	+16.8	3
···	ldej01040	2017-03-07.40	1309	2722	+13.8	3
···	ldej01050	2017-03-07.47	1327	2722	+17.6	3
···	ldej02030	2017-03-12.23	1577	2722	+21.5	3
···	ldej02040	2017-03-12.30	1600	2722	+13.8	3
···	ldej02050	2017-03-12.37	1623	2722	+18.9	3
···	ldnq01020	2017-08-11.56	1291	2748	+16.3	3
···	ldnq01030	2017-08-11.62	1309	2748	+15.4	3
···	ldnq01040	2017-08-11.69	1327	2748	+17.4	3
···	ldnq02020	2017-08-12.55	1222	2746	+15.4	3
···	ldnq02030	2017-08-12.62	1223	2748	+17.5	3
···	ldnq03020	2017-08-14.67	1577	2696	+19.7	3
···	ldnq03030	2017-08-14.74	1600	2696	+13.7	3
···	ldnq03040	2017-08-14.80	1623	2696	+14.8	3
···	leif01020	2021-02-25.29	1291	2466	+18.3	3
···	leif01030	2021-02-25.36	1327	2466	+25.5	3
···	leif02020	2021-02-27.41	1309	2466	+25.4	3

NOTE—COS datasets (ObsID: "l…") with CENWAVE<1400 are G130M; CENWAVE>1400 are G160M; all exposures through Primary Science Aperture (PSA: 2.″5 diameter). Datasets containing "Z" are repeats of partial or failed observations. FP-POS splits for COS are numerical values or ranges cited in the Notes. STIS datasets (ObsID: "o…") are from echelle setting E140M-1425 (CENWAVE 1425); the observation aperture is cited in the Notes: PHOT=0.″2×0.″2; SPEC=0.″2×0.″06. Col. 6 radial velocities are empirical values for the specific spectra derived from low-excitation neutral lines, usually Cl I 1351 Å. Leading value of the parenthetical pairs for the EclipSS subsample refers to the CENWAVE 1291 spectrum from Paper III, while the second value is for the new CENWAVE 1533 spectrum.
[a]Repeat of lego07010. Spectrum very weak and unusable: target only partially in aperture owing to failed NUV acquisition (shutter closed during NUV-ACQ because of delay in Guide Star acquisition).

The Related objects typically have a mixture of COS and STIS pointings, in two or more epochs for all the stars except τ Cet (for which only a single STIS sequence is available). Several of the targets have relatively short COS exposures that date back to an early COS SNAPSHOT program (brief, sub-orbit filler exposures to improve the HST scheduling efficiency) to measure the coronal iron forbidden lines mentioned previously (GO-11687: "SNAPing Coronal Iron"). These observations had been carried out with G130M-1291, at FP-POS= 3 and 4, and with the side-B XDL segment

off, to avoid the over-bright H I Lyα emission of the mostly nearby stars, so only the restricted wavelength range 1290–1430 Å on side A was recorded. This interval nevertheless contains many of the key diagnostics of the chromosphere and higher temperature layers, including the corona via the Fe XII and Fe XXI forbidden lines.

At the other extreme is EK Dra, one of the original SNAPing targets, which was subsequently re-visited in a 2012 program (Ayres 2015) to assess some of the spectral peculiarities revealed in the brief 2010 SNAPSHOT observation (see Ayres & France 2010). The follow-on program had a deep STIS exposure at the outset, to provide an accurate wavelength scale to measure line Doppler shifts (the COS wavelengths are not as reliable), and then a series of four COS pointings, the first of which was as close as possible to the STIS observation, for inter-calibration purposes, and the others spaced over the subsequent two days to catch different phases of the 2.7-d rotation period. The COS sequence involved G130M-1291, again only on side-A to avoid Lyα, but at all four FP-POS; plus G160M-1577 with both sides of the detector activated and at all four FP-POS splits. The CENWAVE 1291 side-A spectra miss the important features C III 1175 Å, Si III 1206 Å, and the N V doublet at 1240 Å, but these were captured by the initial STIS exposure (which, despite a much longer duration, was significantly lower in S/N than each COS visit, but nevertheless adequate for the purpose: see Ayres 2015). The first of the COS exposures was, as mentioned in an earlier section, affected by a super-flare decay, but the prior STIS and later three COS visits appear to be normal (if you can call a star that has an X-ray luminosity a thousand times that of the Sun "normal").

The final FUV group are the Reference objects. The STIS moderate- and high-resolution FUV echelle observations of α Cen AB and Procyon were described at length in Paper V, and constitute the longest quasi-continuous such records on cool stars to date (aside from the Sun, itself, which also is represented here by long-term, in fact daily, FUV datasets: see Paper I).

Four of the remaining Reference objects are the late-type binaries ξ Boo and 70 Oph, from the joint Chandra/HST "Cycles and the Seven Dwarfs" program mentioned earlier. These systems have been observed by COS once per year each for the past two years. The scenario was similar to those described earlier, although now the visits were two orbits, to accommodate the binary components. Initially, the brighter primary was captured by an NUV imaging acquisition. This was followed by a pair of COS grating settings on the primary, G130M-1222 and G160M-1533 through the PSA, in T-TAG mode at the four FP-POS splits, to fill out the first orbit. In the second orbit, the fainter secondary star was acquired by a blind offset from the primary based on the known ephemeris, and the same G130M/G160M sequence was performed. The (relatively new) CENWAVE 1222 avoids the bright stellar Lyα emissions of these very nearby stars, at the (minor) cost of the semi-permitted O V 1218 Å feature in the red wing of the hydrogen line. CENWAVEs 1222 and 1533 overlap over only a small ∼20 Å interval (1342–1363 Å), which nevertheless contains Cl I 1351 Å and O I 1355 Å, as well as Fe XII 1349 Å and Fe XXI 1354 Å. All the Cycles FUV observations to date have been successful, and are summarized in the third section of Table 4.

The last of the Reference objects, ϵ Eri, is somewhat of a special case. There was an early deep STIS E140M observation in 2000 March, through the $0.''2\times0.''2$ photometric aperture, preferred for accurate line fluxes. The star was re-visited in 2015 February, initially with a STIS E140M exposure through the spectroscopic slit ($0.''2\times0.''06$), which provides better spectral resolution but can suffer from reduced throughput. That was followed by a series of four COS CENWAVEs, at various FP-POS steps, which covered most of the FUV, except for the $\lambda < 1290$ Å region because—as for the

other bright COS targets—detector side-B had to be deactivated for the two G130M short-FUV CENWAVEs owing to Lyα safety concerns. Although the deep multi-setting COS exposure was missing the wavelengths below 1290 Å, these could be recovered from the contemporaneous STIS observation, which spanned the entire FUV bandpass, and could be scaled to the COS fluxes to counter possible throughput issues. Two years later, ϵ Eri was fortuitously promoted to wavelength calibration target status by the COS project. Thereafter ensued three additional COS visits to the star, in 2017 March, 2017 August, and 2021 February (G130M, only) utilizing multiple CENWAVEs, but only at the single FP-POS= 3. However, the up to eight closely-spaced settings in each visit served in an equivalent fashion to multiple FP-POS for a single CENWAVE, to suppress fixed pattern noise. The 2015–2021 STIS/COS visits roughly paralleled the nine recent XMM-Newton pointings on ϵ Eri described in the X-ray section, capturing the star sufficiently well over its (short) magnetic cycle (see Cofarro et al. 2020) to qualify for the Reference group.

2.3.1. *COS Spectral Processing*

This section describes the post-processing specifically of the COS datasets. (The STIS reduction procedures were already described adequately in previous papers of this Series, and applied in the same way to the archival E140M echellegrams of the Related and Reference objects listed in Table 4.) A specialized procedure had been developed to co-add the dual G130M exposures of the original EclipSS program (see Paper III). The previous G130M spectra of the ten members of the EclipSS subsample then were joined to the newly acquired G160M exposures, co-adding the wavelengths in common. In the merging process, the wavelength scales of the separate segments were registered to the (usually) narrow Cl I 1351 Å chromospheric emission, if not washed out by high rotation. The one case affected by fast rotation was HD 156559. Its G130M and G160M spectra were separately registered to stronger features, i.e., O I 1306 Å and Si IV 1393 Å, respectively, within the two bandpasses. The brighter, higher contrast features could be measured successfully, despite the excessive rotational broadening. However, the precision of the joined wavelength scales is not so important in this case, because the severe rotational broadening imposes larger measurement uncertainties, say for the line Doppler shifts, compared with the more normal, sharp-line case.

Figure 6 illustrates an example of the process, for the merged, co-added COS G130M + G160M spectrum of the early-F dwarf HD 24636. The y-axis is the bolometrically normalized flux density, which has been utilized throughout the Trenches series to allow fairer comparisons among stars of different sizes and distances from Earth. The initial spectrum of the star for $\lambda < 1430$ Å, from Paper III, was built from separate G130M CENWAVEs, 1222 and 1291, each at two FP-POS splits. The local fluxes at the airglow lines (yellow shading: N I 1200 Å, H I 1215 Å, and O I 1305 Å[12]) were based on those splits displaying minimal contamination. At the other wavelengths, the spectrum was a weighted sum of the two G130M split-combined tracings. The new Bad Attitude Project added a typically 4-split G160M-1533 spectrum, which extends from 1340 Å to beyond 1700 Å. CENWAVE 1533 overlaps the original G130M merged spectrum between 1340–1430 Å, and provides two-epoch coverage of the important TZ doublet Si IV 1393 Å + 1402 Å to crudely assess variability of these representative "hot" lines. The G130M/G160M overlap interval also contains the coronal forbidden transitions Fe XII 1349 Å (1.6 MK) and Fe XXI (13 MK), which can trace changes in

[12] "O I 1305 Å" will be used generically to designate the atomic oxygen resonance triplet, with individual components 1302 Å, 1304 Å, and 1306 Å.

the coronal conditions between the two separated epochs. The individual CENWAVEs are depicted in blue (1222), red (1291), and green (1533). The merged, co-added spectrum is the dark tracing, slightly smoothed to reveal the underlying spectral contributions more clearly. The barely visible thin dotted-dashed curve is the photometric error, heavily smoothed and displayed as $10\,\sigma_\lambda$.

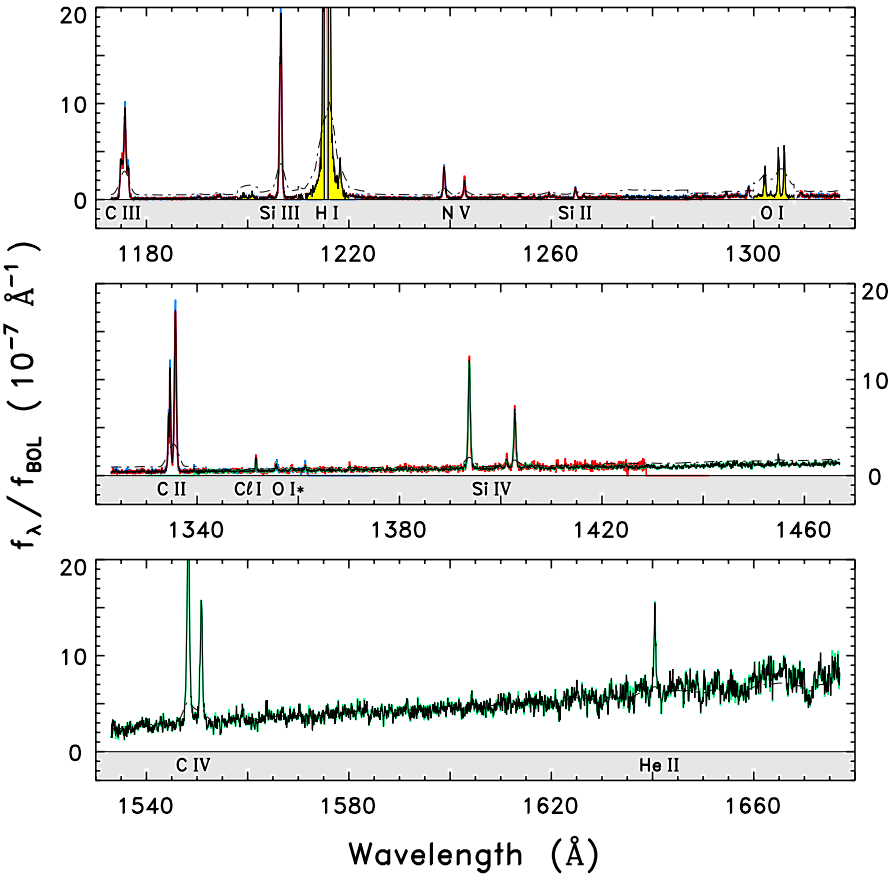

Figure 6. Merged, co-added COS G130M + G160M spectrum of HD 24636. The y-axis is the bolometrically normalized flux density. The tracing for $\lambda < 1430$ Å is from Paper III. Local fluxes at the airglow lines (yellow shading) were based on G130M splits displaying minimal contamination. The current program added a G160M-1533 spectrum, overlapping the original G130M between 1340–1430 Å. The individual CENWAVEs are depicted in blue (1222), red (1291), and green (1533). The merged, co-added spectrum is the dark curve, slightly smoothed to reveal the underlying spectral contributions more clearly. The barely visible thin dotted-dashed line is the $10\,\sigma_\lambda$ photometric error, heavily smoothed for display purposes.

Figure 7 depicts the analogous merging process for the active late-G dwarf ξ Boo A, representing the somewhat simplified case of the Reference sample binaries ξ Boo and 70 Oph. Unlike the original EclipSS targets, the four Cycles stars are too bright at Lyα to use CENWAVE 1291, which in any event is only allowed two FP-POS steps (instead of all four for the chosen CENWAVE 1222: the full complement of splits is important for fixed pattern noise suppression). The detector gaps are visible in the logarithmic flux density display as the two dropouts, one at Lyα, the other at 1525 Å. The only significant diagnostic lost with the use of G130M-1222 is semi-permitted O V 1218 Å, which however

forms at a similar temperature to the N V 1238 Å + 1242 Å doublet, the latter fully captured by CENWAVE 1222. The G130M-1222 and G160M-1533 CENWAVEs now overlap in a smaller interval, 1342–1362 Å, which nevertheless contains chromospheric Cl I 1351 Å, a narrow fluoresced line that is useful as a wavelength zero-point reference; as well as the two coronal forbidden lines mentioned earlier. Given the smaller G130M/G160M overlap, the use of all four FP-POS for each CENWAVE, and the dominance of the stellar O I emissions over the airglow counterparts for these bright stars, the merging of the two tracings was more straightforward than for the fainter, multi-epoch EclipSS subsample. The CENWAVE 1222 spectrum is shown in blue, and the CENWAVE 1533 spectrum in red. Again, the slightly smoothed merged spectrum is the dark curve, and the heavily filtered photometric error, now $1\,\sigma$, is the thin dark dotted-dashed tracing below the main spectrum. The extended wings of the strong chromospheric Lyα feature can be seen to either side of the G130M-1222 detector gap. There also is a conspicuous Si I photoionization continuum in the middle of the spectrum, falling toward shorter wavelengths. Unfortunately, the flux bump-up at the edge itself is hidden by the G160M-1533 detector gap. The S/N in the COS ξ Boo spectrum is remarkably high for a single-orbit exposure, far eclipsing what would be possible with the sister STIS instrument. On the other hand, the bright Reference stars of this program—α Cen AB and Procyon—are too intense in the FUV for COS, and can benefit from the higher resolution and wavelength precision delivered by earlier generation STIS.

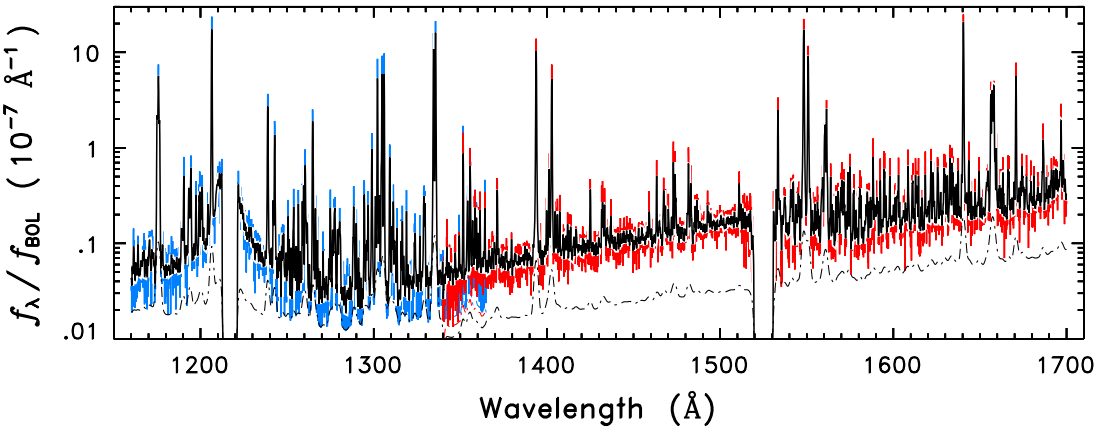

Figure 7. Merged, co-added COS G130M-1222 + G160M-1533 spectrum of ξ Boo A. The CENWAVE 1222 tracing is shown in blue, and the CENWAVE 1533 tracing in red. The dark curve is the slightly smoothed merged spectrum. The thin dotted-dashed tracing is the heavily filtered $1\,\sigma$ photometric error.

The final example, ϵ Eri, is illustrated in Figure 8. This is an extreme case compared with the previous ones, because of the large collection of COS CENWAVES available from both the G130M and G160M gratings. As mentioned earlier, the separate overlapping CENWAVEs play somewhat the same role, in terms of detector fixed pattern suppression, as the smaller wavelength shifts of the FP-POS splits within a single CENWAVE. The figure depicts the merged, co-added FUV spectrum from a COS-Team wavelength calibration exercise in 2017 August. There were twelve independent CENWAVEs recorded, although only eight (see below) were merged here: five G130M, including CENWAVE 1222 used in EclipSS and Cycles, and three G160M (CENWAVE 1533 of the new stellar programs was not included in the calibration suite: it was introduced more recently). All the

exposures were 2 ks, or deeper, and all were obtained at the single FP-POS= 3. Further, most of the G130M CENWAVEs were observed only on the A side of the detector, to avoid the bright Lyα emission of the active K dwarf. The exceptions were CENWAVEs 1222 and 1223, for which Lyα falls in the detector gap and thus both sides of the XDL camera could be activated. (Incidentally, the CENWAVE 1223 is not currently supported, in favor of 1222.) The other six CENWAVEs—1291, 1309, 1327, 1577, 1600, 1623—received the deepest exposures in an earlier wavelength calibration effort in 2017 March, as did the three G130M settings in the G130M-only campaign in 2021 February. Given the larger number of grating CENWAVEs available for ϵ Eri, compared with EclipSS or Cycles, the merging and co-addition process naturally was more complex.

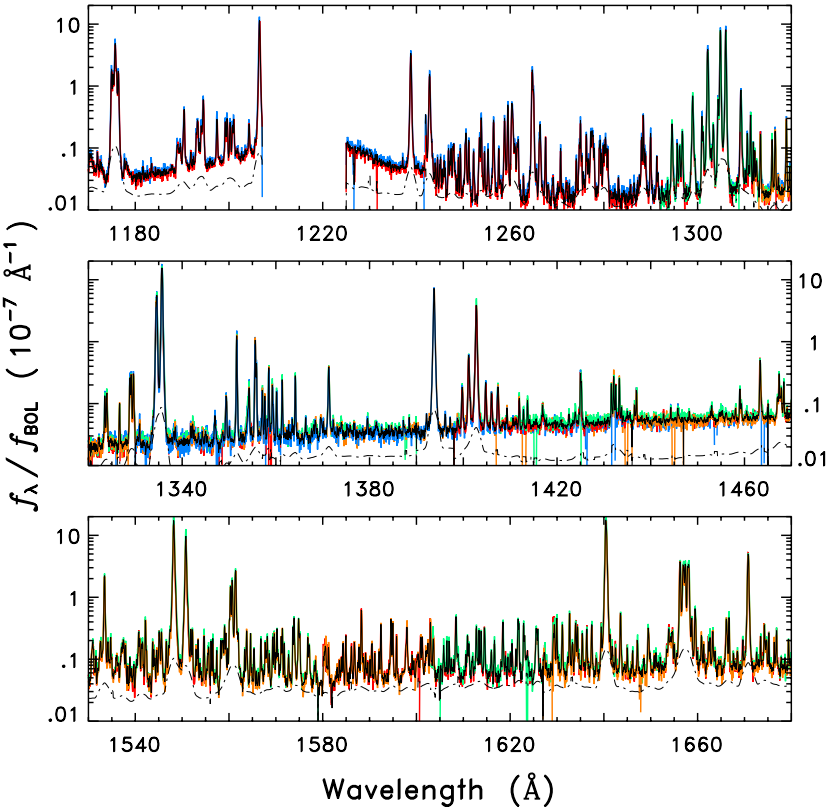

Figure 8. Merged, co-added COS spectrum of ϵ Eri from a COS-Team wavelength calibration exercise in 2017 August. The individual settings are represented by different colors, and the merged tracing is the darker curve. The thin dark dotted-dashed curve is the 5 σ photometric noise, demonstrating the exceptional S/N of the spliced spectrum.

As in the previous figures of this type, the individual settings are represented by different colors, and the (slightly smoothed) merged tracing is the darker curve. The displayed 5 σ photometric noise highlights the very high S/N (technically several hundred, but in practice limited by incomplete fixed pattern suppression). Thanks to the co-addition of overlapping deep exposures, a wealth of chromospheric and higher temperature emission lines has emerged. Note, for instance, the cluster of semi-permitted O IV (and S IV) features surrounding the 1402 Å component of the Si IV doublet. Normally, these density-sensitive emissions are too faint to be seen, aside from perhaps the brightest, O IV 1401 Å.

2.4. *FUV Spectral Comparisons*

Before describing the detailed measurements of the FUV emission lines of the EclipSS subsample, the Related objects, and the Reference stars, it is instructive to compare, in Figures 9a–c, respectively, the relative behaviors of key emission features. The figures highlight selected emission lines of the FUV region, as noted in the upper headings. The x-axis scale is the wavelength displacement relative to the laboratory value, expressed in equivalent velocity units. The Cl I line in most cases provided the calibration of the wavelength zero-point, except for one of the broad-lined stars, where the normally sharp chromospheric feature is washed out. The y-axis is the bolometrically normalized flux density.

Fig. 9a is for the EclipSS subsample, exclusively merged COS spectra. Red curves highlight the fastest rotators, all early-F stars (note the broad profiles of the three upper tracings). Green curves are for the moderate rotators. The dark or open points represent the slow rotators. Abbreviated identifications to the right concatenate the spectral type and first three digits of the HD number.

Fig. 9b is for the Related objects. All the spectra shown here are from STIS (several of the stars have companion COS observations as well). The STIS spectrum of EK Dra is lower in S/N than the associated COS series, but it captures important transitions, like Si III 1206 Å and N V 1238 Å, which are absent from the COS tracings because the side-B detector had to be deactivated owing to Lyα safety concerns. All the stars in this figure are moderate to fast rotators (the fastest, EK Dra, is highlighted in red), except τ Cet (in blue) which is a slow rotator (note the additional factor of ten boost of the normalized flux densities to allow the profiles to be visible on the chosen y-axis scale).

Fig. 9c is for the Reference sample. Here, color-coding highlights the STIS examples: α Cen AB and Procyon. All the stars in this figure are slow or moderate rotators. Dark and open symbols refer to ϵ Eri and the Cycles binaries, all COS observations in this display (ϵ Eri has two STIS pointings as well). Note the generally broader lines of the subgiant Procyon, and the appearance of a central reversal in its C II 1335 Å profile due to high opacity.

Figure 9. Comparison of key emission lines of the FUV region. The x-axis scale is relative velocity: each column is $\pm$200 km s^{-1}. The y-axis is the bolometrically normalized flux density. Each major division, by which the individual spectra were shifted, is indicated at lower left. (a) The EclipSS subsample (all COS). Red curves highlight the fastest rotators, green curves are moderate rotators, and the dark or open points are the slow rotators. Each star is identified at the right by spectral type and first three digits of its HD number. (b) The Related objects (all STIS). Abbreviated star names are noted at right. The red curve is for the fast-rotator, EK Dra. The blue curve is for low-activity τ Cet (multiplied by 10 to be visible on this scale). (c) The Reference stars. Here, color-coding highlights the STIS objects: α Cen AB ("α") and Procyon ("Proc"). All the stars here are slow or moderate rotators. Dark and open symbols refer to ϵ Eri and the Cycles binaries, ξ Boo ("ξ") and 70 Oph ("70"), all observed by COS.

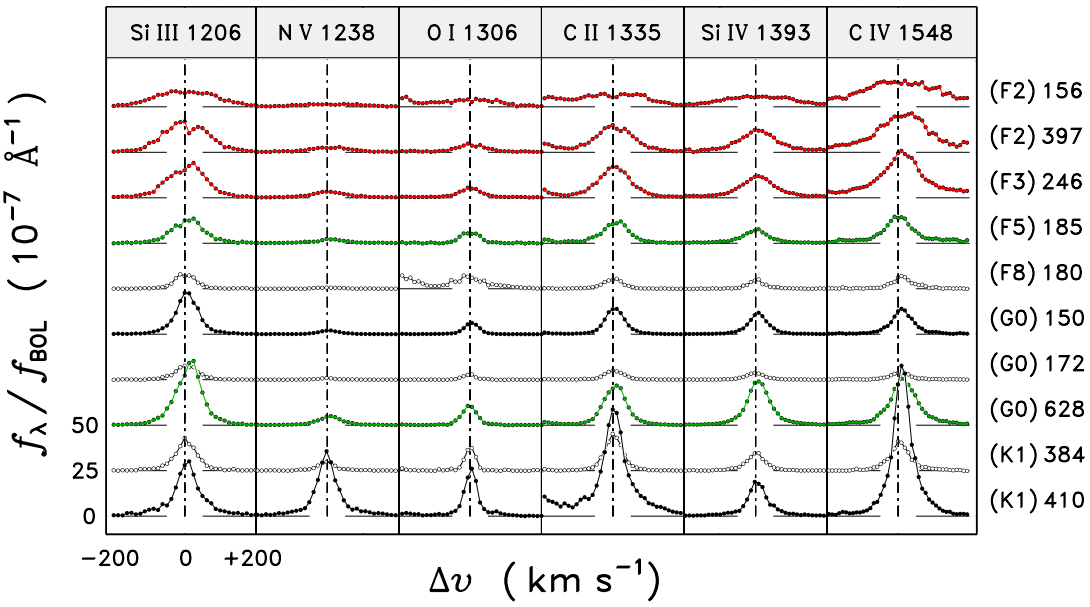

Figure 9a.

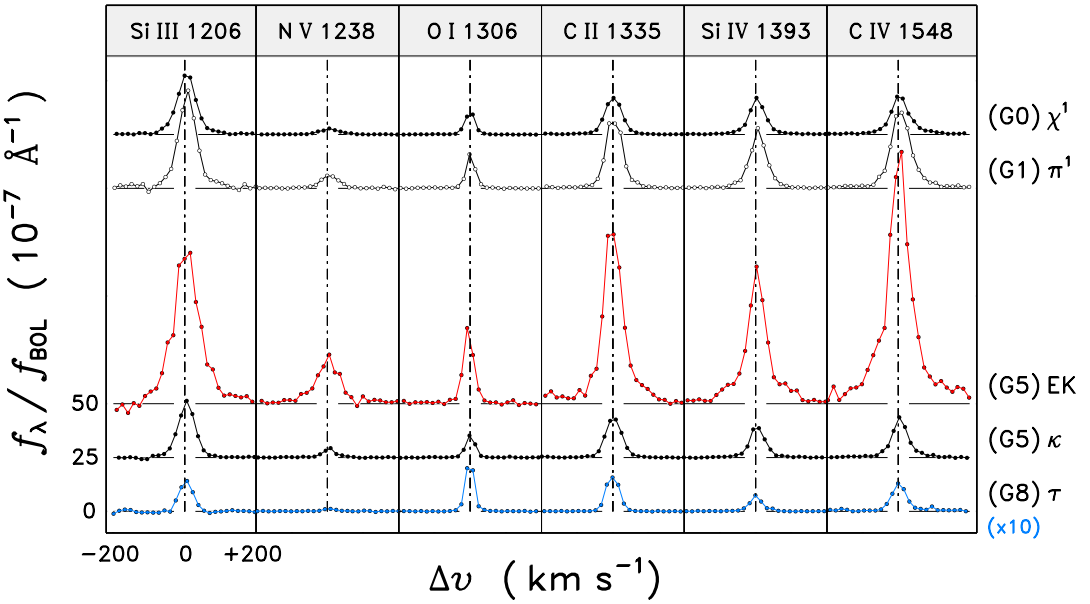

Figure 9b.

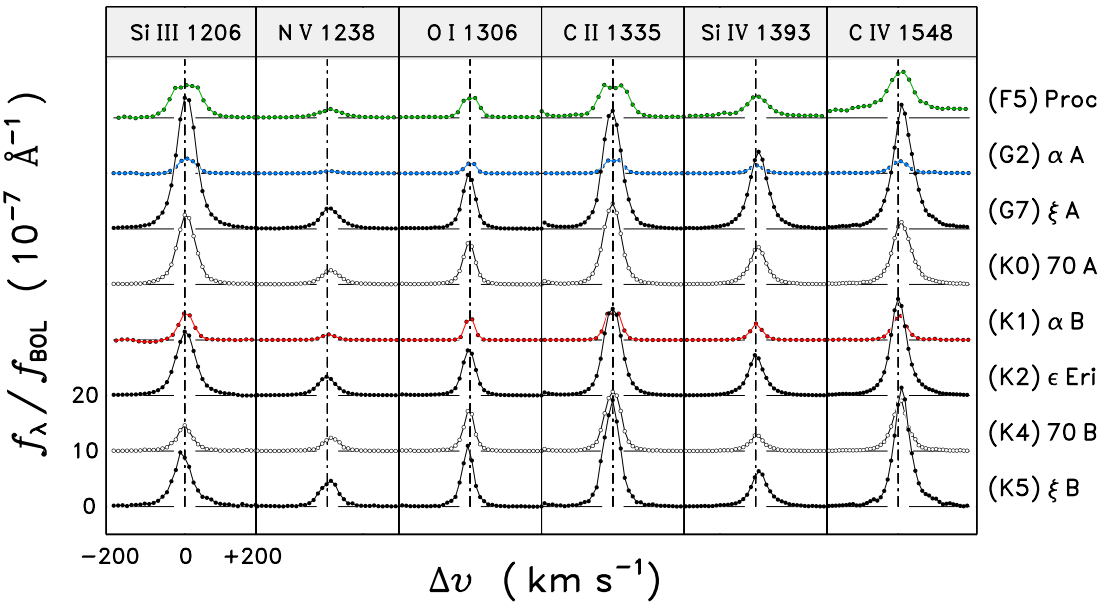

Figure 9c.

2.5. *Spectral Fitting*

This section describes the specialized spectral fitting carried out for the COS (or STIS) FUV tracings of the Total EclipSS stars, as motivated by the experience of Papers IV and V. Results are presented in a series of diagrams and tables later in the section. Several representative sample members will be utilized as examples to illustrate the fitting process, for both COS and STIS. Appendix B separately provides additional representative examples.

Paper IV introduced a pseudo-Gaussian model to fit the FUV emission-line profiles,

$$\phi(\lambda) = e^{-(|\lambda-\lambda_0|/\Delta\lambda_D)^a} \quad , \tag{1}$$

in which the normal pure-Gaussian exponent ($a = 2$) was allowed to take on arbitrary values. Here, λ_0 is the line-center wavelength and $\Delta\lambda_D$ is the characteristic e-folding line width. A pure Gaussian, as has been noted in prior solar and stellar work, tends to have a broader peak, slightly bowed sides, and narrower wings than typical observed TZ line shapes. In some previous studies, the mismatch was accommodated by introducing a bimodal Gaussian model in which a broad component provided the extended line wings, while a narrow component contributed the sharper central peak. However, Paper IV demonstrated that the simple pseudo-Gaussian model could replicate a diversity of solar line shapes, including the narrow-core and broad-wings of optically thin TZ lines, as well as the boxier profiles of optically thick chromospheric features. Paper V extended the approach to three of the current Reference Stars, α Cen AB and Procyon, with similar success.

In Paper V, the pseudo-Gaussian profiles matched the observed stellar FUV TZ line shapes better than pure Gaussians, unsurprising given the additional degree of freedom. Perhaps more intriguing was that the derived pseudo-Gaussian exponents not only were similar for different TZ lines in each star, despite a diversity of line widths, but also were similar among the stars, with values $a \sim 1.5$, significantly less than the pure-Gaussian case ($a = 2$).

For practical numerical reasons, the least-squares pseudo-Gaussian fitting algorithm restricted the exponent a to the range 1–5, which accommodated the vast majority of the STIS and COS profile shapes. Uncertainties in the modeling were assessed by a Monte Carlo approach, in which the best-fit profile was Gaussian-perturbed point-by-point according to the local photometric errors, then re-fitted, in numerous independent trials. The standard deviations of the derived parameters, especially the a exponent, over the many trials provided a measure of the parameter uncertainties.

Figures 10a–10e illustrate the profile fitting scheme, applied to the COS spectra of EclipSS subsample members HD 24636 (F3) and HD 150706 (G0) (co-added over two epochs); and COS spectra of Reference stars ϵ Eri (K2), ξ Boo A (G7), and 70 Oph A (K0). As alluded earlier, Appendix B has additional examples: STIS spectra of α Cen AB (G2 + K1), Procyon (F5), and ϵ Eri (K2); and COS spectra of ξ Boo B (K5) and 70 Oph B (K4). Note that all the illustrated spectra of the Reference stars, especially α Cen AB and Procyon, are for specific epochs (noted in the caption), rather than the (much higher-S/N) epoch-averages presented in previous installments of this Series.

In the figures, the panels depict 18 reference species, representing the chromosphere, TZ, or corona. The spectrum in each panel is normalized to a local intensity maximum, which might be contributed by an unrelated feature. Green dotted curves are smoothed $5\,\sigma$ photometric noise levels. Blue dashed lines under the emission features represent an adopted background continuum. The background emission levels, contributed typically by photoionization continua that vary smoothly with wavelength, were estimated through a hierarchical filtering of the flux densities in a large interval surrounding the target line of interest. See Paper I for details. The background levels were subtracted prior to the profile fitting. The continuum was allowed to be tilted for O V 1218 Å and coronal forbidden line Fe XII 1241 Å, to account for wings of nearby stronger emissions (Lyα and N V 1242 Å, respectively). Most of the target emission lines then were subjected to the pseudo-Gaussian modeling. Dark dots represent the specific fluxes included in the least-squares fit (although were ignored if negative relative to the continuum level). The resulting pseudo-Gaussian profile is illustrated by a red curve. If the model curve is absent, which is the case for noisy or spectrally complex features (e.g., the Si II 1264 Å blend, or Fe XXI, which is contaminated by an often stronger, but narrower, C I emission to the red), the highlighted intensities above the continuum level were numerically integrated. In some cases, such as O I 1355 Å, the fitting bandpass is asymmetric to account for a weak blend (C I 1355 Å, in that example), so that a more reliable measurement of the line flux could be obtained from the fitted profile, rather than, say, from a truncated numerical integration. The choices of which transitions to apply the pseudo-Gaussian fit, and the fitting bandpasses, varied from object to object, depending on the specific circumstances of the spectra. For example, the generally sharper lines of the higher resolution STIS spectra benefitted from narrower fitting bandpasses than the COS spectra of similar objects (although in the case of STIS ϵ Eri, illustrated in Appendix B, the fitting bandpasses were kept the same as for the COS spectra, for consistency). Further, several of the F-type EclipSS subsample stars have very broad lines, owing to high $v \sin i$, which benefitted from wider fitting bandpasses (see, also, Paper III).

Fig. 10a depicts spectral fits for the early-F star HD 24636. The emission lines are broad, as seen especially in the components of the C III 1175 Å multiplet, which normally are more distinct but here are merged together. The Fe XII coronal forbidden lines are weak, and Fe XXI is not evident, but rather its panel is dominated by the FUV continuum of the warm star. Fig. 10b is for the early-G dwarf HD 150706. The COS emission lines now generally are narrower, and the Fe XII lines are

prominent. Some Fe XXI emission appears to be present, but the red peak is still dominated by the C I blend. Fig. 10c illustrates the early-K dwarf ϵ Eri. This multiple-CENWAVE COS co-add has very high S/N, although there is an uncorrected fixed pattern dip in the blue wing of Fe XII 1241 Å (which nevertheless is somewhat mitigated by the spectral fit). Note that O V 1218 Å is missing here (and in subsequent Figs. 10d and 10e as well), a casualty of the detector gap in G130M-1222. The superior S/N reveals a weak, broad Fe XXI component merging into the sharp C I line to the red. Fig. 10d is for a high S/N COS spectrum of the late-G dwarf ξ Boo A. This tracing shows less blending in the C III multiplet, indicating a more modest rotational velocity than previous example HD 24636 (Fig. 10a). The Fe XII lines both are prominent, but the Fe XXI feature is conspicuous as well, albeit with a red peak due to the narrow C I line (as for ϵ Eri). The He II 1640 Å line is strong, without any obvious Fe II contamination (on the blue side, more evident in STIS α Cen A, shown in Appendix B, Fig. B1a). Fig. 10e is for the early-K dwarf 70 Oph A. The Fe XII lines are strong, while Fe XXI is weak and dominated by the C I blend, but otherwise the spectrum is similar to that of ξ Boo A.

Figure 10. Schematic depiction of the emission line profile fitting process. All the examples are from COS. The observed spectrum (thin dark curve) in each panel is normalized to a local intensity maximum. The original spectrum was resampled into uniform 0.05 Å bins ($\sim$ 0.7 resolution element (resel)). Vertical dotted-dashed lines represent the laboratory wavelengths in the stellar (photospheric) reference frame. Green dotted curves are the smoothed $5\,\sigma$ photometric error. Blue dashed lines under the emission features represent an adopted background level, based on a long-range continuum model. The continuum is tilted for O V 1218 Å and Fe XII 1241 Å, to account for wings of nearby stronger emissions. Dark dots represent the specific points included in the pseudo-Gaussian modeling. The fitted profile is illustrated by a red curve. If the model curve is absent, the highlighted intensities above the background level were numerically integrated. (a) HD 24636 (F3). (b) HD 150706 (G0). (c) ϵ Eri (K2: 2017 August). (d) ξ Boo A (G7: 2020 February). (e) 70 Oph A (K0: 2020 September).

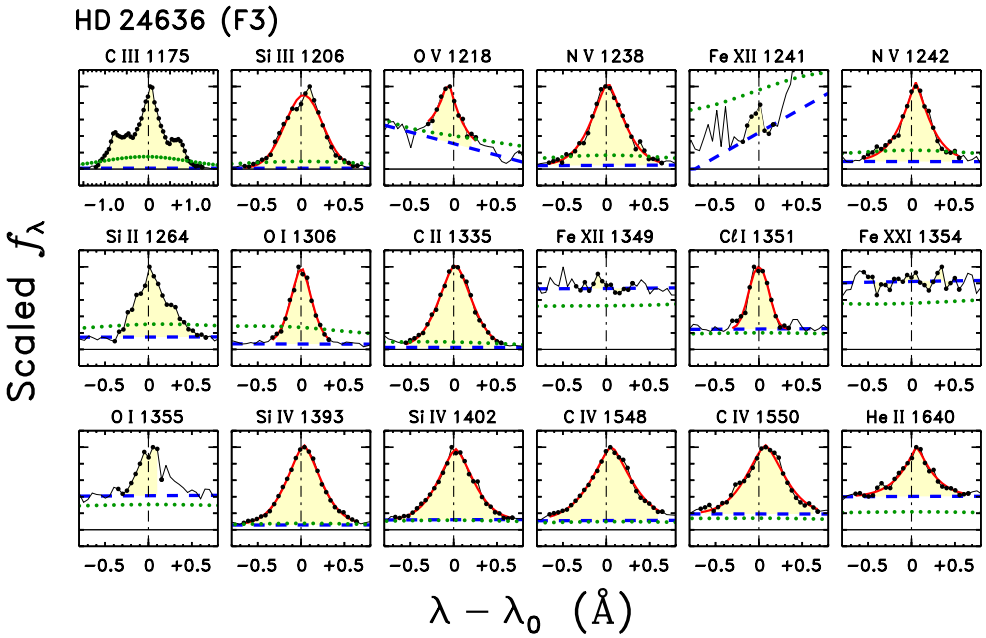

Figure 10a.

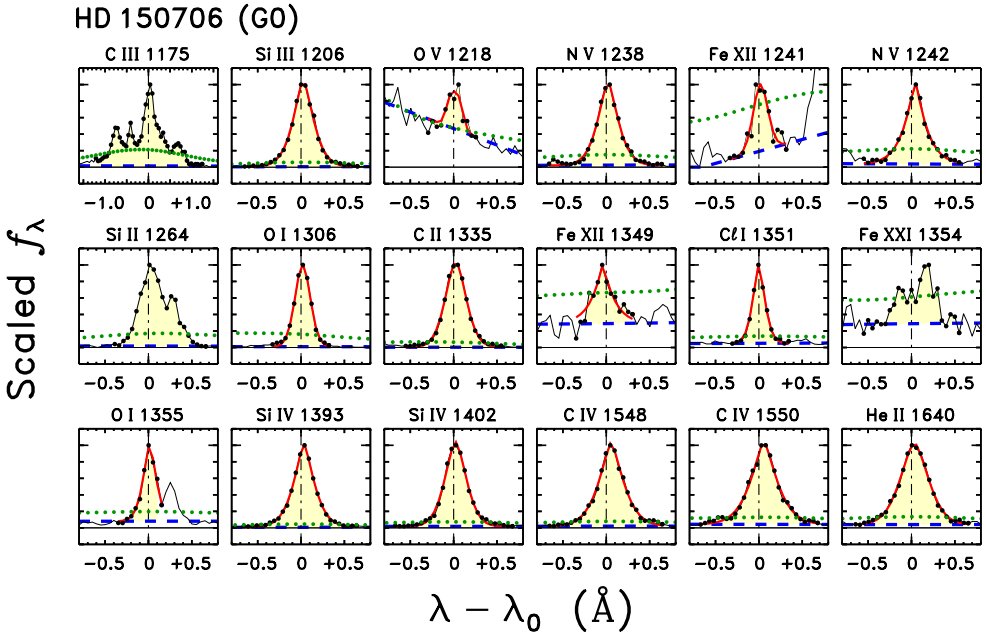

Figure 10b.

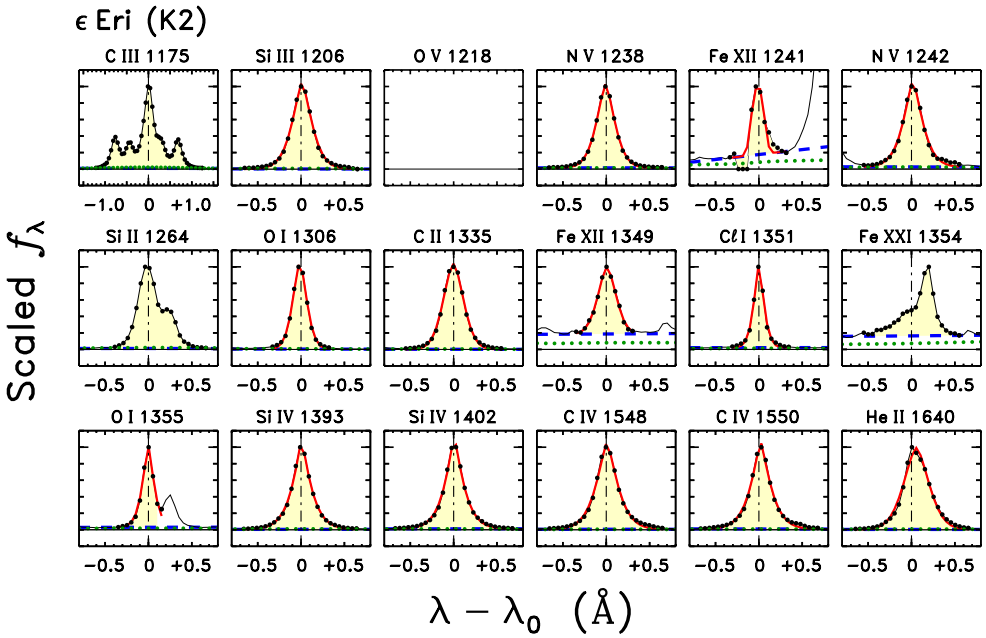

Figure 10c.

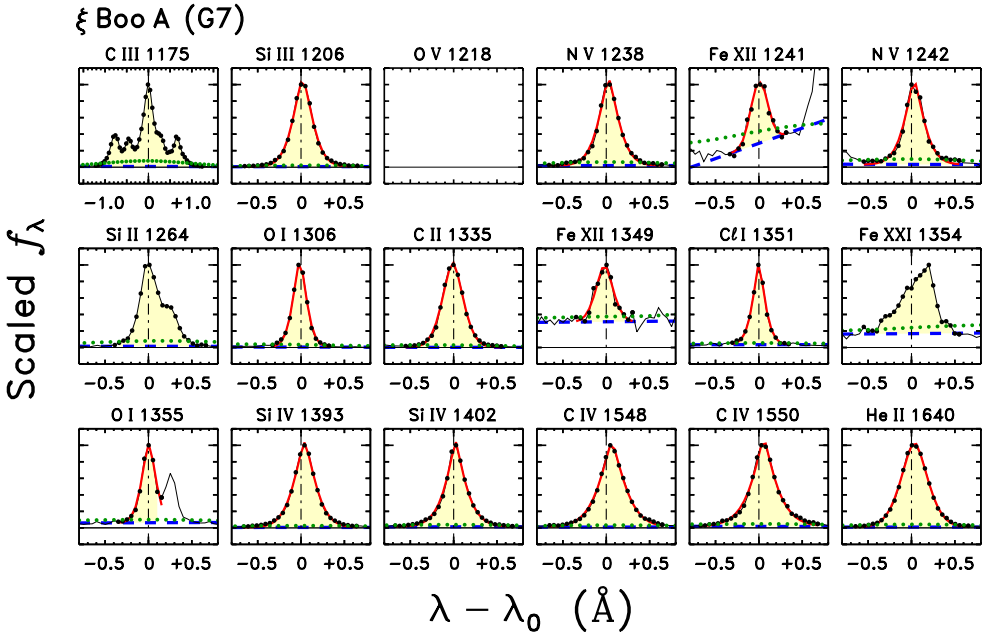

Figure 10d.

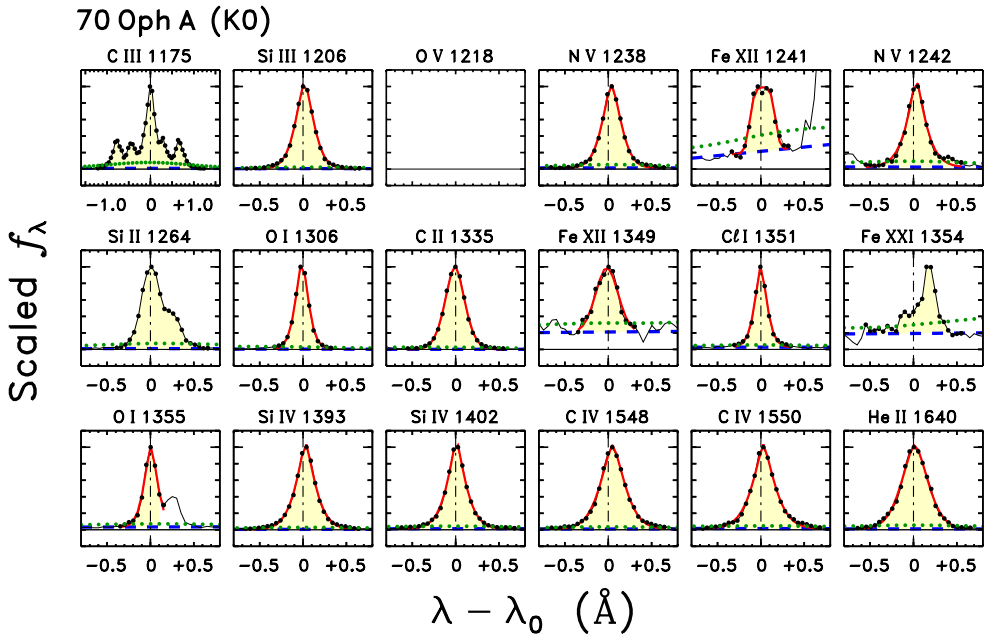

Figure 10e.

Table 5 lists measured fluxes (expressed as f_L/f_{BOL}) of representative FUV features from the Total EclipSS sample. In most cases, the fluxes were the result of pseudo-Gaussian profile modeling, where in some cases the wings of the fitted symmetrical line shape extrapolated over blends by design. An example is O I 1355 Å (Figs. 10(b)–(e)), which is affected by a weaker C I 1355 Å emission to the red. The O I modeling range was restricted mainly to the blue wing, but then the symmetric red wing of the fitted profile nicely excluded the red blend, so that the analytically integrated total profile flux would be more accurate than, say, adopting a truncated numerical integration to explicitly avoid the C I blend. In other situations, for example the Si II 1264 Å close doublet, the single-component pseudo-Gaussian modeling was not appropriate, but given the lack of significant accidental blends, the feature could be numerically integrated with sufficient accuracy.

The Sun is included in the table, based on averages of FUV irradiances over solar Cycle 24 (see Paper I). Several of the reference emission lines are missing from the solar tabulations, for example O V 1218 Å and O I 1355 Å, because they were too blended with neighboring features (Lyα and C I 1355 Å, respectively) to be disentangled in the relatively low spectral resolution irradiance scans. Further, the single lines O I 1306 Å and C II 1335 Å were scaled from blended features in the solar scans, O I 1304 + 1306 and C II 1334 + 1335, according to ratios deduced from high-resolution spectra of α Cen A (see Paper V).

An additional nuance is that several of the sample members, mainly the Reference stars, have multiple epochs of observations, sometimes with full FUV coverage (STIS E140M), but at other times only partial (COS G130M, Side B deactivated). In such cases, standard deviations were calculated over whichever epochs were available for each specific spectral feature, and listed as the flux uncertainty. For the more typical situation, where only one or two independent FUV spectra were available, the cited uncertainty either is the statistical error reported by the pseudo-Gaussian procedure, if only a single observation; or half the absolute difference between two observations,

otherwise. Unfortunately, given the range of possibilities, it was not practical to flag each uncertainty as to its specific origin. Nevertheless, the typical ranges are much smaller for the FUV lines than for the corresponding X-ray fluxes, so any associated FUV error bars generally would be unnoticeable in subsequent (log–log) diagrams.

Table 5. Total EclipSS FUV Fluxes

Species	$\log T_{MAX}$ (K)	—	—	f_L/f_{BOL} (10^{-7})	—	—
1	2	3	4	5	6	7
			EclipSS Subsample			
		HD 24636	HD 38459	HD 39755	HD 41004	HD 62850
C III 1175	4.8	8.53±0.08	3.33±0.10	7.95±0.12	20.10±0.24	6.23±0.07
Si III 1206	4.7	9.26±0.08	5.07±0.09	9.81±0.12	10.40±0.17	12.50±0.09
O V 1218	5.3	0.83±0.05	0.63±0.07	0.83±0.08	1.16±0.17	0.66±0.07
N V 1240	5.2	2.38±0.03	1.88±0.04	2.29±0.05	16.15±0.14	2.72±0.03
Si II 1264	(3.8)	0.447±0.017	0.74±0.03	0.51±0.03	1.16±0.04	1.100±0.019
O I 1306	(3.9)	1.54±0.05	2.15±0.09	1.44±0.07	5.23±0.14	2.46±0.05
C II 1335	4.5	8.13±0.07	5.52±0.07	7.85±0.10	22.80±0.21	7.96±0.06
Fe XII 1349	6.2	0.010±0.004	0.052±0.007	0.021±0.009	0.028±0.014	0.031±0.004
Cl I 1351	(3.8)	0.399±0.013	0.229±0.012	0.40±0.03	0.588±0.017	0.403±0.008
O I 1355	(3.9)	0.191±0.011	0.155±0.011	0.196±0.025	0.489±0.018	0.229±0.008
Si IV 1400	4.9	8.80±0.06	4.34±0.05	10.02±0.18	9.90±0.09	14.06±0.06
C IV 1550	5.0	20.55±0.16	8.32±0.10	21.5±0.4	45.4±0.3	19.17±0.12
He II 1640	4.9	4.01±0.16	3.97±0.10	4.3±0.3	20.40±0.25	9.61±0.11
		HD 150706	HD 156559	HD 172669	HD 180712	HD 185239
C III 1175	4.8	2.54±0.04	7.09±0.11	1.14±0.04	1.22±0.05	4.82±0.10
Si III 1206	4.7	7.33±0.06	6.82±0.11	2.45±0.04	2.36±0.05	5.79±0.10
O V 1218	5.3	0.30±0.05	0.23±0.05	0.15±0.04	0.20±0.05	0.37±0.07
N V 1240	5.2	1.008±0.019	1.59±0.05	0.350±0.013	0.300±0.018	1.44±0.04
Si II 1264	(3.8)	0.723±0.013	0.302±0.025	0.320±0.012	0.308±0.016	0.365±0.023
O I 1306	(3.9)	1.41±0.03	1.78±0.10	0.58±0.03	···	1.64±0.07
C II 1335	4.5	4.48±0.04	5.55±0.09	1.510±0.025	1.63±0.03	4.86±0.08
Fe XII 1349	6.2	0.025±0.003	0.011±0.007	0.017±0.003	0.016±0.005	0.018±0.006
Cl I 1351	(3.8)	0.186±0.005	0.188±0.020	0.061±0.005	0.072±0.011	0.278±0.014

Table 5 *continued on next page*

Table 5 *(continued)*

Species	$\log T_{MAX}$	—		f_L/f_{BOL}	—	
	(K)			(10^{-7})		
1	2	3	4	5	6	7
O I 1355	(3.9)	0.140±0.005	0.090±0.017	0.078±0.005	0.105±0.013	0.166±0.012
Si IV 1400	4.9	5.62±0.03	6.89±0.09	1.677±0.018	2.07±0.06	4.53±0.06
C IV 1550	5.0	7.93±0.07	16.18±0.25	1.93±0.04	3.28±0.08	9.74±0.18
He II 1640	4.9	4.74±0.07	3.40±0.25	0.99±0.04	1.57±0.08	2.39±0.19
Related objects (G-type dwarfs)						
		τ Cet	κ Cet	χ^1 Ori	π^1 UMa	EK Dra
C III 1175	4.8	0.23	3.2	4.0	7	26
Si III 1206	4.7	0.27	6	7	11	29
O V 1218	5.3	0.06	0.46	0.44	0.6	2.2
N V 1240	5.2	0.041	1.2	1.1	2.1	10
Si II 1264	(3.8)	0.07	0.7	0.7	1.1	1.9
O I 1306	(3.9)	0.31	1.68±0.14	1.62±0.06	2.39±0.04	23.0±11.1
C II 1335	4.5	0.33	5.2±0.5	5.2±0.6	7.7±0.7	33.5±9.0
Fe XII 1349	6.2	···	0.035±0.001	0.031±0.003	0.045±0.017	0.064±0.010
Cl I 1351	(3.8)	0.023	0.237±0.003	0.225±0.001	0.35±0.06	1.11±0.11
O I 1355	(3.9)	0.06	0.160±0.010	0.160±0.005	0.22±0.03	0.73±0.15
Si IV 1400	4.9	0.22	6.2±0.5	8.0±1.2	10.6±0.6	41.4±15.3
C IV 1550	5.0	0.49	8	8	17	154.5±141.8
He II 1640	4.9	0.17	4.6	5	10	77.3±55.8
Reference sample						
		Sun	ϵ Eri	Procyon	α Cen A	α Cen B
C III 1175	4.8	0.40±0.04	3.07±0.10	2.23±0.09	0.40±0.03	0.68±0.11
Si III 1206	4.7	0.71±0.12	3.40±0.14	2.55±0.06	0.69±0.07	1.08±0.21
O V 1218	5.3	···	0.56±0.09	0.314±0.013	0.077±0.009	0.15±0.04
N V 1240	5.2	0.141±0.014	1.37±0.05	0.812±0.022	0.157±0.011	0.31±0.08
Si II 1264	(3.8)	···	0.614±0.025	0.172±0.007	0.116±0.008	0.25±0.04
O I 1306	(3.9)	0.340±0.020	1.71±0.05	0.88±0.03	0.331±0.016	0.58±0.10
C II 1335	4.5	0.73±0.08	4.5±0.3	2.52±0.07	0.72±0.04	1.4±0.3

Table 5 *continued on next page*

Table 5 *(continued)*

Species	$\log T_{MAX}$	—		f_L/f_{BOL}	—	
	(K)			(10^{-7})		
1	2	3	4	5	6	7
Fe XII 1349	6.2	0.004±0.001	0.027±0.003	0.005±0.001	0.002±0.001	0.011±0.003
Cl I 1351	(3.8)	0.043±0.002	0.184±0.011	0.251±0.012	0.048±0.002	0.054±0.010
O I 1355	(3.9)	···	0.166±0.005	0.185±0.007	0.070±0.002	0.085±0.009
Si IV 1400	4.9	0.50±0.08	3.20±0.15	2.07±0.14	0.54±0.05	0.94±0.21
C IV 1550	5.0	1.05±0.10	8.4±1.3	4.79±0.22	1.09±0.08	1.8±0.4
He II 1640	4.9	···	6.3±1.0	0.64±0.05	0.13±0.03	0.57±0.14
		ξ Boo A	ξ Boo B	70 Oph A	70 Oph B	
C III 1175	4.8	5.07±0.12	3.82±0.08	2.36±0.12	1.7±0.3	
Si III 1206	4.7	7.32±0.03	2.73±0.09	3.58±0.04	1.4±0.3	
O V 1218	5.3	···	···	···	···	
N V 1240	5.2	1.77±0.05	1.83±0.08	1.104±0.012	1.13±0.20	
Si II 1264	(3.8)	0.905±0.012	0.553±0.019	0.641±0.008	0.42±0.03	
O I 1306	(3.9)	2.12±0.07	2.07±0.03	1.47±0.05	1.49±0.14	
C II 1335	4.5	6.91±0.17	5.16±0.06	4.09±0.22	3.4±0.5	
Fe XII 1349	6.2	0.028±0.002	0.023±0.004	0.024±0.001	0.018±0.002	
Cl I 1351	(3.8)	0.298±0.017	0.204±0.013	0.160±0.005	0.128±0.021	
O I 1355	(3.9)	0.181±0.004	0.183±0.007	0.147±0.003	0.140±0.019	
Si IV 1400	4.9	6.95±0.05	3.10±0.09	3.3±0.3	1.30±0.12	
C IV 1550	5.0	13.2±0.3	10.4±0.3	6.50±0.24	5.0±0.7	
He II 1640	4.9	10.25±0.25	10.9±0.3	3.57±0.05	3.5±0.5	

NOTE—Col. 1 is the FUV emission species, in some cases the sum of doublet (C IV 1550 Å) or multiplet (C III 1175 Å) components. Col. 2 is the temperature of maximum emissivity for optically thin transitions in Collisional Ionization Equilibrium (CIE) from CHIANTI (see: https://www.chiantidatabase.org/chianti_linelist.html). Values in parentheses are estimates for species that form in the optically thick chromosphere. Cols. 3–7 list f_L/f_{BOL} ratios (in units of 10^{-7}), and $1\,\sigma$ uncertainties (same units) for the indicated stars in the rolling headings.
[a]Assuming the f_{BOL} of the K dwarf primary. However, the M dwarf secondary might well dominate the high-energy emissions of the system (see discussion in subsequent Rotation section).

Table 6 summarizes pseudo-Gaussian fitting parameters for the nine stars of the sample that have STIS E140M spectra, mostly G-types. The STIS medium-resolution echelle has several times the spectral resolution of the COS G modes, which is important for assessing the emission line widths, especially the narrow chromospheric features Cl I 1351 Å and O I 1355 Å. Further, STIS has a much more stable and precise wavelength scale than COS, essential for measuring the sometimes subtle

Doppler shifts of the stellar features (which requires establishing the wavelength zero-point empirically, according to narrow low-excitation species, against which all the other features are referenced). Procyon and α Cen B also have a series of E140H high-resolution echelle spectra, in addition to 6–10 medium-resolution exposures each. Just the E140M spectra were retained here for the sake of uniformity, mainly because the remaining seven stars only have E140Ms. (Small, but systematic, differences between the medium-resolution and high-resolution profiles of Procyon and α Cen B were illustrated in previous Paper V.) The fitted pseudo-Gaussian profile was assumed to be symmetric, and the controlling exponent, a, was limited by the least-squares fitting algorithm to the range 1–5 ($a = 2$ is the normal Gaussian). The lower end is a pure exponential (sharply peaked profile), while the upper end is a rounded boxy line shape. The latter is characteristic of optically thick lines, which have insipient (or more developed) central reversals (see Paper V), but was encountered here with one narrow feature that had an accidental downward noise spike in the center of the profile (O I 1355 Å of EK Dra).

Parameter values (pseduo-Gaussian exponents, Doppler shifts, and FWHMs) and uncertainties for the main Reference stars, Procyon and α Cen AB, were based on averages and standard deviations over all the epochs of the STIS E140M exposures. Uncertainties for the other (single-epoch) stars are not listed if the species consisted of a single transition. (Given the normally high S/N of the exposures of these bright stars, the single-measurement errors typically are better than ± 10 % for FWHM and a, and ± 0.7 km s^{-1} for Δv.) The single-epoch value and uncertainty for a doublet species is the average of the two separate parameter values and one-half the absolute value of the difference, respectively. The (usually bright) narrow Cl I 1351 Å line was adopted as the fundamental velocity reference for each spectrum, thus the velocity shifts for the chlorine line reported in the Table uniformly are zero. Thoughts concerning Table 6 will be deferred until the Analysis section.

Table 6. Stellar Pseudo-Gaussian Profile Parameters (STIS E140M, only)

Name:		Procyon	χ^1 Ori	π^1 UMa	α Cen A	EK Dra	κ Cet	τ Cet	α Cen B	ϵ Eri
SpTyp:		F5	G0	G1	G2	G2	G5	G8	K1	K2
Cl I 1351	Δv	0.0	0.0	0.0	0.0	0.0	0.0	0.0	0.0	0.0
	FWHM	22.5±0.2	23.2	19.6	17.2±0.6	22.8	12.3	13.2	15.1±0.6	12.8
	a	1.80±0.03	2.02	1.60	1.76±0.06	2.04	1.27	1.61	1.69±0.07	1.65
O I 1355	Δv	0.0±0.2	−1.2	0.6	−0.1±0.3	−1.5	0.9	−1.1	−0.2±0.2	0.2
	FWHM	19.3±0.8	21.2	11.7	16.6±0.5	34.6	16.4	14.0	15.1±0.5	13.1
	a	1.50±0.04	2.15	1.00	1.60±0.06	5.00[a]	1.97	1.83	1.57±0.04	1.58
Si III 1206	Δv	4.4±0.4	4.8	5.7	5.7±0.4	7.1	6.4	4.4	4.9±0.3	4.2
	FWHM	99.4±1.2	53.8	55.7	58.2±0.9	71.2	49.9	42.1	45.5±1.0	41.5
	a	2.26±0.04	1.48	1.55	1.97±0.05	1.25	1.52	1.68	1.70±0.06	1.41
Si IV 1400	Δv	4.6±0.3	4.4±0.1	5.3±0.1	3.8±0.4	5.1±0.1	5.2±0.1	2.4±0.7	3.0±0.3	2.7±0.2
	FWHM	61.5±1.2	40.5±0.8	43.3±0.2	42.5±0.7	47.2±1.5	36.0±2.8	36.2±5.2	33.7±0.8	25.9±1.0
	a	1.41±0.03	1.27±0.01	1.24±0.03	1.45±0.02	1.00	1.25±0.06	1.46±0.22	1.32±0.05	1.04±0.04
C IV 1550	Δv	5.7±0.3	5.0	5.4±1.0	4.9±0.3	5.2±0.8	5.4±0.9	2.5±0.8	3.1±0.4	2.9±0.2
	FWHM	69.8±1.0	49.0±0.4	52.9±3.3	50.4±0.8	51.5±4.3	42.5±1.1	39.5±2.3	40.0±1.5	28.0±0.9
	a	1.57±0.03	1.39±0.05	1.49±0.08	1.58±0.03	1.02±0.03	1.25±0.05	1.50±0.03	1.45±0.08	1.08±0.03
N V 1240	Δv	7.4±0.4	4.8±0.8	4.3±1.3	5.3±0.5	2.8±1.9	5.9±0.5	1.5±0.7	3.3±0.2	3.6±0.4
	FWHM	67.5±0.8	48.3±3.5	50.3±1.9	49.5±2.2	49.0±0.9	43.3±1.1	46.0±7.1	41.6±1.1	33.7±1.2
	a	1.35±0.02	1.30±0.01	1.46±0.10	1.54±0.08	1.00	1.39±0.09	2.39±1.21	1.51±0.06	1.27±0.04
O V 1218	Δv	6.0±1.1	6.8	3.3	4.8±1.5	6.1	4.4	6.7	3.0±1.0	5.5
	FWHM	65.2±2.7	47.6	51.9	49.8±3.3	65.8	29.4	23.5	42.0±3.3	43.1
	a	1.63±0.14	1.77	1.56	2.07±0.53	1.70	1.01	1.00	2.14±0.45	1.48
He II 1640	Δv	9.9±1.1	4.5	6.5	−2.4±1.6	8.1	4.9	−4.2	1.5±0.9	4.5
	FWHM	55.9±1.8	50.9	49.8	57.3±5.7	55.8	50.5	72.2	48.5±1.5	46.0
	a	1.59±0.16	1.54	1.52	1.73±0.42	1.56	1.57	1.98	1.49±0.07	1.62

Note—Δv is the line center shift in km s^{-1}; FWHM is the full width at half maximum intensity of the profile, also in km s^{-1}; and a is the pseudo-Gaussian exponent ($a = 2$ is the normal Gaussian). See text for description of how the parameter values and uncertainties were determined for the multi-epoch versus the single-epoch examples.

[a]Noisy profile with downward spike in center, fitted by boxy line shape.

2.6. *Measures of Stellar Rotation*

Rotation periods derived from spot or plage modulations in broad-band optical photometry, or narrow-band chromospheric Ca II HK, can be superior to the other main source of spin rates—the projected photospheric rotational velocity, $v \sin i$—because often the inclination of the stellar spin axis, i, is unknown, and the diminution factor, $\sin i$, can become quite small if the star is viewed nearly pole-on. To be fair, photometric periods can also be ambiguous if one happens to catch a time when a harmonic of the true rotation period is dominant, because, say, bright patches are on opposite hemispheres of the star in that epoch. Another situation is when bright and dark patches are spatially mixed across the stellar latitudes, so that the photometric signal is inconsistently modulated. Usually, such ambiguities can be resolved by examining suitably long photometric records, in which eventually one side of the star dominates the variability signal and the fundamental period shines through. In the situation where harmonics of the fundamental period are present on occasion, the guiding rule is that it is very unlikely to encounter a sustained interval in which, say, a multiple the fundamental period is encountered (there are caveats to the rule for time series that have regularly spaced gaps, like the 13.5 d telemetry interludes of TESS). Longer periods than the fundamental certainly are possible if strong evolution of the active regions is occurring, but in general such evolution would not proceed smoothly enough, in positive and negative senses, for long enough to be mistaken as the fundamental period. The analogous rule for the $v \sin i$ case is that the projected rotational velocity should not exceed the equatorial $v_{\rm ROT}$. Thus, the projected rotational velocity can serve as a check on a photometric rotation period, assuming that the stellar radius can be deduced independently, which is the case for nearby stars with Gaia parallaxes, G magnitudes, and $(BP - RP)$ colors (see Paper III).

There is an additional caveat. The photometric rotation period is representative of particular latitudes on the star where the spots and/or plage are present during the time frame of the observations. The Sun rotates differentially, and apparently so do other cool stars (see Donahue et al. 1996). Further, the birth of active regions on the Sun migrates over the course of the magnetic cycle, beginning at mid-latitudes at the cycle onset, but drifting toward the equator as the cycle progresses (creating the so-called "butterfly pattern" of spot emergence over time). Thus, a star might display the photometric signatures of several different rotation periods during a decadal cycle. Some clarity was achieved by Donahue et al. (1996), who measured spin periods of about three dozen FGK stars from the Mt. Wilson Ca II HK program that had been monitored more regularly for a decade specifically for the purpose of assessing differential rotation. The authors reported that the dispersion in HK rotation periods, ΔP, for each star was roughly proportional to the period, P, itself; so that the percentage effect of the apparent differential rotation was approximately constant.

Consequently, differential rotation likely affects the other stars similarly to the Sun, where the influence is not large, because the gradient of the differential rotation is small across the zone typically occupied by active regions. In fact, Donahue et al. reported a range of chromospheric periods for the Sun of 22.9–26.6 d (sidereal), based on an analysis of disk-integrated solar Ca II K-line time series from Sacramento Peak Observatory. The lower period is slightly super-rotational (the equatorial sidereal period is 24.5 d), while the upper value would be characteristic of the mid-latitudes where active regions appear at the cycle onset. The Carrington rotation period of the Sun, which corresponds to an average latitude of spots ($\sim \pm 26^\circ$), is 25.4 d in the sidereal frame. That value was adopted here

for the solar rotation period (with an uncertainty of ±1 d to roughly account for the range reported by Donahue et al.).

The projected rotational velocity also captures the differential rotation to some extent because all parts of the visible hemisphere of the star contribute to the unresolved spectrum. However, considering the high-inclination case, the equatorial limbs contribute the most to the disk-average Doppler broadening because of the larger line-of-sight (LOS) velocities compared to the poles (for which the LOS velocities would further be reduced by differential rotation, if present and with a similar equator–pole decline as solar). Consequently, the photometric period and projected rotational velocity sample nearly equivalent portions of the stellar disk. In the low-inclination case, the photometric period is not much affected, but the $v \sin i$ is diminished by the projection factor, and becomes more sensitive to the high-latitude differential rotation. In such situations, the $v \sin i$ no longer is a good check on the rotational period, but rather the ratio now is more useful to set limits on the projection factor.

Both the photometric and $v \sin i$ methods have limitations, and, unfortunately, the limitations are parallel, rather than orthogonal, affecting mainly the slow rotators. First of all, slow rotators like the Sun have long rotation periods, $\gtrsim 1$ month, requiring sustained photometric attention in the face of stochastic variations. (The Kepler satellite was very good at that, but of course was pointing at only a small patch of sky during its four-year main mission, capturing mainly more distant late-type dwarfs that are of less interest for follow-up studies.) Second, slow rotators usually are magnetically less active than their faster-rotating cousins, consequently the photometric modulation contrasts tend to be small, necessitating high-precision measurements from space (such as Kepler, and now TESS). Ca II HK time series from the ground, focusing on the more energetic chromospheric layers, are more practical from the contrast point of view, but require long-term dedicated facilities, such as the iconic Mt. Wilson survey, and so far only a relative handful of nearby bright stars have reliable HK rotation periods (e.g., Donahue et al. 1996; Baliunas et al. 1996). Third, current all-sky TESS observes a given part of the sky typically for only about a month, which is too short to adequately confirm a rotation period of that order, or longer, because at least several cycles should be counted to claim a solid detection, and even then there might be ambiguities with respect to harmonics. TESS is much better for rotation periods less than about 5 d, especially for high Ecliptic latitude stars (such as the EclipSS sample) for which several consecutive 27 d TESS sectors might be recorded, so that enough rotational cycles can be captured to distinguish between the fundamental and harmonics, and avoid intervals when the surface activity was too smoothy distributed to cause any detectable modulations.

Similarly, the projected rotational velocity method has significant limitations for slowly rotating stars, beyond the obvious uncertainty in the projection factor. First, detecting the extra broadening due to rotation requires high dispersion spectroscopy, certainly better than $R \equiv \lambda/\Delta\lambda \sim 100{,}000$ for $v \sin i \lesssim 2$ km s^{-1}, achieved with special purpose equipment normally not available at typical ground-based observatories. This limitation has eased in recent years with the introduction of several planet-hunting spectrographs at large optical telescopes for which high-resolution benefits the measurement of precision radial velocities. Unfortunately, many of the existing projected rotational velocities in the literature were obtained through the analysis of lower resolution material from older instruments.

A second limitation is related, namely the weak unblended photospheric absorption lines prized for rotational measurements are broadened by kinematic effects beyond rotation itself, lumped into the generic categories thermal, macroturbulent, and microturbulent velocities in the classical analysis framework (involving 1-D atmospheric models: see Gray 1976). These additional broadening mecha-

nisms introduce an undesirable background from which the rotational component must be extracted (and thereby also introduce a floor for the necessary spectral resolution). In reality, the macro/micro classification is a crude representation of the various spatial scales of flows and turbulence associated with hydrodynamic convection in the stellar photosphere. Even though the macro/micro parameters are imprecise descriptions of a complex physical phenomenon, they are useful for contrasting the size of the ancillary Doppler broadening that limits the detection of the rotational component. (Normally, $v \sin i$ measurements are restricted to heavy species, such as iron, to minimize the thermal part of the broadening, and optically thin lines to avoid the width-boosting effect of "saturation," which affects optically thick transitions.)

Typical values for $\xi_{\rm macro}$ and $\xi_{\rm micro}$ for the Sun (see Appendix C, Table C1) are 3–4 km s^{-1} and 1 km s^{-1}, respectively (FWHM of Gaussian profile), which would produce a combined line shape that would be at the resolution limit of a $R \sim 1{\times}10^5$ spectrograph. Helpfully, the rotational profile itself is super-Gaussian, more like an inverted-U shape, depending on the degree of limb darkening (see Gray 1976). The associated FWHM is a multiple of $v \sin i$, typically ~ 1.7, so the impact on the combined profile is accentuated. In fact, there are Fourier decomposition techniques (ibid) that take advantage of the near-Gaussian character of the kinematic broadening versus the super-Gaussian rotational profile. Nevertheless, it is clear that a $v \sin i$ smaller than about 2 km s^{-1} (the solar value) would be challenging to determine precisely because the extraneous dynamical broadening is comparable or larger. There is some relief from this restriction for the cooler, K-type dwarfs, which have more muted convective dynamics. Still, a $v \sin i$ below 1 km s^{-1} would likely be out of reach. Noting that many of the older K dwarfs have long rotation periods exceeding a month, and given the small sizes of the stars, the corresponding rotation periods would be at, or below, the cited threshold, even without considering projection effects.

2.6.1. *TESS Photometric Light Curve Analysis for the EclipSS Subsample*

The EclipSS subsample was well-suited for a TESS rotational modulation analysis. First, the targets are located near the Ecliptic poles, so most of them have multiple contiguous TESS sectors, possibly doubled given the two sky surveys carried out so far (although not yet fully completed in the north). Second, the targets were selected on the basis of FUV brightness, so they were expected to be relatively fast rotators, which again is advantageous for TESS.

There were three full sky surveys (TESS Years 1–3) included in the analysis: two in the southern Ecliptic hemisphere (sectors 1–13, 27–39), and one in the north (sectors 14–26). Current Year 4 (2021 July–2022 September) includes a partial northern survey, and new coverage of a band along the Ecliptic (missed in Years 1–3, intentionally, owing to the design of the TESS camera system). The second northern survey will be completed in Year 5 (2022–2023), and third southern survey will be started then as well.

TESS short cadence (2-minute sampling) light curves of the EclipSS subsample were obtained from MAST. Out-of-range values and extreme outliers were removed from the light curves; the time series were divided by the median; and then concatenated (all the targets were observed for six, or more, sectors). A piecewise cubic Hermite interpolating polynomial was used to bridge any short gaps in the time series.

The period analysis followed that outlined in Buzasi (2018). Three different techniques were applied: the Discrete Fourier Transform (DFT), the autocorrelation function (ACF), and the Morlet wavelet transform (with $k = 6$). The adopted DFT period simply corresponds to the maximum of the

resulting amplitude spectrum, while the ACF period is the highest peak in the autocorrelation after boxcar smoothing with a width of 900 minutes (0.6 d). The summed wavelet transform can at times have substantial signal at periods much longer than the rotation period, so the period search was confined to the range 0–2 $P_{\rm DFT}$, based on the DFT result. Uncertainties in the DFT periods were estimated by calculating the noise in the vicinity of the peak frequency, and then estimating the "jitter" in the position of the peak that would result from random 1 σ changes in the underlying local Fourier spectrum. A parallel approach was adopted for the other methods. The three different period-finding techniques have different strengths and weaknesses, but in combination they can provide a unified view of the photometric behavior of a target. Results of the three tools are listed in Table 8, and illustrative examples are provided in Figures 11a–11e.

Table 8. TESS Rotation Periods for EclipSS Subsample

HD	TIC	N(Sectors)	DFT	Autocorr	Wavelet	Consensus
1	2	3	4	5	6	7
24636	238196350	8, 7	0.86±0.01	0.78±0.04	0.82±0.03	0.82±0.03 (0.03)
38459	235066737	3, 3	10.0±0.3	10.4±0.4	10.2±0.6	10.2±0.2 (0.4)
39755	149631289	11, 10	1.14±0.03	1.18±0.02	1.15±0.05	1.16±0.02 (0.04)
41004[a]	219152539	3, 3	1.33±0.01	1.25±0.08	1.32±0.05	1.30±0.04 (0.05)
62850	340459410	6, 7	3.66±0.09	3.68±0.04	3.69±0.11	3.68±0.01 (0.09)
150706	159511543	7, –	10.2±0.1	9.8±0.1	10.1±0.3	10.0±0.2 (0.2)
156559	198407592	12, –	0.62±0.04	(0.60±0.29)	0.62±0.02	0.62±0.00 (0.03)
172669	229738635	11, –	9.5±0.1	9.8±0.1	9.3±0.3	9.5±0.2 (0.2)
180712	243278327	13, –	6.6±0.1	5.7±0.1	6.7±0.3	6.3±0.5 (0.2)
185239	275626011	6, –	2.3±0.2	(2.1±1.0)	2.4±0.4	2.3±0.1 (0.3)

NOTE—Col. 2 is the number of TESS sectors included in the analysis. Two complete sky surveys were available for the southern Ecliptic hemisphere, and one for the north. Double entries show the number of sectors in each survey. Cols. 4–7 periods in days. Col. 4 is the result from a Discrete Fourier Transform. Col. 5 refers to an autocorrelation function analysis. Col. 6 is a wavelet decomposition. Col. 7 is the consensus period, ignoring any of the Col. 4–6 values with large uncertainties (highlighted by parentheses). The first uncertainty listed for the consensus period is the standard deviation of the up to three individual periods. The second uncertainty listed, in parentheses, is the average uncertainty of the various techniques. The adopted uncertainty is the larger of the two.

[a]Short P from dM secondary? longer $P \sim 9$ d for K-type primary?

Figure 11. Results of modeling TESS light curves of representative members of the EclipSS subsample. The image in the upper panel schematically depicts the wavelet analysis. The second panel down is the TESS light curve normalized to its mean value. The "Time" axis for these two panels is JD–2457000. The third panel down is the wavelet period-amplitude distribution. The lowest panel is the DFT analysis. (a) HD 39755; (b) HD 41004; (c) HD 62850; (d) HD 150706; (e) HD 180712.

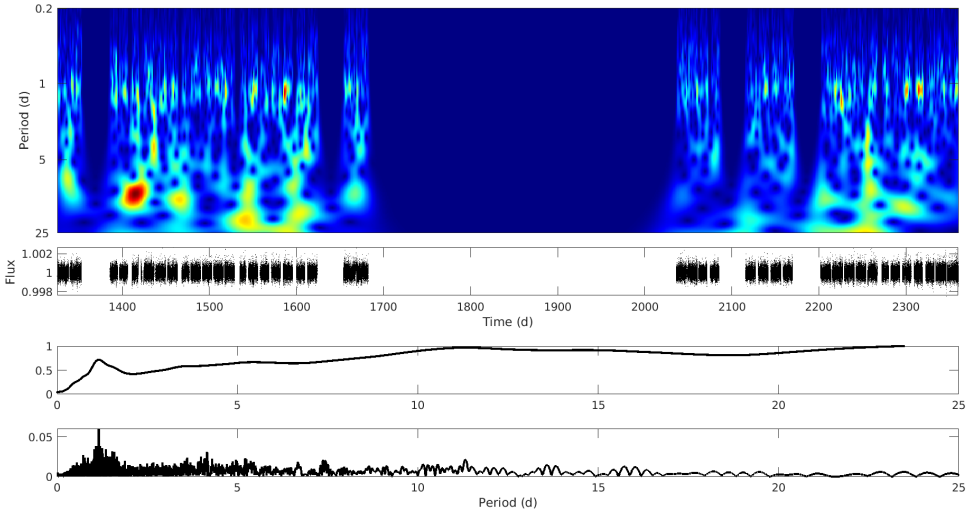

Figure 11a.

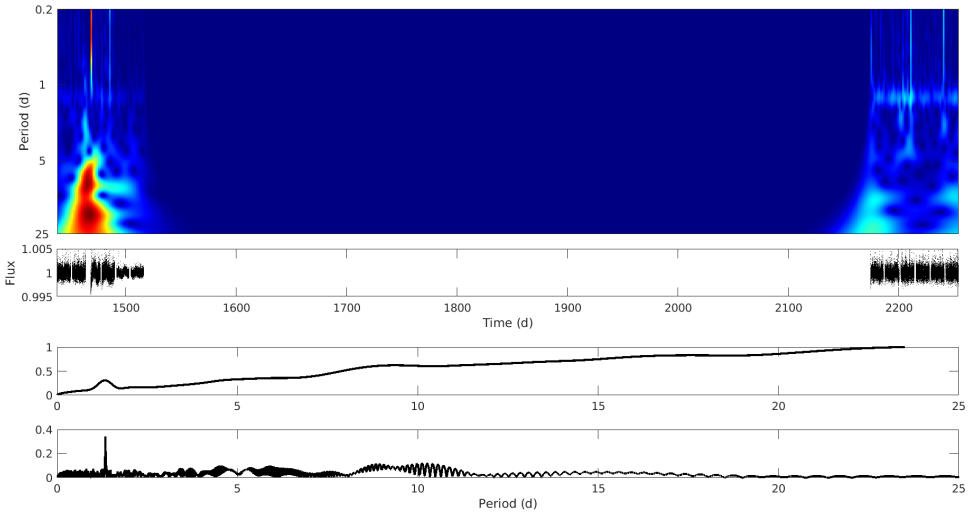

Figure 11b.

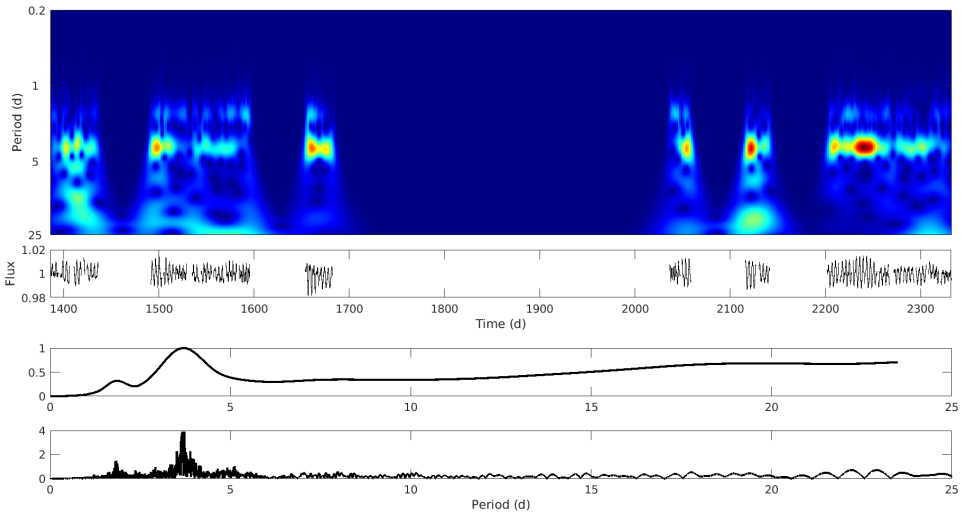

Figure 11c.

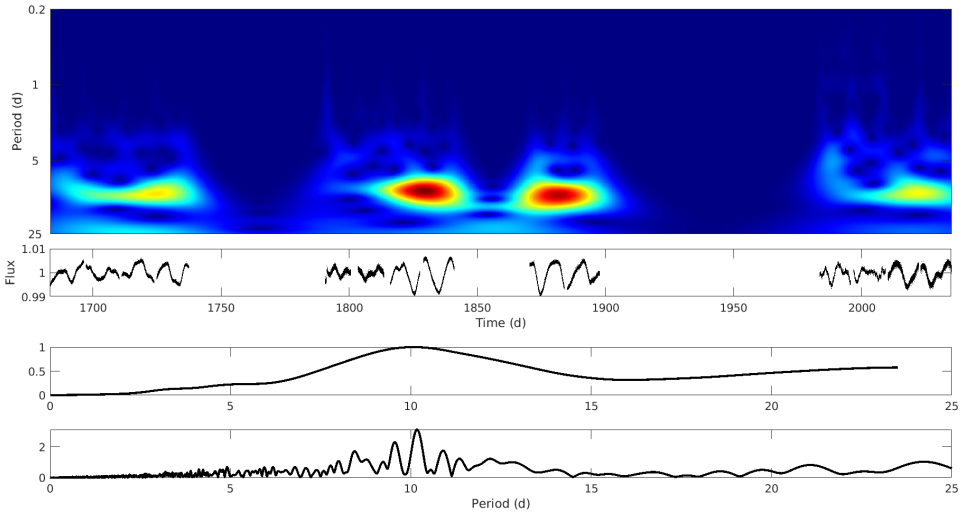

Figure 11d.

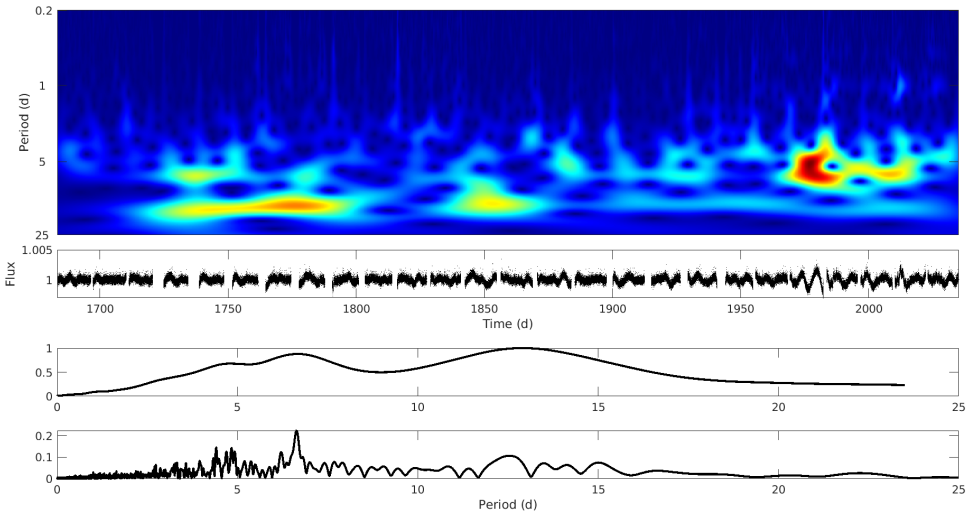

Figure 11e.

Figure 11a is for HD 39755, a fast-rotating early-F dwarf. Many TESS sectors were collected for this high Ecliptic latitude star. The rapidly varying TESS light curve is evident. The full amplitude of the variation is only about 0.2 %. The wavelet image displays a clear band of power at about 1.2 d, which is seen as a peak at the extreme left of the period-amplitude diagram, and a narrow cluster of peaks in the DFT spectrum in the lower panel. A broader peak in the period-amplitude panel near 12 d likely is an alias contributed by the numerous TESS telemetry gaps.

Figure 11b is for the early-K dwarf HD 41004. Six TESS sectors are shown, split into two groups of three (for the two southern surveys completed to date). The full amplitude of the light curve again is about 0.5 %, but there are numerous positive spikes caused by strong flares (more evident in the wavelet image). A faint band of power is seen near 1.3 d in the wavelet map, especially in the second set of three sectors, which appears as a distinct peak in the middle panel, and a sharp feature in the bottom DFT power spectrum. There is a suggestion of a longer period of ∼9 d, as well, although not as obvious. More on HD 41004 shortly.

Figure 11c is for the early-G star HD 62850. Like HD 39755, many sectors were collected, numbering several hundred days of photometric coverage. However, unlike HD 39755, now the photometric amplitude is much larger, 2–3 %. There is a strong band of power at 3.7 d in the wavelet map, which appears as distinct peaks in the period-amplitude diagram and the DFT. Harmonics near 1.9 d are visible as well.

Figure 11d is for another early-G dwarf, HD 150706. Again, multiple sectors are available. There is a clear, strong signal at 10 d in all the panels, with perhaps a weak harmonic in the period-amplitude diagram. The full range of the modulation is similar, although smaller than that of HD 62850, 1–2 %. As will be seen later, the apparent TESS period of this star is about twice as long as expected from its elevated X-ray luminosity, relative to the other G dwarfs. However, there is no clear evidence of a shorter period in the TESS photometry, and it would be very unusual to have a sustained interval during which twice the true period dominated the modulated signal.

Figure 11e is for the late-F dwarf HD 180712. This target had near-continuous coverage during the first northern Ecliptic hemisphere survey by TESS. The maximum photometric variation is around

0.5 %. The dominant signal in the DFT power spectrum is at 6.3 d, and harmonics of that period are evident. There are corresponding peaks in the wavelet period-amplitude diagram, but also a broad peak near 13 d, which likely is contributed by the numerous telemetry gaps. This photometric series is an example where the activity modulation was more obvious at certain times than at others. So, even though the apparent rotation period is short, there is a clear advantage to collecting a long-duration record covering many rotational cycles.

2.6.2. *The Curious Case of HD 41004*

Most of the TESS rotation periods were as expected for these FUV-bright targets, ranging from less than a day out to about 10 days; the three fastest rotators all are early-F types. HD 41004 is a notable exception to expectations, however. On the one hand, the K dwarf was the FUV-brightest of the ten member EclipSS subsample, so a relatively fast rotation period was expected, on the order of 5–10 d, based on other stars of similar color and youth. (HD 41004 has an $L_{\rm BOL}$ that places it above the ZAMS, ostensibly on a pre-MS Hayashi track: see Fig. 1; and is listed in the SACY catalog of young active stars: Torres et al. 2006). Indeed, the wavelet decomposition shows the presence of a period of about 9 d, although for only part of the bifurcated time series. On the other hand, the dominant period from the multi-tool analysis is an unexpectedly short 1.3 d. The measured $v \sin i$ of the K dwarf is only 1.0–1.2 km s^{-1} (Santos et al. 2002; Torres et al. 2006), which could be compatible with a rotational velocity of about 5 km s^{-1} (i.e., from the longer 9-d period) if the inclination of the star is low, less than about 15°; but much more difficult to accept if the true rotation rate of the K dwarf is the 36 km s^{-1} suggested by the 1.3-d period.

However, HD 41004 is a binary system, with a faint dM2 companion, currently about 0.″2 from the K dwarf, in a several decade orbit. Curiously, a subtle 50 m s^{-1} periodicity, with *exactly the same* 1.3-d period, was identified in radial velocity time series of the K dwarf, obtained by Santos et al. (2002) as part of an exoplanet survey using the sensitive CORALIE spectrograph. The authors argued that the low-amplitude velocity variation, and systematically varying line bisectors in the blended CORALIE spectra (which did not resolve the two stars), originated from the red dwarf. They proposed a close-orbiting substellar body with the 1.3-d period and a mass of 19 $M_{\rm J}$, which would classify it as a brown dwarf (BD) (see also Zucker et al. 2003). If the dM star had been recorded in isolation, the radial velocity swings due to the BD would have been much larger, but were diluted in the blended spectrum by the static contribution of the ten times brighter K dwarf primary.

Now, the same short period is seen by TESS in the integrated light of the system. One possibility is that the ∼0.5 % peak-to-peak photometric signal represents variable reflection by the BD of the red dwarf's light, although this would require a somewhat extreme set of system properties. Another possibility, favored here, is that the red dwarf has become tidally synchronized to the tightly orbiting BD, and thus the dM rotation period would also be the short 1.3-d, and TESS is simply witnessing modulations of surface activity on the fast-spinning secondary. Normally, a more modestly rotating red dwarf would be out-shined by an early K dwarf of the same age at high energies, but in this case the fast rotation of the dM star is externally imposed and not age-related, so the red dwarf could dominate the X-rays and FUV. (Pineda et al. 2021 have described a number of hyperactive fast-rotating dM stars. One of their exceptionally FUV-bright sources, LP 247-13, is a dM3 with the same short period of about 1.3 d.) Further, the TESS light curve of HD 41004 is punctuated by frequent white-light flares, which would be another hallmark of a hyperactive red dwarf, but unusual

for a moderately active K dwarf. However, a third possibility, originally dismissed by Santos et al. (2002), is that the low-amplitude radial velocity signal actually is from the K star, specifically a sub-Jovian-mass planet in the 1.3-d orbit, but seen at low inclination (Zucker et al. 2004, identified a longer-period 2.5 M_J planet around the primary, with a 2.6-y period). In that case, the TESS signal would be associated with reflected light from the K-star's inner planet, and the high activity levels of the whole system might be contributed by the K dwarf (with a fast rotation rate obscured by a small $\sin i$ factor); although an active dM secondary would also be a possibility (if the albeit transient 9-d signal in the TESS light curve was not related to the K dwarf rotation, and the true period of the primary was much longer).

Unfortunately, there is scant evidence to decide whether the secondary, or the primary, is dominant at high energies. The COS FUV XDL camera is not ideal for separating two objects only 0.″2 apart, and the 1″ resolution of Chandra HRC-I image is not suited for the purpose either. The enhanced rotational broadening—20 km s^{-1} for a small red dwarf with the 1.3-d period—is not enough to be clearly distinguished in the relatively low-resolution COS FUV spectra. The main spectral oddity supporting the active secondary hypothesis is that the Ca II HK emission of HD 41004 is not exceptionally bright, only falling between those of α Cen B and ϵ Eri on the S-index scale (Henry et al. 1996), pointing to a rotational period of perhaps 20–30 d (see, also, Santos et al. 2002). In fact, the latter authors reported a lack of lithium absorption in the red spectrum of HD 41004, which casts doubt on the earlier attributions that it is a young object (although the H–R diagram position of the K dwarf would still remain anomalous).

There is one more piece to this story. As outlined by Ayres & Buzasi (2021), an intriguing implication for the scenario of the spun-up secondary is that the red dwarf should be losing angular momentum through magnetic braking by its coronal wind, which would also be at the expense of the dM/BD orbit thanks to the strong tidal coupling. Over time, the pair should evolve into contact, and eventually coalesce, leaving behind a slightly more massive, but ultra-fast spinning, single red dwarf; and in the process further depleting the already barren "brown-dwarf desert." Oetjens et al. (2020) have described the physical basis of this process, and provide extensive references to previous work in this area. Such tidal-cannibalism is much more effective for close-in BDs than planets, simply because of the amplified tidal-interaction parameter (see Scharf 2010).

Several pieces of evidence presented above point to the dM2 secondary of HD 41004 as the source of the elevated high-energy emissions of the system. Because that late spectral class is beyond the scope of the present study, reluctantly HD 41004 will be excluded from the subsequent discussions of emission-line properties and the rotation-activity connection. Clearly, however, this fascinating object is worthy of further scrutiny.

2.6.3. *Rotation Summary*

Table 9 provides a summary of rotation periods (and rotational velocities) of the Total EclipSS sample members. The majority of the periods for the Related objects and the Reference stars were taken from studies of rotational modulations of Ca II contributed by the Mt. Wilson HK Project (e.g., Noyes et al. 1984; Donahue et al. 1996; Baliunas et al. 1996). The HK modulation period is considered the gold standard here, for stars with periods greater than about 10 d and outside the Ecliptic polar regions, given the limitations of the TESS photometry described earlier. Appendix C is a more detailed description of the provenance of the rotation periods, as well as available rotational broadening measurements ($v \sin i$), which not only can validate a measured period, but also in some

cases provided the primary assessment of the stellar spin, in the absence of a secure photometric period.

Table 9. Total EclipSS Rotation Summary

HD Num	Name	$P_{\rm ROT}$ (d)	$R/R_\odot$	$v_{\rm ROT}$ (km s^{-1})	Notes
1	2	3	4	5	6
		EclipSS Subsample			
24636		0.82±0.03	1.39	86±3	broad FUV lines
38459		10.2±0.4	0.85	4.2±0.2	
39755		1.16±0.04	1.43	62±2	broad FUV lines
41004		1.30±0.05	0.93	36±1	$v_{\rm ROT} = 5.3\pm0.6$ for $P_{\rm ROT} = 9\pm1$
62850		3.7±0.1	1.06	14.5±0.4	
150706		10.0±0.2	0.97	4.9±0.1	
156559		0.62±0.03	1.43	116±6	very broad FUV lines
172669		9.5±0.2	0.98	5.2±0.1	
180712		6.3±0.5	0.99	7.9±0.6	
185239		2.3±0.3	1.35	30±4	
		Related Objects			
10700	τ Cet	34.5	0.92	1.3	
20630	κ Cet	9.1±0.1	0.97	5.4±0.1	
39587	χ^1 Ori	5.3±0.2	1.03	9.8±0.4	
72905	π^1 UMa	5.0±0.2	0.97	9.8±0.4	
129333	EK Dra	2.7±0.1	0.98	18.3±0.7	
		Reference Sample			
···	Sun	25.4±1.0	1.00	2.0±0.1	Sidereal
22049	ϵ Eri	11.5±0.3	0.81	3.6±0.1	
61421	Procyon	(19±2)	2.03	5.4±0.6	$P_{\rm ROT}$ from $v_{\rm ROT}$
128620	α Cen A	(26±3)	1.22	2.4±0.3	$P_{\rm ROT}$ from $v_{\rm ROT}$
128621	α Cen B	40±3	0.86	1.1±0.1	
131156A	ξ Boo A	6.2±0.1	0.84	6.8±0.1	

Table 9 *continued on next page*

Table 9 *(continued)*

HD Num	Name	$P_{\rm ROT}$ (d)	$R/R_\odot$	$v_{\rm ROT}$ (km s^{-1})	Notes
1	2	3	4	5	6
131156B	ξ Boo B	11.9±1.1	0.67	2.8±0.3	
165341A	70 Oph A	19.5±0.3	0.86	2.23±0.03	
165341B	70 Oph B	(34)	0.72	(1.1)	$P_{\rm ROT}$ from $R'_{\rm HK}$

NOTE—See Appendix C for further details concerning each star. Rotation rates were mostly derived from measured spin periods, except in two cases (α Cen A, Procyon) for which the periods were based on an estimated rotational velocity. The rotation period for 70 Oph B reported by Baliunas et al. (1996) was not directly measured, but rather was inferred from the HK flux, through an empirical Ca II rotation-activity connection.

3. ANALYSIS

3.1. *Behavior of the Pseudo-Gaussian Profiles Measured in the STIS Spectra*

Previous Table 6 presented profile shapes and Doppler shifts of representative FUV lines, focusing on the STIS medium-resolution spectra of the nine Total EclipSS stars for which suitable observations are available. The transitions mostly are modestly ionized species characteristic of hot plasma; but two sharp chromospheric features as well, which serve as zero-velocity references. Paper V had described the detailed dependence of the various profile parameters—Doppler shifts, widths, and pseudo-Gaussian exponents—of diverse-excitation species from STIS medium- and high-resolution spectra of Procyon and α Cen AB taken roughly semiannually over a decade (following the undulating magnetic cycles of α Cen AB, but the "flat-line" activity state of Procyon). Although these objects represent a fair range of stellar properties, especially surface temperature and gravity, the measured profile parameters, particularly the Doppler shifts and the sub-Gaussian nature of the high-temperature emission profiles, were surprisingly similar among the three stars. Table 6 shows that this also is the case over a wide range of *activity levels* among the STIS G dwarfs, again both in terms of the Doppler (red)shifts of, say, the Si IV and C IV doublets (see, e.g., Feldman et al. 1982 for the Sun), as well as the sub-Gaussian a exponents of these lines; even despite the large differences in $f_{\rm L}/f_{\rm BOL}$ going from relatively low-activity dwarfs like α Cen A, to an upper tier of activity represented by young χ^1 Ori and π^1 UMa, and even the more extreme case of Pleiades-age EK Dra.

Equally intriguing, as was hinted in Paper V, there is a general trend of decreasing high-temperature redshifts going from hotter Procyon, through the Sun-like G stars, to the two cooler early K stars. Procyon, because of its class–IV-V proto-subgiant status, perhaps should be discounted in that conversation, but the negative gradient between the G stars and their K-type cousins remains. The downdrafts of hot TZ plasma are thought to occur in cooling coronal magnetic loops (e.g., Pneuman & Kopp 1978). One could imagine that the higher gravities of the small K dwarfs might encourage larger velocities of this cooling gas, although, to be sure, the values among the Sun-like stars are only a small fraction of the gravitational free-fall speeds, so the settling process must be more involved

than a simple ballistic phenomenon. Despite the suggested trend with decreasing stellar temperature, it still is quite remarkable that the TZ redshifts empirically do not depend, at least not strongly, on the activity level of the star. That behavior might be viewed as less surprising if the fundamental building blocks of elevated FUV emissions—active regions—basically are similar among all the stars, but simply become more numerous among the highest intensity examples (see, also, Wood et al. 2018, for a similar perspective, albeit based on coronal emission-measure modeling; and Coffaro et al. 2020, for the specific case of ϵ Eri).

3.2. *Construction of an "XUV" Subcoronal/Coronal Radiation Proxy*

Two key aims of the present study are: (1) obtain refined correlations among the various emissions from the stellar corona and the subcoronal layers, expressed in terms of "flux–flux" diagrams, to help trace the interconnections among the different thermal regimes, and serve as targets for semi-empirical and ab-initio modeling; and (2) inventory the total radiative losses of these magnetically energized regions to correlate against stellar properties, specifically rotation, that might be closely related to the internal dynamo mechanism. The motivation for the latter objective was the previous work of Pevtsov et al. (2003), who showed that various spatially resolved magnetic features on the Sun—including quiet areas, ephemeral bright points, and active regions—displayed a tight power-law correlation, over many orders of magnitude, between the X-ray surface intensity from the Yohkoh Soft X-ray Telescope and the total unsigned magnetic flux in the same pixels, based on high-resolution Kitt Peak and SoHO MDI magnetograms.

For both objectives, it is convenient to define an "XUV flux," which is a combination of multiple species intended to represent the radiative cooling of the layers above about $5{\times}10^4$ K, which corresponds to the major part of the subcoronal/coronal magnetic *heating* (since cooling must balance heating), aside from the (likely small) fraction associated with kinetic fluxes in stellar outflows (which are difficult to measure even in the favorable situation of the Sun; see Wood 2018 for the equally challenging case of M dwarfs). As such, this XUV flux is an indirect proxy for the magnetic conditions on the stellar surface (cf., Pevtsov et al.), which potentially can be correlated with stellar parameters more directly connected to the internal dynamo mechanism from a theoretical viewpoint. The present section outlines how such an XUV flux can be assembled from various directly observed high-energy emissions, complemented by indirect estimates for the "unseen" pieces.

Some of the key $T \gtrsim 5{\times}10^4$ K emissions are already found in the FUV or accounted by the 0.1–2.4 keV X-rays. However, an important contribution arises from the EUV spectrum, through a diversity of ionization states of iron (and nickel) in the 125–250 Å region, as well as the bright emissions He II 303 Å and C III 977 Å, and others, longward of 250 Å. Unfortunately, the EUV spectra of even nearby stars are largely blocked by interstellar atomic hydrogen absorption for 300 Å$<\lambda<$ 912 Å, or are difficult to observe with current instrumentation (912–1150 Å), so any guidance concerning how those emissions might scale with increasing activity must mainly come from the Sun (e.g., Paper II). The approach for the 250–1150 Å interval was to identify the important line emissions and associate them with similar-excitation features in the more accessible FUV. For example, EUV C III 977 Å pairs with FUV C III 1175 Å, or EUV He II 303 Å pairs with the FUV C IV 1550 Å doublet. Normally, one might consider FUV He II 1640 Å to be a better proxy for 303 Å. However, 1640 Å is an excited transition which could form differently than the resonance line. Further, in low-activity Sun-like stars, the 1640 Å emission is blended with an Fe II line of similar strength,

which can affect the accuracy of the flux measurement. The specific EUV→FUV associations were guided by formation temperatures and the flux–flux correlations of Paper II.

The region 125–250 Å is more challenging because the breadth of ionization stages present means that there is not a single FUV proxy, or even a combination, that can serve to scale the emissions of that interval over the wide range of activity levels of the Total EclipSS sample, whose emission-measure distributions span a factor of a hundred in coronal temperatures, $\sim$ 0.5–50 MK (Fig. 2). The 0.1–2.4 keV coronal soft X-ray normalized flux, f_X/f_{BOL}, is the best choice, because it too contains a wide range of ionization species, including the numerous emissions in the iron "M-shell" region between 60–100 Å (see Ayres 2014; Wood et al. 2018). In fact, the ratio of the 0.05–0.1 keV (125–250 Å) flux to that in the 0.1–2.4 keV (5.2–125 Å) reference band can be rather large at low plasma temperatures, but then decreases rapidly with increasing temperature, as the bulk of the emission shifts back into the 0.1–2.4 keV window, owing to the preponderance of the H-like and He-like ionization states of abundant metals such as O, Ne, Si, and Mg, as well as the $\sim$1 keV L-shell emissions of Fe. Similarly, as the median temperature of the coronal EMD increases, emissions at energies higher than 2.4 keV come into play. Thus, while the ratio of the $E > 2.4$ keV flux to that in the 0.1–2.4 keV (5.2–125 Å) reference band is negligible at the lower EMD temperatures, it begins to be appreciable at the higher temperatures, $\log T \gtrsim 6.8$ K. The full X-ray band, 0.05–12 keV, contains by far the bulk of the high energy radiative losses of even extreme stellar coronae, so is a key part of the overall coronal cooling budget.

The ratio of the full-to-reference band fluxes can be estimated using the EMD convolution strategy described previously; taking the standard APEC plasma emission model for solar abundances, and, of course, negligible interstellar absorption (since ratios at the source are desired). The corresponding test function was illustrated previously, in Fig. 3.

Figure 12 illustrates the EMD-convolved results for the full-to-reference band ratio, as a function of the X-ray surface flux, $\log F_X$, which is the main observable associated with the EMD models. Blue diamonds are the outcome of the EMD calculation, and the underlying smooth curve is an empirical fit of the form:

$$r_X \equiv \frac{f_{(0.05-12)}}{f_{(0.1-2.4)}} = 2.322 - 1.199\,(\log F_X - 5) + 0.318\,(\log F_X - 5)^2 \ . \qquad (2)$$

The larger circles on top of the smooth curve are the result of applying the conversion formula to the measured $f_{(0.1-2.4)}/f_{BOL}$ values of the Total EclipSS stars as transformed to surface fluxes via $F_X = \sigma\, T_{eff}^4\, (f_X/f_{BOL})$. The color-coding of the symbols is according to spectral type as in Fig. 1. At the higher surface fluxes, $\log F_X \geq 6$, most of the total $E \geq 0.05$ keV emission is accounted by the reference 0.1–2.4 keV X-ray flux, but at lower surface fluxes, the ratio rises rapidly to factors of 4–5 for the lowest activity members of the sample (τ Cet, α Cen A, and the Sun). Consequently—at least to the extent that the plasma emission model is reliable—the bulk of the high-energy emission of low-activity dwarfs occurs at the longer wavelengths, in the 125–250 Å EUV region, beyond the low-energy limit of the reference 0.1–2.4 keV band.

Small open dots in the figure refer to solar $f_{(0.05-12)}/f_{(0.1-2.4)}$ ratios over the period 2000–2020 derived by integrating the respective bandpass fluxes from the FISM2 high-energy irradiance catalog mentioned earlier. The fluxes were averaged into 81-d bins (3 rotations) prior to constructing the ratios. The empirical solar values track the theoretical curve reasonably well, demonstrating the hardening of the solar X-ray spectrum over the course of the magnetic cycle. However, the absolute

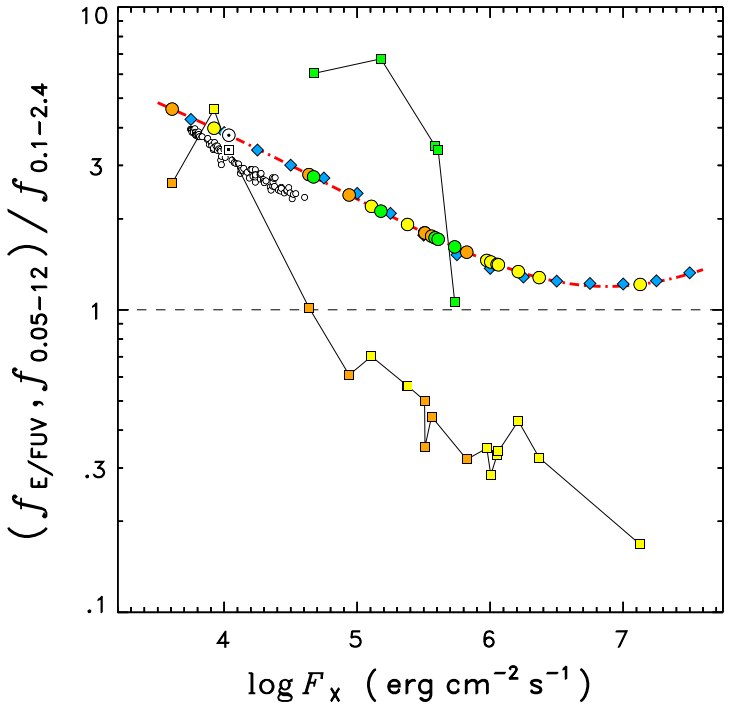

Figure 12. Blue diamonds illustrate the variation of the X-ray flux ratio ("flux multiplier"), $r_X \equiv f_{(0.05-12)}/f_{(0.1-2.4)}$, as a function of the X-ray surface flux, $\log F_X$, calculated from a theoretical temperature-dependent relation folded through the various EMD models (which are designated according to the associated $\log F_X$). The smooth, red dotted-dashed curve is a parabolic fit to the discrete values. Filled circles refer to the various members of the Total EclipSS sample, for which the X-ray flux multiplier was calculated from the smooth fit. The chain of small open circles depict empirical values of the solar r_X over Cycle 24 determined by direct integrations of high-energy irradiance records, averaged into 81-day (3 rotations) bins. Connected filled boxes refer to the stellar (and solar) ratios of the $\lambda > 250$ Å "E/FUV" flux contribution relative to the reference 0.1–2.4 keV X-ray intensity. The F stars and the G/K dwarfs are separately connected by solid lines owing to their apparently divergent behavior.

solar ratios are systematically about 20 % lower than the theoretical curve over the range of surface fluxes traced by the magnetically changing Sun over recent Cycles 23 and 24. This difference is small compared with uncertainties in the EUV flux calibration and the likely accuracy of the underlying plasma emission models[13]. Most important, the solar values appear to support the relative behavior of the theoretical curve through the key region of soft coronal sources where the (0.05–12 keV) / (0.1–2.4 keV) flux ratio is most elevated.

The preceding discussion focused on the high-energy part of the subcoronal/coronal radiative losses, based on scaling the reference 0.1–2.4 keV X-ray flux. In a similar fashion, one can devise flux multipliers for the "hidden" discrete emissions of the 250–1150 Å EUV spectrum. As mentioned before, the most important are the resonance lines He II 303 Å and C III 977 Å. But, there are a number of weaker emissions that in combination can make a noticeable contribution to the total, such

[13] The "theoretical" points (blue diamonds) in the figure were based on APEC emissivities as calculated through the WebPIMMS tool and integrated with the Wood EMDs, whereas the FISM2 spectral fluxes were based on CHIANTI (https://www.chiantidatabase.org/chianti_database_history.html) emissivities and solar-specific emission-measure models, but empirically adjusted to high-energy irradiances from a variety of solar sensors.

as O V 629 Å and the O VI doublet near 1035 Å. As shown in Paper II, the He II, O V, and O VI emissions scale with increasing activity approximately like FUV C IV. The C IV flux multiplier, about two-thirds of which is contributed by He II, is 5.7 (including the 1.0 from C IV itself). Similarly, EUV C III 977 Å scales well with the FUV C III 1175 Å multiplet, again accounting for about two-thirds of the total flux multiplier of 3.4, with respect to 1175 Å. In the mid-EUV there also are prominent transitions of Mg IX 368 Å and a doublet of Mg X at 609 Å and 624 Å, both of which form near 10^6 K in CIE, and together are about 10 % the strength of the 0.1–2.4 keV X-ray flux at the high point of solar Cycle 24. However, the contribution of these relatively cool coronal lines would be swamped by the elevated r_X factor at 1 MK, and would be severely diminished in importance at 10 MK owing to the unfavorable ionization balance, so were ignored in the X-ray flux multiplier.

The final formulation of the combined XUV proxy is as follows:

$$\mathrm{XUV} \sim r_X\, \mathrm{X}_{(0.1-2.4)} + 3.4\ \mathrm{C1175} + \mathrm{Si1206} + \mathrm{N1240} + \mathrm{Si1400} + 5.7\ \mathrm{C1550} + \mathrm{He1640}\ , \qquad (3)$$

where the abbreviated parameters are shorthand for f_L/f_{BOL} of the indicated species, and "$\mathrm{X}_{(0.1-2.4)}$" refers to the 0.1–2.4 keV X-ray band. Here, the separate measurements of the doublet components of Si IV, C IV, and N V were combined into a single flux for that species, e.g., "Si1400" is the sum of Si IV 1393 Å and 1402 Å. The contribution of the non-X-ray part ("E/FUV") of the total flux for the individual Total EclipSS stars is illustrated in Fig. 12 by the two sets of connected filled squares, again color-coded by spectral type. The F stars were treated separately from the G/K dwarfs, because their behavior clearly is different, showing significantly elevated E/FUV emissions relative to the G/K dwarfs at the same $\log F_X$. Among the G/K dwarfs, the lowest activity members have E/FUV ratios similar to the X-ray-related part of the total, and several times higher than the 0.1–2.4 keV flux on its own. However, the E/FUV contribution falls rapidly with increasing X-ray surface flux, so that by $\log F_X \sim 5$, it has dipped well below the X-ray-related part. The F stars, on the other hand, mostly have E/FUV ratios that eclipse the X-ray contribution, owing to the over-active 10^5 K layers of these thinly convective objects.

The savvy reader will notice that the formulation of the XUV flux proxy has explicitly ignored the various strong chromospheric ($T \lesssim 10^4$ K) emissions, such as H I 1215 Å Lyα in the FUV; the Mg II 2800 Å hk doublet and several multiplets of Fe II in the NUV; and famous Ca II HK 3950 Å in the violet-optical. Mg II normally is the dominant cooling flux of the group in late-type stars (see Linsky & Ayres 1978; also, Paper I). Normally, as well, the chromospheric emission of a star would be much larger than the XUV proxy flux, especially among the low-activity dwarfs like the Sun. As known from studies of the Sun, the Mg II emission arises partly in the wide-spread magnetic supergranulation pattern, which is populated mainly by a "local dynamo" unrelated to the cycling dynamo (see Paper V); partly in magnetic active-region plage; and partly in the supergranulation cell interiors by hydrodynamical shocks, probably mostly unrelated to magnetic effects (e.g., Carlsson & Stein 1992, and references therein, for the Ca II analog). As one considers progressively higher temperature species, the formation becomes more localized in the magnetic active regions, which undeniably are creatures of the internal dynamo.

Consequently, considering just the high-temperature species to construct the XUV proxy flux has a better chance to isolate the magnetic phenomena (large-scale active regions) most closely connected to the internal dynamo, and avoids the distractions presented by the chromospheric emissions, perhaps more closely tied to hydrodynamical heating and the supergranulation pattern, where the magnetic

elements can partly arise from local-dynamo field production (independent of the internal dynamo, and more closely connected to direct, though inefficient, conversion of convective energy to magnetic flux). Further, the in-situ chromospheric heating itself might involve the magnetic field indirectly, merely to channel hydromagnetic waves into the outer atmosphere, rather than representing the conversion of magnetic free energy to heat via reconnections, as must operate more widely in the coronal active regions.

Another symptom that the heating mechanisms for the chromosphere and subcorona/corona behave differently is that the X-ray normalized flux rises as a steep power law (with index ~ 3) relative to the normalized Mg II flux, either over the solar magnetic cycle, or those of α Cen AB (see, e.g., Paper I). The higher contrast of the X-rays, and related XUV proxy (as shown shortly), with increasing activity also argues that the XUV composite flux is a more sensitive gauge than a pure chromospheric tracer, to follow changes in the surface magnetic conditions. Finally, the tension between the local and global dynamos affects only the lowest activity dwarfs, because already the solar case displays both extremes from cycle MIN (no active regions) to MAX (significant active-region coverage). At higher activity levels, even for modestly active α Cen B, the global-dynamo generated active region fields appear to dominate the high-energy emissions at all phases of the cycle. In particular, the coronal emissions of α Cen B at its activity MIN are similar to those of the Sun at its MAX, whereas in principle the cooler star should experience a much lower MIN, if it were completely spot-free, simply because the local dynamo magnetic flux creation should be significantly reduced because the available kinetic energy density in its photosphere is much less.

Recently, Johnstone et al. (2021) have also devised an "XUV" flux to account for all the radiation emitted by a late-type star that specifically might impact orbiting exoplanets. Their upper wavelength cutoff was 920 Å (Lyman continuum edge), which misses several of the diagnostically important hot FUV emissions between 920–1700 Å. However, they did include Lyα, brightest of the FUV lines, which is highly relevant to the photoionization of planetary atmospheres. They also obtained scaling laws for EUV radiation versus X-rays based on scattered observations of nearby stars by the EUVE satellite, for which the interstellar absorption could be estimated, at least for the wavelengths below about 300 Å. Here the XUV flux is defined differently, to exclusively include the high-temperature emissions, in an effort to isolate the parts of the coronal energy budget that might be most closely connected to active regions and from there to the internal dynamo. Further, here the EUV radiation in the 125–250 Å band was estimated from emission-measure models, which avoids the uncertainty of the empirical measurements due to ISM absorption, but accrues whatever systematics are associated with the modeling itself. Finally, here the important EUV emissions longward of 250 Å, especially He II 303 Å and C III 977 Å, were scaled according to FUV counterparts, using solar correlations that were specially corrected for instrumental effects (see Papers I and II). These alternative approaches, with regard to the XUV flux, have different immediate objectives (exoplanets versus the dynamo), but ultimately are complementary.

3.3. *Flux–Flux Diagrams*

The next comparisons of the present study are a series of flux–flux diagrams, illustrating the dependence of the normalized intensities of one species against those of another, for example coronal X-rays versus chromospheric O I. These comparisons are based on the total profile-integrated fluxes of the stellar emission lines, rather than the detailed line-shapes, so the corresponding low spectral

resolution, but full-disk, solar irradiances from Paper I can be incorporated (over the period 2009.0–2020.0, corresponding to recent sunspot Cycle 24).

Figures 13a–13e display several sets of flux–flux diagrams for the EclipSS subsample (omitting HD 41004 for the reasons mentioned earlier) and the Related objects (both depicted by larger dots); the epoch-resolved STIS stars (α Cen A: small yellow dots; B: orange; Procyon: green); the epoch-resolved Sun (81-day averages: small open circles); ξ Boo AB (squares); 70 Oph AB (diamonds); and ϵ Eri (single triangle). The spectral-type color coding of the symbols is same as in Fig. 1. Error bars for the Cycles binaries and ϵ Eri indicate $1\,\sigma$ standard deviations of epoch averages, to highlight temporal variability (at least over the limited epochs so far observed; more for the X-rays than the less-volatile FUV). The separate measurements of doublet components, e.g., Si IV 1393 Å and 1402 Å, have been combined into a single flux, in this case "Si IV 1400 Å." The fan of dashed lines, moored in the α Cen A cluster of points, depicts simple power laws. The slopes are: 0.5 (lower, red), 1 (2nd from bottom, thicker), 2 (next higher), and 3 (highest). Square brackets are shorthand for $\log f_{\rm L}/f_{\rm BOL}$ for the indicated transitions.

Figure 13. Flux–flux diagrams for the Total EclipSS stars. See text for symbol coding. The fan of dashed lines emanating from the α Cen A points depicts simple power laws with slopes of 0.5, 1, 2, and 3. Square brackets are shorthand for $\log f_{\rm L}/f_{\rm BOL}$ for the indicated transitions. (a) Various species versus chromospheric O I 1306 Å. (b) Various species versus upper chromosphere C II 1335 Å. (c) High-temperature species versus low-TZ Si III 1206 Å. (d) High-temperature species versus mid-TZ C IV 1550 Å. (e) Mixed-temperature species versus the hybrid XUV flux.

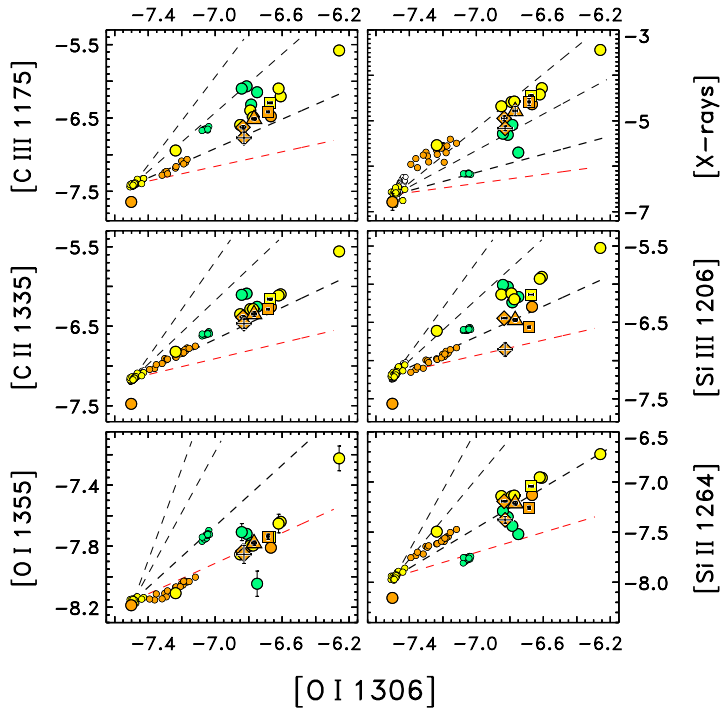

Figure 13a.

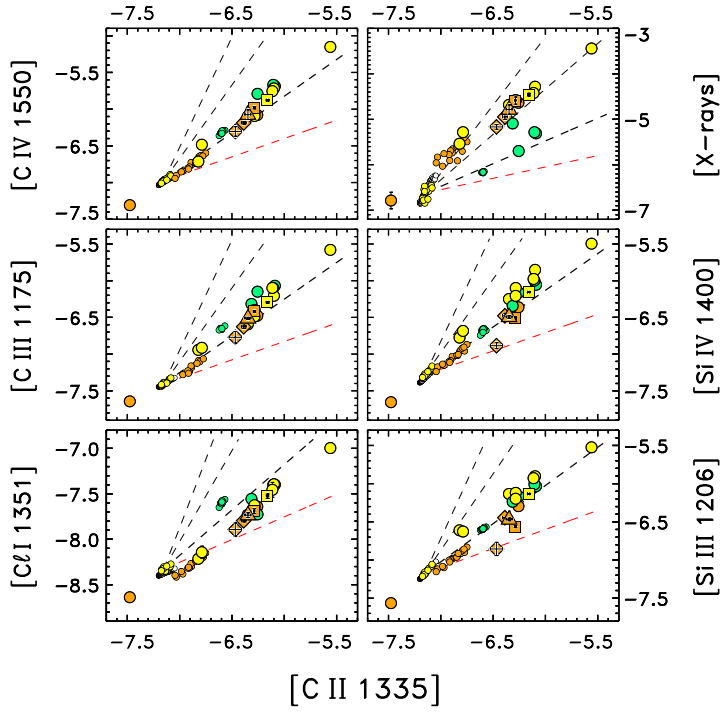

Figure 13b.

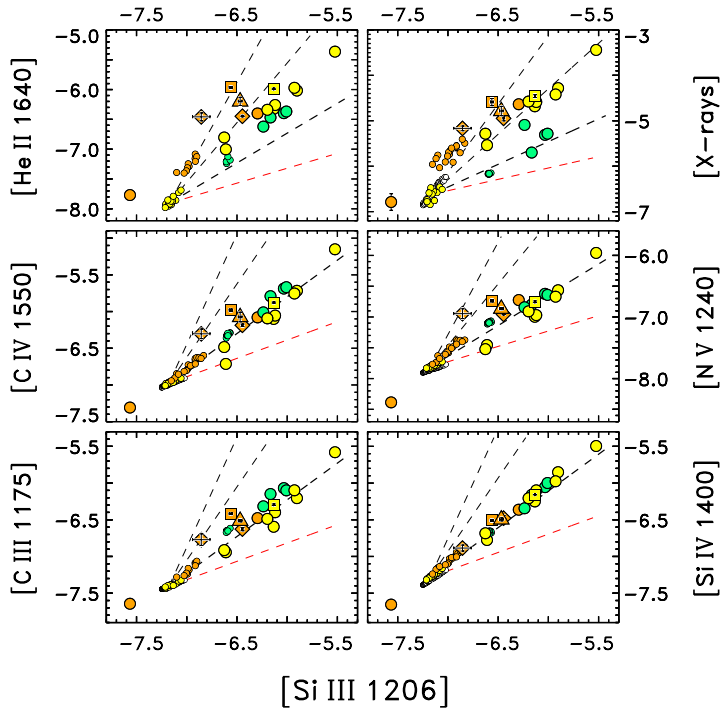

Figure 13c.

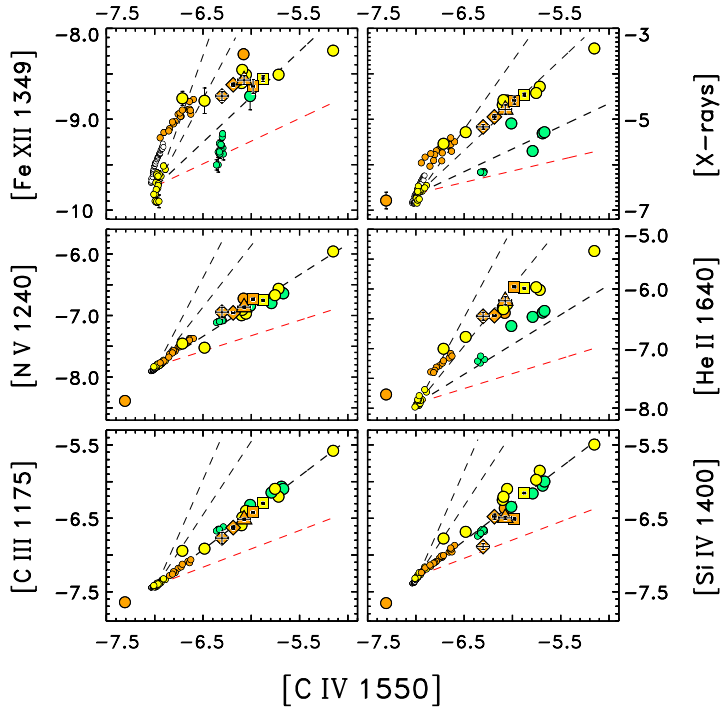

Figure 13d.

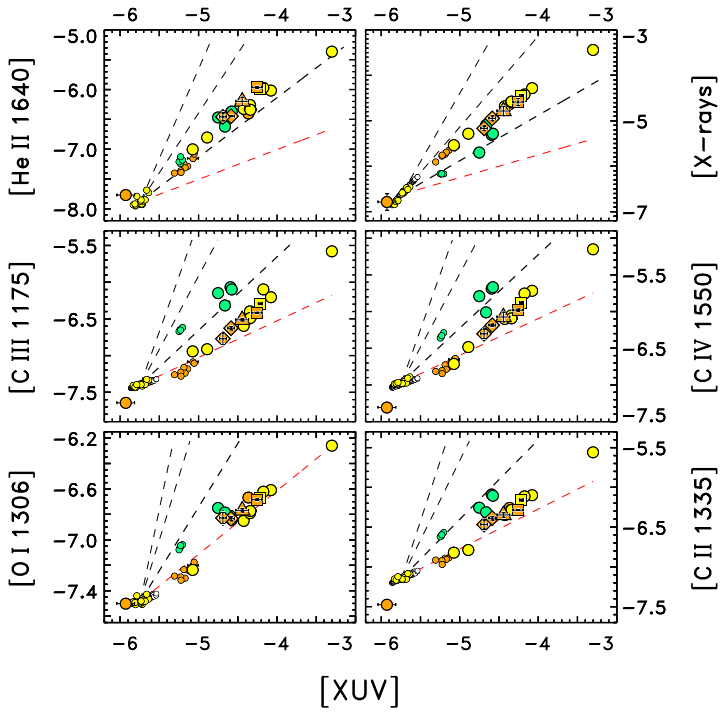

Figure 13e.

Figure 13a is for mixed-temperature species versus mid-chromosphere O I 1306 Å ($T \sim 8000$ K), the oxygen triplet component least affected by interstellar absorption (or geocoronal emission for COS). The lower left panel depicts O I 1355 Å versus 1306 Å. There generally is a good correlation between the two oxygen lines, aside from the conspicuous bump-up of F subgiant Procyon, although weaker 1355 Å increases only as the square root of the optically thick chromospheric 1306 Å flux, which raises the possibility of a different mode of formation (as discussed in Paper V). Chromospheric Si II 1264 Å also displays a good correlation with 1306 Å, but now Procyon and two of the other F stars show a negative dip relative to the main trend, as does τ Cet (orange dot to lower left). The downward displacement of τ Cet probably is associated with its lower metallicity (Si deficient compared with O). The apparent downward shift of the F stars perhaps is related to the effect noted in Paper V, whereby Procyon's O I 1306 Å emission was anomalously high compared to the main chromospheric diagnostic Mg II 2800 Å, at least with respect to the Sun and α Cen AB. Here, the O I emissions of Procyon and the other F stars conceivably are shifted to the right, so that at the same Si II intensity, the O I emission is enhanced. The Si II emission might be expected to track that of similar Mg II better than the O I resonance transition, because the ionization balance of the latter is complicated by charge exchange with atomic hydrogen, and there could be additional offsets if low-FIP (First Ionization Potential) Si and Mg experienced a FIP-effect abundance enhancement (Laming et al. 1995; Wood et al. 2018) in the chromosphere relative to high-FIP CNO.

The panel for C II 1335 Å shows a close power-law correlation with O I, with an index slightly larger than unity. The downward displacement of τ Cet is similar to that seen in the original EclipSS study for the several metal-poor stars, and was explained in Paper III as a consequence of the structuring of the upper chromosphere by Lyα cooling (versus the lower chromosphere where Mg II, Ca II, and Fe II control the structure). Although the F stars appear to fit better in the C II relation,

there is the caveat of the possible anomalous rightward shift of O I suggested in the Si II panel. The Si III 1206 Å comparison shows significant scatter around the mean trend, perhaps related to differences in FIP-effect abundance enhancements among the different temperature dwarfs. C III displays a good correlation with O I, now steeper than 1:1, but again with the caveat that the F stars might be anomalously shifted to the right, which, if corrected, would then show a significant relative C III enhancement compared to the cooler dwarfs (as noted for Procyon in Paper V). Similarly, in the X-ray panel, the overall smooth steep correlation would be noticeably improved if the apparent downward shift of the F stars were in fact a rightward displacement, as noted earlier. F stars like Procyon tend to have a conspicuous deficiency of their coronal X-rays relative to subcoronal C IV, but Paper V showed, at least for the archetype Procyon, that the anomaly disappeared in an X-ray versus chromospheric Mg II diagram, suggesting that the F subgiant seems to have a surplus of the subcoronal emissions.

Figure 13b depicts mixed-temperature species versus high-chromosphere C II 1335 Å (1–2×10^4 K). In the two "carbon" panels (C III, C IV), where abundance effects should cancel, there generally are good correlations against C II across the whole range of stars and activity levels. The Cl I panel shows small displacements between the Sun, α Cen A, and Procyon and the general trend obeyed by the rest of the stars (which α Cen B seems to anchor at the low end). The chlorine line is special because it forms through a fluorescence process driven by C II 1335 Å (Shine 1983). However, the main empirical trend appears to be steeper than the expected 1:1. The two "silicon" panels (Si III, Si IV) display more scatter, possibly again because of FIP-related abundance effects. The X-ray comparison shows an apparent deficit for the F stars, which, like previous O I, probably is associated with their enhanced subcoronal emissions (the solar C II formation extends into the lower TZ, and in the F types likely at least partially benefits from whatever mechanism enhances those layers). The leftward shift of τ Cet can be explained by an abundance effect (via the Lyα structuring mentioned earlier).

Figure 13c shows high-temperature species versus low-TZ Si III 1206 Å (5×10^4 K). The Si IV (8×10^4 K) panel displays a close, slightly above 1:1, correlation between the adjacent ionization states of silicon, where relative abundance effects should cancel. The carbon, nitrogen, and helium panels, where relative abundance effects would be more important, especially of the FIP variety, exhibit more scatter, although the general trends are similar, close to 1:1; except for He II, which displays a somewhat steeper correlation. The He II Bα line is thought to be at least partially formed by a photoionization recombination process driven by coronal EUV radiation below about 230 Å (e.g., Zirin 1975; Wahlstrom & Carlsson 1994), which could account for the steeper than 1:1 correlation. The X-rays exhibit a more curved power-law relation, and again the F stars fall to the right.

Figure 13d is for high-temperature species versus mid-TZ C IV 1550 Å (1×10^5 K). The more abundance-free carbon-carbon and nitrogen-carbon comparisons show tight 1:1 correlations. The He II, Fe XII, and X-ray comparisons are similar to one another, displaying curved power laws that rise steeply, but then bend over to a shallower slope, closer to 1:1. There again is the systematic rightward displacement of the F stars with their enhanced subcoronal emissions.

Finally, Figure 13e displays various species versus the "XUV" diagnostic described earlier. As a reminder, this hybrid flux was cobbled together from the 0.1–2.4 keV coronal X-rays and various FUV lines, with flux multipliers to account for the "unseen" emissions at the wavelengths outside and in between (2.4–12 keV, 125–250 Å, 250–1150 Å), in an effort to devise a reliable proxy for the

radiative output of the layers above about 5×10^4 K. That regime encompasses the major part of the subcoronal/coronal cooling, aside from the (likely small) fraction associated with mechanical fluxes in stellar coronal outflows. In that regard, it should be pointed out that in the classical view, much of the subcoronal emission represents the dissipation of an electron conduction flux from the base of the corona, down the steep temperature gradient of the TZ. As an inclusive high-temperature radiative cooling flux, ideally the XUV is an indirect proxy for the magnetic conditions on the stellar surface (see Pevtsov et al. 2003), specifically the dynamo-inspired active regions, which potentially can be correlated with stellar parameters more directly connected to the global dynamo mechanism from a theoretical vantage point.

Fig. 13e reprises some of the aspects of the previous flux–flux diagrams, recalling that the XUV flux bridges the coronal X-rays and subcoronal E/FUV emissions. Low-temperature chromospheric O I shows a remarkably good correlation with the XUV proxy, although with a shallow power-law slope close to 0.5 . C II displays a slope somewhat above 0.5 for the cooler stars, and a separate even steeper track, near 1:1, for the F stars. This behavior is repeated in the C III and C IV panels, where there is the suggestion of an upward curving relationship. He II shows a fairly straight, coherent power law, slightly steeper than 1:1, with no obvious displacement of the F stars. The X-rays display a similarly coherent, slightly steeper, though perhaps mildly curved, relation, with a modest, perhaps sideways separation of the F dwarfs relative to the G/K stars. The initial rise of the 0.1–2.4 keV X-rays is less steep than if the earlier, now abandoned, 0.2–2 keV reference energy band had been used, because at low coronal temperatures, $\sim$ 1 MK, the 0.2–2 keV X-rays contribute a relatively small fraction, perhaps as little as 10 %, of the total "coronal" high-energy flux, which mostly comes from longer wavelengths (62–250 Å). But, that fraction rises rapidly with increasing coronal temperature, and reaches $\sim$50 % by 2.5 MK. The 1–2.5 MK range is similar to the spread of average coronal temperatures across the solar cycle, so the 0.2–2 keV X-ray band is especially sensitive to coronal temperature even if the total high-energy flux (the XUV proxy here) changes more modestly. The use of the more inclusive 0.1–2.4 keV energy band compensates for the temperature effect to a large extent, thereby flattening the initial rise of X-rays versus the XUV.

3.4. *Correlating the X-rays and XUV Proxy with Rotation*

The next series of comparisons are an attempt to tie together the disparate components of this study, by juxtaposing the high-energy X-rays and hybrid XUV fluxes to various incarnations of the stellar rotation. Figures 14 and 16 have left and right panels that display, respectively, the variation of normalized X-rays, and the XUV proxy flux, versus the stellar rotation, expressed in two different ways: either as the rotation period, $P_{\rm ROT}$ (Fig. 14), or the so-called Rossby number, *Ro* (Fig. 16), a parameter borrowed from theoretical descriptions of the global dynamo mechanism.

The Rossby number is a dimensionless ratio of the rotation period to a convective turnover time scale, $Ro \equiv P_{\rm ROT}/\tau_{\rm c}$, where here $\tau_{\rm c}$ is the turnover time (either a "global" value obtained by averaging the convective velocities across the entire convection zone, or a "local" turnover time based on averaging convective velocities over a more limited span of the convection zone, typically one pressure scale height above the bottom boundary: see Landin et al. 2010 for a detailed discussion.) The Rossby number was introduced to stellar chromospheric physics by Noyes et al. (1984) who discovered that a spectral-type dependent dispersion in a scatter diagram of Ca II HK fluxes versus rotation period

could significantly be tightened by using *Ro* in place of $P_{\rm ROT}$, because the convective turnover time depends on stellar temperature in a way that compensated for much of the empirical spread[14].

In the figures, the unadorned dots are for the EclipSS subsample plus the Related objects. The adorned dots are for the various Reference stars, according to the legend in the right-hand panel. Thick dashed curves are notional expectations for the rotation-activity connections of Sun-like stars, namely a steep rise of the X-rays with decreasing period, but then a slight bend at shorter periods toward the "saturation" regime (see Wright et al. 2011, and references therein); or a more linear power-law trend for the XUV proxy (based on the empirical behavior of the Sun-like stars).

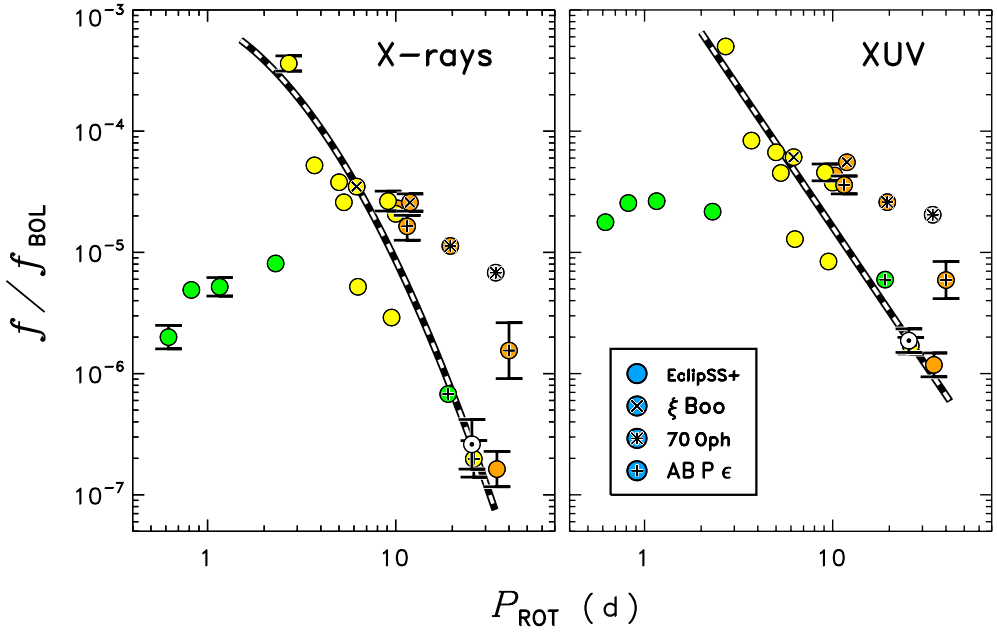

Figure 14. The left and right panels display, respectively, the variation of normalized X-ray fluxes, and the hybrid XUV index, versus stellar rotation period, $P_{\rm ROT}$. The unadorned circles are for the EclipSS subsample and the Related objects (together, "EclipSS+"). The adorned dots are for the various Reference stars, according to the legend in the right-hand panel: "AB P ϵ" refers to α Cen, Procyon, and ϵ Eri. The gray symbol for 70 Oph B indicates an uncertain rotation rate. Error flags ($\pm 1\,\sigma$), where visible, were based on standard deviations of logarithmic flux ratios over multi-epoch time series, if applicable; or simple measurement errors otherwise (which, for the X-rays, might involve instrumental inter-calibration uncertainties). Thick dashed curves are notional expectations for the rotation-activity connections.

Fig. 14 illustrates the two normalized fluxes versus the rotation period. Even in these log–log diagrams, there is significant scatter, more in the higher contrast X-rays then for the XUV proxy; and the suggestion of systematic trends among the three spectral type ranges: coolest stars falling to the right, Sun-like stars in the middle, and warmer stars to the left. This behavior mimics previous results of larger scale studies of chromospheric Ca II HK emission versus rotation period, which, as mentioned earlier, typically displayed a spectral-type dependent spread. (The analogous figure versus

[14] Prof. Noyes was fond of telling his Harvard students, "When in doubt, take a ratio!" The Rossby number is a perfect example of that mantra.

rotational velocity would roughly be the mirror image because of the approximate inverse correlation between $v_{\rm ROT}$ and $P_{\rm ROT}$.)

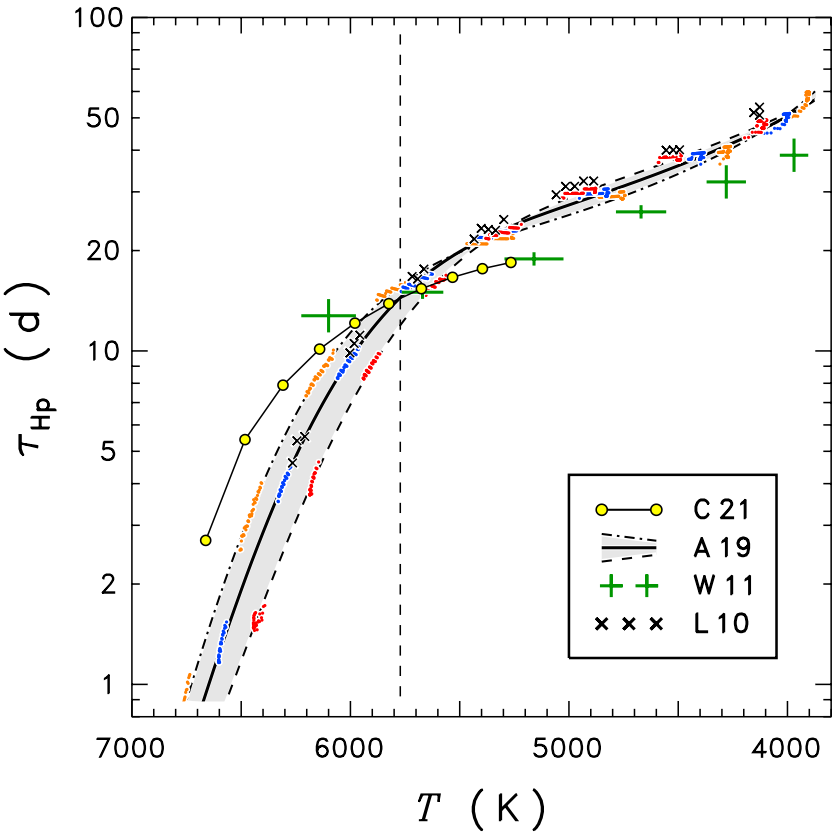

Figure 15. Comparison of various proposed convective turnover times versus stellar effective temperature. Abbreviated citations in the legend are spelled out in the text. The C21 and W11 points are semi-empirical; the other two, A19 and L10, are based on stellar structure models. The vertical dashed line marks the solar $T_{\rm eff}$. The dashed boundary curve for the A19 simulations refers to metal-rich models ([Fe/H]= +0.3); dotted-dashed is for metal-poor models ([Fe/H]= −0.5); solid curve in the middle is for solar composition. Small dots of various colors trace how the turnover time evolves during the Main sequence lifetime for the different masses and metallicities. Small x's are the equivalent evolution-resolved points for the L10 model grid, for [Fe/H]= 0.

Figure 15 compares various proposed convective turnover-time relations versus stellar effective temperature. While there are several different definitions of turnover times in common use in the literature, $\tau_{\rm Hp}$ (often called $\tau_{\rm c}$) was adopted here, namely an average of the convective velocities in the first pressure scale height above the base of the convection zone. Further, the extensive model grid of Amard et al. (2019: A19)[15] was adopted as a reference distribution, mainly because of the diversity of mass steps and metallicities used in that study compared with the more limited mass/composition coverage of other efforts. A19 calculated evolutionary tracks from the pre-MS to the terminal MS (TMS) phase. They included the effects of rotation on chemical mixing, internal angular momentum

[15] See also: https://cdsarc.cds.unistra.fr/viz-bin/cat/J/A+A/631/A77 .

redistribution, and wind angular momentum loss. The models covered the masses 0.2 $M_\odot$ (late-M) to 1.5 $M_\odot$ (early-F), and metallicities [Fe/H]= −1 to [Fe/H]= +0.3 (only the range (−0.5)–(+0.3) was considered here, which encompasses the [Fe/H] values of the Total EclipSS sample). The independent variable commonly used to describe the turnover times is a stellar color, such as $(B - V)$. Here, however, the effective temperature was adopted because it is a more fundamental parameter of the A19 evolutionary grid. The gray band in Fig. 15 encloses the span of the A19 $\tau_{\rm Hp}$ simulations considered. The dashed boundary curve refers to metal-rich models ([Fe/H]= +0.3); the dotted-dashed boundary curve is for metal-poor models ([Fe/H]= −0.5); and the solid curve in the middle is for solar composition. The small orange ([Fe/H]= −0.5), blue ([Fe/H]= 0), and red ([Fe/H]= +0.3) dots trace how the turnover time evolves during the Main sequence lifetime for the different discrete masses and metallicities, showing that $\tau_{\rm Hp}$ primarily tracks the stellar temperature on the MS, for a given composition. (The stars near solar mass evolve toward hotter temperatures during their ZMS to TMS evolution.) Further, the influence of metallicity is most pronounced on the warm side of the distributions, where convection zones are thin.

Corsaro et al. (2021: C21 in the Fig. 15 legend) proposed a semi-empirical relationship between $\tau_{\rm c}$ and Gaia $(BP - RP)$ motivated by stellar structure properties, derived through asteroseismic considerations, of a sample of about 60 F and G stars from the Kepler Field, which had been subjected to detailed oscillation analyses to infer key internal parameters including metallicity. The C21 relation versus Gaia color was converted to effective temperatures using the Casagrande et al. (2021) transformation described earlier. Further, the C21 model is based on parameter fits, rather than detailed integrations in stellar structure models, so it is not clear exactly which of the various "$\tau_{\rm c}$" definitions was in play. In fact, the absolute level of the $\tau_{\rm c}$ scale is not important within a given, self-contained study, only the relative scale. The absolute level is important, however, when comparing different theoretical calculations that have a consistent definition of $\tau_{\rm c}$. Evolutionary simulations of turnover times by Kim & Demarque (1996) suggested that the global, $\tau_{\rm g}$, and local, $\tau_{\rm c}$, time scales typically differ by a mass-independent multiplicative factor, at least on the MS. For this reason, the C21 curve was shifted in y to intersect the reference A19 solar-composition track at the solar effective temperature, to allow a fairer comparison.

Green error bars in Fig. 15 represent an empirical relation for the turnover time proposed by Wright et al. (2011: W11) in a detailed study of the X-ray rotation-activity connection in a large sample (>800) of late-type Main sequence stars, with well-documented rotation rates, mainly taken from nearby young clusters. The relation was derived by dividing the sample into narrow $(B - V)$ color ranges; then solving for the color-dependent term in the $C_{(B-V)}\, P_{\rm ROT}^{\beta}$ decomposition of the native $L_{\rm X}/L_{\rm BOL} \sim Ro^{\beta}$ dependence ($\beta \sim -2.7$ is the power law index of the rotation-activity connection in the unsaturated regime; $\beta = 0$ in the saturated regime). The derived color-dependent term was then fitted by a quadratic formula for the turnover time versus stellar mass. Here, that quadratic relation was translated into a dependence on $T_{\rm eff}$, using the Main sequence mass-temperature relation described by Landin et al. (2010). As with C21, the W11 empirical turnover times were scaled to intersect the A19 relation at the solar value.

Landin et al. (2010: L 10) considered, in great detail, the global (and local) convective turnover time scales for late-type stars in the mass range 0.6–1.2 $M_\odot$ (roughly mid-K to mid-F). Although the apparent focus of the study was on the pre-MS phase, the authors carried out evolutionary simulations up to the TMS for all the mass steps. Like A19, the stellar structure modeling included

the numerous and varied effects of rotation, and its evolution over time. Their simulations showed a strong decrease of τ_c during the pre-MS phase for all the masses considered, but by an age of about 100 Myr the curves had flattened out, leaving just the large systematic offsets related to the MS temperatures. The L10 relations over the MS lifetimes of each mass range are illustrated here as small x's (similar to the A19 dots) for a solar composition grid.

As noted by L10, their relation for τ_c is very similar to that obtained by Kim & Demarque (1996), a decade and a half earlier, based on a similar, though less advanced, modeling procedure (the Kim & Demarque curves are not displayed explicitly, to avoid further crowding an already congested diagram). Likewise, the L10 relations are quite similar to those of A19, especially in the steep turn-down toward the warmer effective temperatures, where convection zones are thinning rapidly and convective velocities are increasing ($\upsilon_c \sim T_{\rm eff}^2/\sqrt{\rho}$); and the less steep rise toward the cooler types, where convective velocities are decreasing, the convection zones are thickening as a fraction of the stellar radius, but the stars themselves are becoming smaller. The (scaled) semi-empirical relations of C21 and W11 are similar to one another over the overlapping temperatures, while C21 shows a less precipitous drop at the warmer temperatures than A19, and W11 falls somewhat below A19 among the cooler types, although the slopes roughly are parallel.

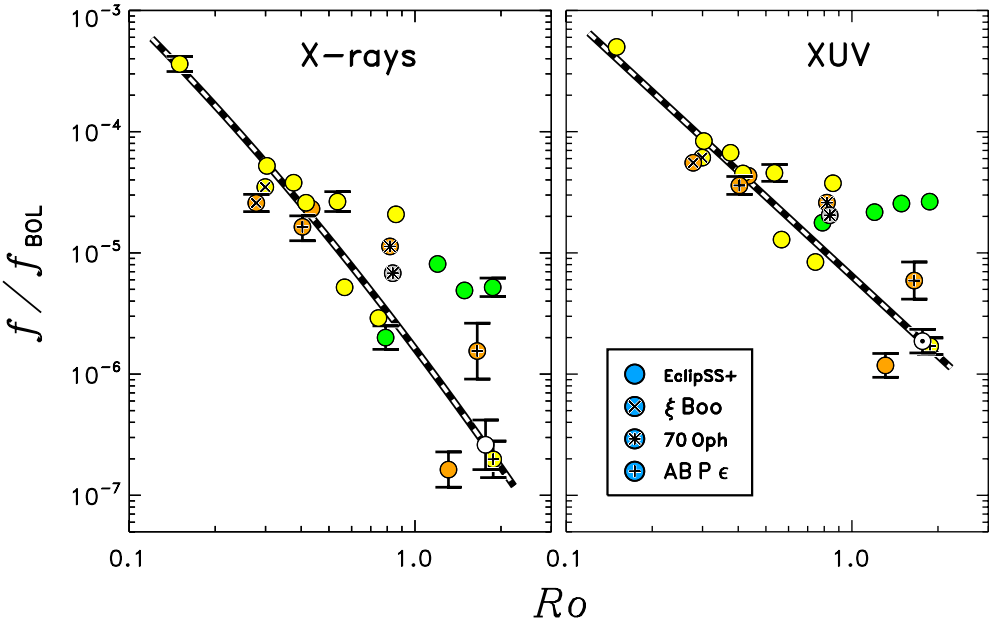

Figure 16. Results of applying the A19 τ_c versus $T_{\rm eff}$ relation for solar composition to the Total EclipSS sample, then displaying the stellar X-ray (left panel) and XUV (right panel) fluxes against the corresponding Rossby numbers. Symbol marking and color-coding are the same as in previous figures. Thick dashed power law in the left hand panel, fitted to a subset of the Sun-like stars, has a slope of -2.2.

Figure 16 depicts the outcome of applying the A19 τ_c versus $T_{\rm eff}$ relation for solar composition to the Total EclipSS sample, then displaying the stellar X-ray and XUV fluxes against the corresponding Rossby numbers. The symbol marking and color-coding are the same as in previous figures. Compared to Fig. 14, the scatter of the points along the *Ro* axis is reduced, especially for the K dwarfs, although the F dwarfs still exhibit a noticeable spread, now shifted toward the right. The

dark dashed curves in each panel are parabolic (X-rays) and linear (XUV) log-log fits to the Sun-like dwarfs (yellow symbols), excluding one discrepant point (HD 150706, discussed later).

Figure 17 schematically repeats the A19 and C21 + W11 curves from Fig. 15, together with empirical estimates of turnover times for the Total EclipSS sample, derived by forcing all the points in Fig. 16 to fall exactly on the consensus relation for the normalized XUV proxy flux versus *Ro* power law (based on the Sun-like dwarfs, minus HD 150706). Error bars, displayed when larger than the symbol size, were calculated from the $\pm 1\,\sigma$ XUV ranges noted earlier (the most conspicuous are from "cycle variability," especially the Reference stars α Cen B and the Sun). The XUV flux, according to the calibration template shown in the right hand panel of Fig. 16, depends on the Rossby number as $\sim Ro^{-2.2}$, so that the uncertainty range of the associated τ_c would be compressed.

The general behavior of the empirical turnover times of the Total EclipSS sample is encouragingly systematic. The hotter stars (green) show a steep rise in τ_c with decreasing surface temperature roughly following the C21 and A19 curves, presumably as the convection zone transitions from extremely thin to just moderately thin (a glaring exception is the subgiant Procyon). The more Sun-like stars cluster around the mean trend line of the A19 theoretical relation. The cooler late-G and early/mid-K stars bump up somewhat, bracketing the A19 trend.

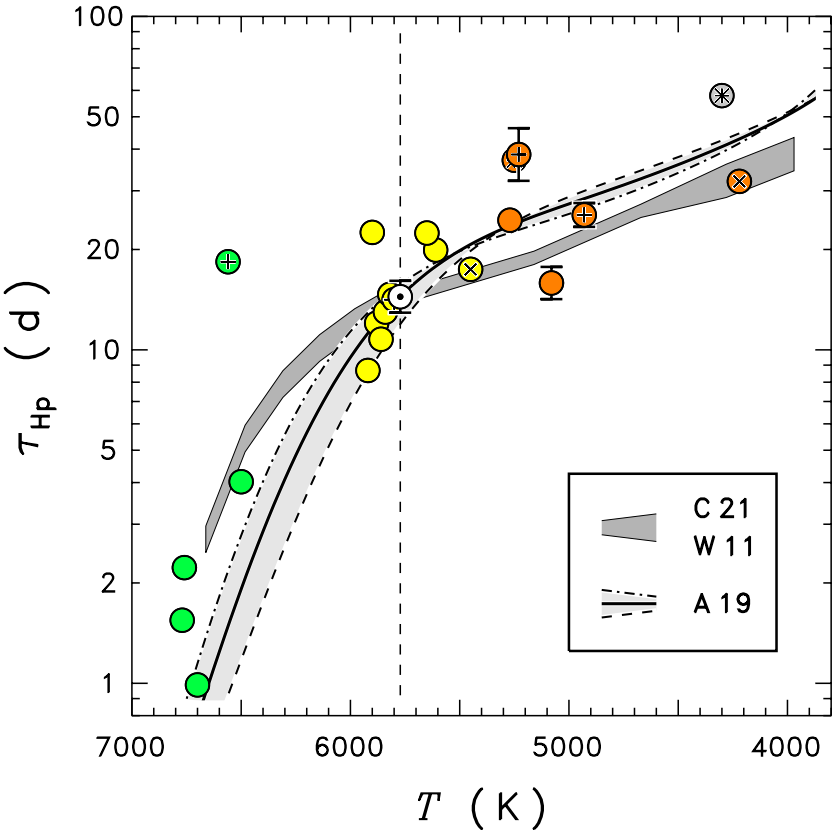

Figure 17. Similar to Fig. 15, but now including empirical turnover times derived from Fig. 16.

One outlier in the diagram, mentioned earlier, is the early-G dwarf HD 150706 (isolated yellow dot to the left of the vertical dashed line, above the main trend). The τ_c versus T_{eff} curve appears to be

well-defined for the objects close to the Sun in temperature, and the rotation period of the EclipSS star seems unassailable from the TESS photometry. The dominant, persistent TESS period, 10 d, would have to be halved in order for HD 150706 to agree with the other G stars. As was noted earlier, the golden rule for photometric periods is that it would be very unlikely to find twice the true value.

Another outlier is the old, slightly metal-poor late-G dwarf τ Cet, lowest of the orange points, well below the main trend line. The star already has a long HK period, 34 d, and it seems unlikely, but not impossible, that this is a harmonic of a twice longer period. To be sure, a longer period would fit in better with the low activity level of τ Cet. Alternatively, τ Cet has the coolest coronal EMD of all the stars considered here, and it is conceivable that even the large XUV flux multiplier for the 0.1–2.4 keV X-rays might have been underestimated by a factor of two, or more, which would elevate the star into better agreement with the XUV trend line, and also with α Cen B, which has a similar rotation period, similar Gaia color, and is similarly old.

Speaking of α Cen B, it falls above the main A19 trend, paired with, and partially obscuring, the point for 70 Oph A. A shorter rotation period would bring it back in line, but as argued earlier the golden rule says that the apparent rotation period (from HK in this case) is unlikely to be twice the true period. 70 Oph A, similar in temperature to α Cen B, also falls above the main trend by a similar amount, but has a rotation period half that of α Cen B, and an XUV flux about five times higher (another reason it would be unlikely that α Cen B has a much shorter rotation period than its nominal 40 d). 70 Oph B also sits above the main A19 trend with about the same offset as α Cen B and 70 Oph A. To be sure, α Cen B is slightly metal-rich compared with the Sun, but the A19 distributions are much less responsive to composition among the cooler types.

At the same time, the AB components of the other late-type binary, ξ Boo, together with Reference star ϵ Eri, all fall just below the main A19 trend, closer to the (scaled) W11 distribution. One possible conclusion is that the τ_c versus $T_{\rm eff}$ relation is missing something, an additional parameter perhaps, in the K types where the trends ostensibly are bifurcated; whereas the A19 reference curve appears better defined among the G dwarfs (with the possible exception of HD 150706 mentioned earlier). On the other hand, the behavior among the K stars is anchored by relatively few objects, and it remains to be seen whether additional candidates would clarify the mean trend, or instead maintain a spread that would argue for a hidden parameter.

Then, there is Procyon, the green crossed point far to the left of the main trend. The MS τ_c relation predicts a short turnover time at Procyon's temperature, whereas the inferred rotation period of the subgiant is relatively long. The result is a large Rossby number (in fact, off-scale in Fig. 16). However, Procyon's true turnover time undoubtedly must be much longer than suggested by the dwarf-star relation, because the lower-gravity F proto-subgiant would have a different convective structure than a higher gravity dwarf, especially in the effective temperature range where the convective zone is thinning rapidly toward warmer temperatures. In fact, Kim et al. (1996; their Fig. 3), show a factor of 2–3 spike in τ_c during the initial post-MS evolution of (the less extreme case of) a 1.2 $M_\odot$ star (Procyon is 1.5 $M_\odot$). Thus, the outlier nature of Procyon should not be concerning.

The promise of the diagram is that if the apparent systematic behaviors of τ_c with $T_{\rm eff}$ could further be refined, by additional supporting observations perhaps, it would open up the prospect of being able to characterize the total high-energy power of late-type sources simply by means of a one-parameter description, namely the rotation period (accessible for the more active stars by TESS photometry, although with the caveats mentioned earlier). Alternatively, if the evident dispersion

among the K types is maintained with further observations, then possible hidden parameters in the Rossby formulation would have to be entertained.

Finally, it should be mentioned that the Rossby number is only one possibility among several formulations that attempt to correlate, say, X-rays against some combination of stellar properties over large samples of FGK stars. For example, Reiners et al. (2014; and references to previous work therein) proposed that a relation of the form, $L_{\rm X}/L_{\rm BOL} \sim P_{\rm ROT}^{-2} R^{-4}$ was a more optimum fit to the Wright et al. (2011) X-ray/rotation sample than the Rossby formulation (although the Wright et al. model of the turnover time in Fig. 15 is somewhat flatter than the A19 theory, so perhaps their Rossby approach was non-optimum to begin with). The Reiners et al. formulation certainly would tighten up Fig. 14, since the rightward shifted K-type outliers, with respect to the more Sun-like stars, would be pulled back toward the main relation owing to the smaller sizes of the cooler stars. Exploring these non-Rossby possibilities is beyond the scope of the present study, but might be worth pursuing in the future with more extensive high-quality datasets of the current type. The main advantage of the Rossby approach is that it is more closely connected to theoretical descriptions of terrestrial and cosmic dynamos, whereas empirical fits to multiple stellar parameters might have a less obvious connection to the contemporary theory. Of course, the empirical parameter descriptions might help steer the theory in a new direction, so all options should be considered.

4. SUMMARY AND CONCLUSIONS

This largely observational study has compiled extensive multi-wavelength high-energy fluxes of a sample of nearby Sun-like stars with well-defined stellar properties and generally reliable rotational rates (some of which were derived here from recent TESS time series). Part of the sample was drawn from a previous short-FUV survey of FGK dwarfs at high Ecliptic latitudes that has especially benefitted, in terms of rotation periods, from the added coverage by TESS (whose scan pattern favors the Ecliptic polar regions). Others of the sample had been monitored by the Mt. Wilson HK Project, and have firm rotation periods deduced from long-term records of chromospheric Ca II modulations. A few of the sample members have less solid measures of rotation, usually from photospheric line broadening coupled with some knowledge of the likely stellar spin axis orientation. The Sun was included as a bone fide sample member, thanks to multi-wavelength high-energy irradiance measurements over recent solar Cycle 24, and of course, its well known sidereal rotation period (albeit which varies somewhat with latitude, faster at the equator, slower in the polar regions, thanks to differential rotation).

A subset of the sample had been subjected to multi-epoch surveillance by a series of joint Chandra/HST programs, whose primary intent was to determine the time scales of long-term high-energy starspot cycles analogous to the Sun's iconic 11-year example; but secondarily to estimate the range of flux variability experienced by each star in coronal X-rays and subcoronal FUV emissions, as a gauge of the, up to this point, poorly characterized "activity variability bias." The latter affects any study that attempts to compare single- or few-epoch high-energy observations of late-type stars against basic stellar properties, such as rotation (in an effort to probe the internal magnetic dynamo responsible for the non-classical activity in the first place). A high degree of activity variability would translate to enhanced scatter in such comparative diagrams, which might obscure any fundamental connections otherwise present.

X-ray pointings on the sample members mainly came from Chandra, specifically its HRC-I camera, but in other cases from HRC-S and ACIS-S. Additional X-ray datasets were drawn from the archives

of ROSAT and XMM-Newton. FUV fluxes of the sample members were drawn from new and archival observations by the two UV spectrographs on HST: COS and STIS. The medium- and high-resolution FUV spectra from these two instruments were subjected to a specialized emission profile measurement strategy that involved a pseudo-Gaussian formalism developed in previous Papers IV and V of this series. The X-ray and FUV observational material generally was of very high quality, especially for the several stellar participants in multi-epoch monitoring programs (about a third of the total sample).

An important departure of the present program, with regard to previous installments of the Trenches series, was the adoption of a new reference X-ray energy band, 0.1–2.4 keV (ROSAT PSPC standard range), which extends to both softer and harder energies than the previously used 0.2–2 keV reference (the latter similar to that of the ROSAT WGA catalog). The low-energy extension (factor of two) was especially important to match the soft response of the HRC-I camera, to capture the dominantly soft emissions of low-activity coronae like the Sun's, and other nearby middle-age G dwarfs, for the purpose of accounting the total coronal radiative energy loss (a major objective of the present study, as described next). The (more modest) high-energy extension helped access the hottest coronal emissions of the most active G stars, whose emission-measure distributions can extend to temperatures of several tens of MK.

A parallel effort was undertaken to devise a global metric for the total coronal (and subcoronal) radiative losses as a function of stellar activity, as a proxy for the high-temperature magnetic heating of the stellar outer atmosphere. In practice, this "XUV" hybrid flux was constructed from high-energy observables by applying suitable flux multipliers to the 0.1–2.4 keV X-rays and a variety of key FUV fluxes (some of which were stand-ins for crucial emissions in the 250–1150 Å EUV range, which is challenging to observe in stars owing to interstellar absorption as well as current instrumental limitations). The X-ray emissions in the 0.05–12 keV range were found to dominate the overall coronal energy output for X-ray surface fluxes $\log F_{\rm X} \geq 5$ erg cm^{-2} s^{-1}, which is a relatively modest activity level among the Sun-like stars. However, at the very lowest activity levels, $\log F_{\rm X} \sim 4$—similar to the Sun and solar neighbors α Cen A and τ Cet—the longer wavelength $\lambda \geq 250$ Å EUV/FUV contribution was comparable. The XUV proxy flux likely dominantly arises, on all types of cool stars, from magnetic reconnection heating in concentrated active regions, such as commonly appear on the Sun during the heights of the solar spot cycle. As such, the hybrid XUV flux should be strongly linked to the specific areas of surface magnetic activity that ultimately arise from the internal dynamo mechanism, which is thought to derive its power from turbulent convection and (differential) rotation.

An initial branch of the analysis compared the pseudo-Gaussian profile parameters obtained from the sample members that had been observed uniformly with the STIS medium-resolution FUV echelle. These spectra have more than twice the resolution of the sister COS spectrograph, which is important for obtaining reliable line-shape measurements, although the targets were restricted to relatively nearby bright late-type stars to achieve high S/N. It was found that the sub-Gaussian line profiles (with exponents $a \sim 1.5$ versus $a = 2$ for a pure Gaussian: see eq. 1), described for the subcoronal lines of the Sun, α Cen AB, and Procyon in previous Paper V, carried over to the other STIS stars, which spanned a similar range of spectral types, from G0 to K2, but a much wider spread of intrinsic activity levels. One remarkable finding was that the *redshifts* characteristic of subcoronal lines like Si IV and C IV on the Sun, and are thought to be associated with downdrafts of cooling coronal

material, are repeated at similar amplitudes in all the G dwarfs, regardless of activity status. Further, the shifts were similar among the late-G and early-K stars, again independent of activity, but the amplitudes uniformly were less than seen in the early-G dwarfs. These systematics potentially are important clues to the heating and cooling processes that operate in coronal magnetic loops, which appear to be universal, at least within the current modest, but representative, sample.

A second branch of the analysis followed the previous Trenches series by constructing a series of flux–flux scatter plots, each contrasting various spectral diagnostics against a reference; covering the broad reach of plasma temperatures involved in the stellar outer atmosphere: chromosphere ($T \lesssim 10^4$ K); transition zone ($2{\times}10^4$ K $\lesssim T \lesssim 8{\times}10^5$ K); and corona ($\gtrsim 1$ MK) (these ranges are somewhat arbitrary and overlap to some extent). The current set of flux–flux diagrams encompassed a wider range of activity, more densely, than the original 49 members of the EclipSS sample, which was dominated by relatively quiet dwarf stars. Further, the new flux–flux diagrams extended to additional diagnostics, especially X-rays and the long-FUV spectra of the EclipSS subsample (the ten FUV brightest of the original Ecliptic poles survey) and the other Related (additional G dwarfs) and Reference objects (subjects of multi-epoch X-ray and FUV monitoring). The long-FUV spectrum contains the key C IV doublet, which itself is a significant component of the FUV part of the XUV radiative loss, and is well-correlated with—and thus serves as a proxy for—other important, but, "hidden" emissions of the EUV spectrum (especially, He II 303 Å). Another, previously less-well appreciated, long-FUV diagnostic is He II 1640 Å, which empirically displayed the best correlation, of all the FUV features, with the hybrid XUV total coronal radiative loss. The He II Balmer-α line is thought to at least partially form by recombination following photoionization of He^+ by coronal radiation. The strong correlation with the XUV flux perhaps is a direct result of that association.

The flux–flux diagrams presented here are the highest quality possible with the existing carefully curated stellar sample, which is weighted toward Sun-like G dwarfs (because of the solar orientation of this series), but extends up to the hotter early-F types, as well as down to the cooler mid-Ks. The flux–flux diagrams typically showed tight power-law correlations between any of the diagnostic pairs, normally with steeper slopes when comparing a hot diagnostic like subcoronal C IV or coronal X-rays against a cooler species such as chromospheric O I or Si II. The F stars often displayed correlations separated from the main trends of the G/K dwarfs; and there were possible further offsets among some of the sample members due to abundance effects, either low metallicity (Si, Mg, and Fe *deficits* versus CNO) or in some cases chemical fractionation (i.e., FIP mechanism: Si, Mg, and Fe *enhancements* versus CNO). Given the many decade ranges of the flux–flux diagrams, the "activity bias" mentioned earlier empirically was found to play only a minor role; mainly important for the lower activity dwarfs like the Sun, affecting the 0.1–2.4 keV X-rays the most, with a lesser influence on the FUV emissions.

The fact that the flux–flux diagrams display such coherent correlations across species that arise throughout the chromosphere–corona, where temperatures range over a factor of 10^2 even in low-activity stars, and 10^3 among their active cousins, emphasizes that the overt manifestations of magnetic activity must vary systematically with some fundamental set of stellar properties. As noted in Paper IV, spatially resolved solar Si IV (brightest subcoronal emission recorded by the IRIS spectrometer) displayed, at the finest spatial scales, the full range of surface fluxes (factor of ∼10) seen between quiet and very active G dwarfs, even though the globally average solar FUV fluxes showed a much more modest variation over the sunspot cycle (only ∼50 %, or so, for Si IV). The spatial

behavior of Si IV on the Sun, coupled with the systematic correlations of the flux–flux diagrams, reinforces the old idea that the degree of stellar X-ray/FUV activity depends mainly on how much of the stellar surface is covered by spatially concentrated active regions. The corollary is that low-activity stars, e.g., the Sun at cycle MIN, essentially are devoid of active regions, while the highest activity objects, such as the G dwarf EK Dra of this study, are nearly completely covered by magnetic regions essentially all of the time. Of course, there likely are nuances concerning how the magnetic areas might mutually interact when in close proximity that would not apply to low-activity stars with their sparser, more disconnected spot coverage. Such effects might partially be responsible for the nonlinear behavior of the key flux–flux power laws.

The third branch of the analysis considered how the high-energy XUV proxy flux might vary with parameters that could be more closely tied to the internal dynamo mechanism, namely various incarnations of the stellar rotation. The simplest initial candidate, $P_{\rm ROT}$, failed to yield a coherent systematic correlation over the wide range of activity levels and stellar types encompassed by the Total EclipSS sample. Instead, a better choice was the so-called Rossby number—a dimensionless ratio of the rotation period to a time scale associated with the stellar envelope convection—which appears in dynamo theories in a variety of settings, from terrestrial to cosmic. An important role for the Rossby number had already been recognized in early surveys of Ca II HK activity, as well as in more recent studies focused on coronal X-rays.

This project adopted the tactic to establish an empirical Rossby number for each of the sample stars, through a calibration of the key convective turnover time scale (denominator of the Rossby ratio) against the hybrid XUV flux, which, as argued earlier, should be an accurate tally of the dissipation of magnetic free energy by reconnections (itself likely correlated with the total unsigned magnetic flux produced by the internal dynamo). The, perhaps arguable, assumption was that all late-type stars should obey a coherent relationship between the XUV proxy flux and the Rossby number. The template for the calibration was chosen to be a simple power law, based on the empirical behavior of the G0–G7 Sun-like stars of the sample, which had initially been assigned turnover timescales, $\tau_{\rm c}$, from theoretical considerations (Amard et al. 2019). For the most part, the sample stars had well-determined rotation periods, so any leeway in the Rossby number would devolve from the $\tau_{\rm c}$ part.

Given the designated power-law calibration of $f_{\rm XUV}/f_{\rm BOL}$ versus Ro, an empirical $\tau_{\rm c}$ could be derived for each object. The resulting calibrated $\tau_{\rm c}$ values were then compared against the effective temperature, $T_{\rm eff}$, the fundamental parameter of the A19 stellar structure models (and which is strongly linked to the Gaia broadband $(BP - RP)$ color among FGK stars: Casagrande et al. 2021, also Paper III). The gross characteristics of the $\tau_{\rm c}$ versus $T_{\rm eff}$ distribution obtained in that—albeit circuitous—way are: (1) a steep rise among the early-to-mid F dwarfs; (2) a rightward jog to the G types segueing into another steep rise; then (3) a bending over to a more shallow slope among the late-G and early-to-mid K dwarfs. The empirically derived values were in general agreement with several different realizations of theoretical and semi-empirical turnover times.

One striking feature of the empirical $\tau_{\rm c}$ is the excellent internal agreement for the G dwarfs, despite a wide diversity of activity levels, aside from one anomalous point; but larger apparent scatter among the K dwarfs (although defined by fewer objects, one of which, 70 Oph B, lacks a validated rotation period). If the K dwarf scatter is real, then it would suggest that the single-parameter Rossby

description is not complete for these cooler dwarfs, and that there might be hidden dependencies yet to be uncovered.

To be sure, the Rossby description is limited to mean activity levels, and cannot accommodate stellar magnetic cycles, so the one anomalous G dwarf, and the several discrepant K dwarfs might be caused by cyclic variability, caught in an inopportune epoch as far as the mean behavior is concerned. This is an issue because the XUV proxy depends strongly on the 0.1–2.4 keV X-ray flux, for all the stars more active than the Sun, and the Sun itself displayed a roughly factor of four MIN to MAX variation in $f_{(0.1-2.4)}$ over Cycle 24; and a similar factor, $\sim$3, for solar twin α Cen A over its most recent 19-year cycle. Further, somewhat higher activity α Cen B had a roughly factor of seven X-ray swing between its MIN and MAX during the HRC-I era, 2005–present.

On the other hand, moderately active ϵ Eri exhibited an only $\sim$25 % 1 σ dispersion in its 0.1–2.4 keV fluxes over the ten 4XMM-DR11 epochs considered here. This much reduced cycle variability might carry over to ξ Boo B and the 70 Oph K dwarfs, which are similar to ϵ Eri in normalized activity levels. If the trend of larger amplitude X-ray cycles at the lower activity levels (albeit so far based on three points) carries over to all the G and K stars, then it would be more difficult to explain away the discrepancies in the τ_c diagram by cycle variability. The ξ Boo and 70 Oph stars currently are under evaluation in this regard, with only two years worth of X-ray and FUV observations collected to date, so it would be premature to speculate whether their high-energy cycle amplitudes might be modest like ϵ Eri, or more extreme like α Cen B. Lastly, as mentioned earlier, the influence of cycle variability will be muted to some extent because for a known rotation period, the turnover time varies roughly as the square root of the XUV flux.

The other conspicuous feature in the empirical τ_c versus $T_{\rm eff}$ diagram is the jog between the F and G dwarfs (excluding the F-type proto-subgiant Procyon, for reasons described earlier). This displacement might result from systematics associated with the assumption that the XUV proxy flux has the same functional dependence on the dynamo mechanism (i.e., the same initial power-law template) for the F stars as for the more deeply convective G dwarfs. In fact, the F stars of the sample span a healthy factor of about four in $P_{\rm ROT}$, mostly on the short-period side, yet the associated $f_{\rm XUV}/f_{\rm BOL}$ values vary by only an anemic 50 % (minimum to maximum) and just 15 % 1 σ, effectively constant in the many decade comparison. Consequently, the τ_c for these stars will be roughly proportional to the $P_{\rm ROT}$, to achieve similar *Ro* at the similar XUV fluxes. Because the temperatures of the F stars span only a narrow range, the imposed factor of $\sim$4 variation of τ_c translates to a steep dependence. At this point, it is not known whether the nearly constant normalized XUV fluxes of the F stars of the Total EclipSS sample are coincidentally that way because of a natural steep τ_c versus $T_{\rm eff}$ relation, as seen in the C21 and A19 curves; or that the constancy is more fundamental, perhaps resulting from an analog of the Sun's surface dynamo (whose magnetic productivity would depend more sensitively on the stellar temperature than the rotation rate).

Standing at odds to the latter possibility is the fact that the stellar XUV proxy fluxes already are normalized to the bolometric values, which implicitly contain the factor $\sigma\,T_{\rm eff}^4$. That normalization would compensate to some extent for the change in the photospheric kinetic energy density—power source for the local dynamo—with effective temperature. Consequently, the bolometric normalization would tend to produce a constant normalized XUV flux response associated with the local dynamo, if the magnetic flux generation primarily is directly proportional to the convective energy density. In fact, the F stars in question have normalized XUV fluxes about an order of magnitude higher

than that of the Sun, but $T_{\rm eff}$ only about 20 % larger in the worst case, so the local dynamo would have to have a—perhaps unrealistically—steep dependence on $T_{\rm eff}$ between early-G and early-F. In any event, the F stars display photometric modulations in the TESS time series, normally a sign of surface magnetic inhomogeneities such as produced by the internal dynamo.

Both of these aspects of the empirical $\tau_{\rm c}$ curve—the F stars on the one hand and the K stars on the other—could be addressed by future observations of the type described here. The F stars are easier targets from the point of view that they tend to be faster rotators, and thus are more accessible to modulation analysis by TESS, or future high-precision photometric instruments in space. The K stars of the solar neighborhood would be more challenging because their rotation periods typically are long, a month or more, so that the most viable source of rotation periods would be the existing Mt. Wilson HK sample. A different choice might be to look beyond the solar neighborhood to the faster-rotating K dwarfs of nearby young clusters, especially the Hyades and Pleiades, for which extensive optical photometric surveys of rotation periods have been carried out from the ground (e.g., Delorme et al. 2011; Hartman et al. 2010) as well as by the extended Kepler mission (K2: e.g., Douglas et al. 2019; Rebull et al. 2016). The downside of the cluster option is that the K dwarf members will be much fainter in X-rays and the FUV than those of the solar neighborhood, and thus more challenging targets for Chandra, XMM-Newton or HST. In addition, the faster rotating members of the Pleiades (five times younger than the Hyades) likely would fall in the saturated X-ray regime, where empirically the coronal radiative losses become decoupled from the Rossby number (e.g., Wright et al. 2011).

There also is the case of 70 Oph B, for which the HK Project was unable to establish a definitive rotation period. The deviation of the empirical $\tau_{\rm c}$ of the mid-K dwarf could be repaired if the rotation period of the star were half the value estimated by Baliunas et al. from the HK rotation-activity connection, which, to be sure, is not especially well defined at the longer periods among the K dwarfs (owing to sparse samples). If the rotation period of 70 Oph B is that much shorter, then spectroscopic line broadening might be a viable alternative, especially since a reasonable guess of the inclination of the star could be obtained from the orbit (the $\sin i$ factor is near unity).

If future observations could explain away the discrepant points in the $\tau_{\rm c}$ diagram, then the Rossby analysis would be placed on a firmer footing. Alternatively, future studies might demonstrate that the deviations in the diagram are significant, and consequently might be pointing to additional stellar properties that must be considered (e.g., Reiners et al. 2014). Again, the power of the Rossby approach would be to have a one-parameter way of estimating the high-energy radiative losses of arbitrary stars, say in a broad survey, solely on the basis of their rotation periods and Gaia colors; or to follow the high-energy history a particular-mass star along its MS evolutionary track, as its temperature rises and its rotation slows over time (due to coronal wind braking).

There is a final point to be made concerning the low-activity end of the stellar distribution, anchored by the Sun itself, but including the old dwarfs α Cen A and τ Cet (although the latter is somewhat outside the Sun-like class). All three of these stars display rotational modulations, in Ca II HK or the FUV, so all must have active regions present, at least at the higher phases of their magnetic cycles. Tau Cet is a bit of an anomaly in that respect because it is a so-called "flat-activity" star with no apparent long-term HK cycle (Judge et al. 2004). Nevertheless it does display rotational modulations, at least at times, so it must have an asymmetric HK brightness pattern, at times; normally a sure sign of magnetic active regions. Thus, all three stars fit, to some extent, within the

Rossby paradigm, albeit in a minimalist way. At the same time, there are other flat-activity G dwarfs that appear stalled in spotless minima for decades at a time, at least in terms of chromospheric HK variability. To be sure, the HK index is a very low-contrast cycle indicator. X-rays are much better, but very few stars so far have long-term records of X-ray variability. (The eROSITA multiple sky surveys might change that story, but the known flat-activity stars generally are faint in X-rays to begin with, so obtaining reliable time series might be out of reach for the majority of them.) The flat-activity stars must be dominated by the local dynamo, so the expectation is that these stars would collectively display normalized XUV fluxes that were relatively independent of the Rossby number, creating a cloud of points at the floor of the XUV versus *Ro* relation, just below the Sun and α Cen A (noting that the flat-activity stars universally are slow rotators so that there might not be a horizontally extended "foot," which otherwise might be present if there were a significant spread of rotation periods among those stars at a given effective temperture). In fact, many of the G dwarfs in the original minimally biased EclipSS sample of Paper III had normalized subcoronal flux levels just below that of solar MIN, so would be candidates for local dynamo dominance. Nevertheless, as emphasized in previous papers of this series, it is remarkable that the Sun apparently sits at a tipping point between local dynamo control and the cycling internal dynamo, apparently swinging from one extreme to the other over time (for example, the 17th century Maunder Minimum versus the 19th century Carrington superflare event), without, so far, a convincing long-term pattern or controlling mechanism.

Certainly, there is much still to be learned concerning the remarkable magnetic behaviors of the cool stars, the most habitation-friendly abodes in the Galaxy, but with a dark side: potentially fiendish high-energy radiation and wind environments, inimical to planetary atmospheres, especially during the initial phases of stellar youth. Building a coherent story will require a series of dedicated high-energy observations, coupled with more extensive estimates of stellar spin rates, especially at the longer periods ($\gtrsim$ month) common among the K dwarfs in general and the older G dwarfs in particular. Many of these pieces already are in place (e.g., TESS and eROSITA, together with contemporary X-ray and FUV missions), but the assembly will be complicated, and the instruction manual is missing most of its pages.

This work was based on observations from Chandra X-ray Observatory, collected and processed at the Chandra X-ray Center, operated by the Smithsonian Astrophysical Observatory, under contract to NASA; and observations from Hubble Space Telescope, collected at the Space Telescope Science Institute, operated by the Associated Universities for Research in Astronomy, also under contract to NASA. TRA thanks SAO and STScI for their grant support of this work. DB thanks the TESS mission for their support. This study made use of public databases maintained by CDS, Strasbourg, France, as well as the Gaia Data Archive. HST COS and STIS spectra and TESS light curves were obtained from the Mikulski Archive for Space Telescopes at STScI in Baltimore, Maryland.

APPENDIX

A. X-RAY MEASUREMENTS OF α CEN AB AND PROCYON IN THE NEW 0.1–2.4 KEV BANDPASS

The following two tables provide revised Chandra HRC-I X-ray measurements of α Cen AB and Procyon based on the newly adopted extended 0.1–2.4 keV bandpass. ECFs were determined for each observation based on the EMD optimization scheme described previously.

Table A1. *Chandra* HRC-I Pointings: α Cen AB (0.1–2.4 keV)

ObsID	UT_{mid}	t_{exp}	$(CR)_A$	$(CR)_B$	$(L_X)_A$	$(L_X)_B$
	(yr)	(ks)	(cnt s^{-1})		(10^{27} erg s^{-1})	
1	2	3	4	5	6	7
6373	2005.805	5.15	0.45±0.04	2.20±0.15	0.75	3.40
6374	2006.362	5.11	0.45±0.03	0.99±0.07	0.75	1.55
6375	2006.960	2.67	0.41±0.04	0.94±0.10	0.69	1.48
7433	2007.469	5.04	0.45±0.04	0.71±0.04	0.75	1.13
7434	2007.961	5.11	0.47±0.04	0.74±0.04	0.79	1.17
8906	2008.389	10.08	0.46±0.03	0.81±0.08	0.77	1.28
8907	2008.961	9.34	0.47±0.05	0.87±0.06	0.79	1.37
9949	2009.409	10.06	0.43±0.04	1.48±0.06	0.72	2.30
9950	2009.949	10.05	0.49±0.04	1.83±0.08	0.82	2.84
10980	2010.335	9.76	0.62±0.05	3.32±0.65	1.03	5.14
10981	2010.808	10.03	0.49±0.05	2.75±0.19	0.83	4.31
12333	2011.437	4.88	0.63±0.05	2.20±0.15	1.07	3.50
12334	2011.993	10.07	0.56±0.04	3.35±0.17	0.96	5.37
14191	2012.473	10.10	0.76±0.07	2.82±0.10	1.30	4.57
14192	2012.950	10.06	0.92±0.06	2.38±0.10	1.57	3.90
14193	2013.480	10.59	0.83±0.07	1.93±0.10	1.44	3.21
14232	2013.963	10.05	0.95±0.05	2.01±0.10	1.66	3.38
14233	2014.477	9.62	0.86±0.07	1.40±0.09	1.52	2.39
14234	2014.999	10.11	0.83±0.06	1.64±0.16	1.49	2.82
16677	2015.346	10.07	1.10±0.07	1.36±0.07	1.96	2.37
16678	2015.810	10.08	1.13±0.06	1.01±0.05	2.04	1.79
16679	2016.330	10.03	0.89±0.05	1.19±0.08	1.64	2.12
16680	2016.771	10.01	1.06±0.05	1.31±0.06	1.96	2.36

Table A1 *continued on next page*

Table A1 *(continued)*

ObsID	UT_{mid}	t_{exp}	$(CR)_A$	$(CR)_B$	$(L_X)_A$	$(L_X)_B$
	(yr)	(ks)	(cnt s^{-1})		(10^{27} erg s^{-1})	
1	2	3	4	5	6	7
16681	2017.335	9.99	0.96±0.06	2.11±0.18	1.80	3.82
16682	2017.823	10.00	0.74±0.05	2.64±0.12	1.42	4.82
20987	2018.378	5.12	0.96±0.06	3.64±0.18	1.84	6.71
21572	2018.967	5.11	0.68±0.04	2.96±0.10	1.35	5.55
21573	2019.391	5.10	0.76±0.06	3.26±0.10	1.51	6.17
21574	2020.097	5.07	0.56±0.04	3.02±0.16	1.15	5.82
21575	2020.428	5.11	0.49±0.06	3.90±0.44	1.02	7.56
21576	2021.761	4.98	0.42±0.04	1.16±0.08	0.91	2.36
21577	2021.761	5.12	0.41±0.04	1.21±0.08	0.89	2.46

NOTE—Col. 3 exposure times include compensation for dead-time. Cols. 4 (A) and 5 (B) count rates were time-filtered to remove flare enhancements, if any; and were adjusted for the 95% encircled energy of the $r = 1.''5$ detect cell. Cited uncertainties reflect standard deviations of time-binned count rates, including the influence of flares, with respect to reported flare-filtered averages. Cols. 6 (A) and 7 (B) X-ray luminosities (0.1–2.4 keV) were calculated from optimized ECFs derived from the EMD modeling described in the text; $d = 1.338$ pc (Kervella et al. 2017); and including a correction for the adopted time-dependent sensitivity decline of HRC-I (2 % per year since 2010; constant prior to 2010). $(L_X)_\odot \sim 0.5$–2.2 in same energy band and luminosity units, over recent (weak) sunspot Cycle 24.

Table A2. *Chandra* HRC-I Pointings: Procyon (post-2008.0; 0.1–2.4 keV)

ObsID	UT_{mid}	t_{exp}	CR	L_X
	(yr)	(ks)	(cnt s^{-1})	(10^{27} erg s^{-1})
(1)	(2)	(3)	(4)	(5)
8908	2008.020	4.78	1.62±0.02	16.3
18304	2016.183	9.68	1.45±0.01	16.5
18305	2016.685	10.06	1.50±0.01	17.4
18306	2017.254	10.03	1.47±0.01	17.2
18307	2017.713	9.95	1.40±0.01	16.6
18308	2018.128	9.99	1.39±0.01	16.7
18309	2018.692	9.76	1.38±0.01	16.7
21578	2019.406	5.01	1.29±0.02	15.9
21579	2020.051	5.07	1.29±0.02	16.2
21580	2021.261	5.09	1.30±0.02	16.9

NOTE—Col. 3 exposure times include compensation for dead-time. Col. 4 count rates were adjusted for the 95% encircled energy of the $r = 1.''5$ detect cell. Cited uncertainties reflect Poisson noise. Col. 5 X-ray luminosities (0.1–2.4 keV) were calculated from the count rates using optimized ECFs, $d = 3.514$ pc (from the Hipparcos ϖ: van Leeuwen 2007), and including a correction for the time-dependent sensitivity decline of HRC-I (2 % per year since 2010; constant prior to 2010).

B. ADDITIONAL EXAMPLES OF STIS AND COS SPECTRAL FITS

This appendix provides additional examples of emission profile fits for selected STIS spectra of α Cen A, α Cen B, Procyon, and ϵ Eridani (Figures B1a–B1d, respectively); and COS spectra of 70 Oph B and ξ Boo B (Figs. B1e and B1f). The specific STIS epochs were chosen from the deepest medium-resolution FUV echelle exposures (E140M-1425) through the $0.''2\times0.''2$ photometric aperture, to provide the highest S/N for illustrative purposes. Nevertheless, all the STIS exposures of α Cen AB and Procyon are of high quality, thanks to the excellent photometric throughput and well-calibrated wavelength scales of the FUV echelles when applied to bright stars. On the other hand, the first STIS exposure of ϵ Eridani (illustrated here in Fig. B1d) is of better quality than the second, because the latter had half the exposure duration, and an additional ~ 50 % decrease in throughput from use of the narrow spectroscopic slit, which can suffer light losses due to telescope "breathing."

Weak central reversals appear in the high-chromosphere C II 1335 Å profile in the medium-resolution STIS spectra of α Cen A and B, and even more conspicuously in Procyon. The α Cen A tracing at Fe XXI, an important coronal forbidden line that nevertheless is expected to be absent in the cool ($\sim$ 1 MK) corona of the low-activity dwarf, clearly showcases the C I 1354 Å blend to the red; and the Procyon spectrum in that region, dominated by the FUV continuum, might even have the carbon line in absorption.

The STIS spectrum of ϵ Eri reveals a curious broad negative-flux absorption dip in the blue wing of Si III 1206 Å. This is an artifact due to a scattered light streak from the intense Lyα feature nearby, that cuts across the adjacent echelle orders at an angle, and affects the interorder background correction at roughly $\pm$10 Å from the Lyα center. The same background feature appears in many of the α Cen AB STIS E140M spectra, but is less obvious in Figs. B1a and B1b, here, because the fitting bandpass was intentionally truncated on the blue side of 1206 Å to avoid the affected wavelengths (the negative fluxes were zeroed out in those displays). Procyon does not exhibit the effect to the same degree, because its Lyα feature is intrinsically broader than those of the α Cen dwarfs, and the bright core of the hydrogen line is somewhat more absorbed, leading to a lower contrast emission profile and a more washed-out scattered light feature. In the case of ϵ Eri, the $\Delta\lambda$ limits were chosen to be the same as for the more numerous COS spectra, for the sake of consistency, so the scattered light feature blueward of 1206 Å appears in the fitting bandpass. The influence was inconsequential, however, because the pseudo-Gaussian algorithm ignores negative fluxes (below the adopted continuum level).

Figure B1. Additional examples of spectral fits for STIS and COS pointings on the Reference stars from specific epochs (rather than the epoch-average spectra illustrated routinely in previous papers of this Series). See Fig. 10 caption for details. For the STIS spectra, the highlighted points (dark dots) represent only every third native wavelength bin. (a) α Cen A (STIS: 2011 May); (b) α Cen B (STIS: 2011 May); (c) Procyon (STIS: 2011 April); (d) ϵ Eri (STIS: 2000 March; compare with a COS spectrum, Fig. 10c, in the main text); (e) ξ Boo B (COS: 2020 February); (f) 70 Oph B (COS: 2020 July).

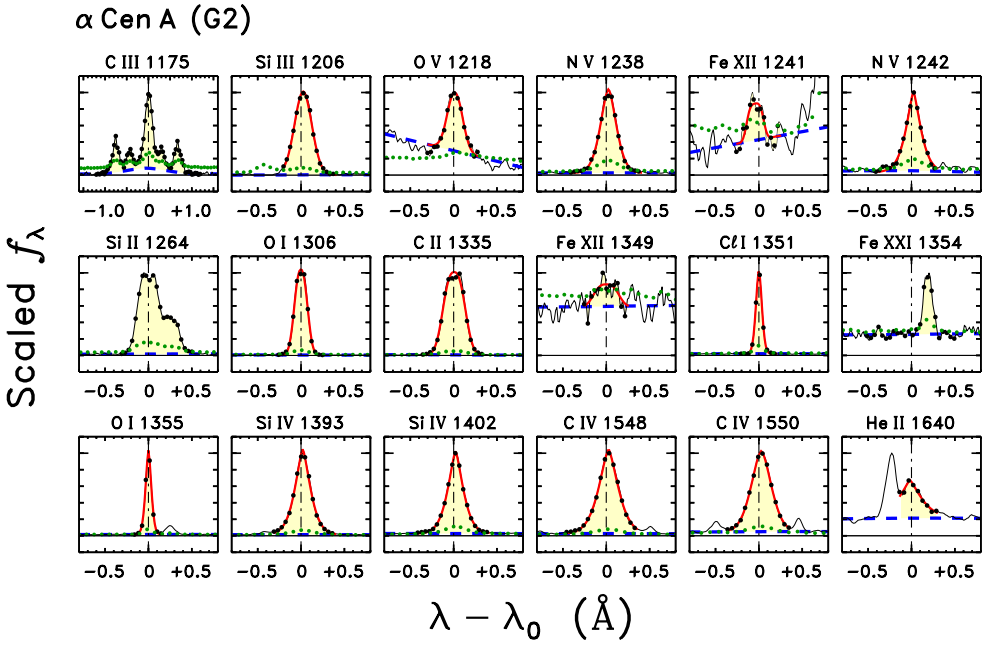

Figure B1a.

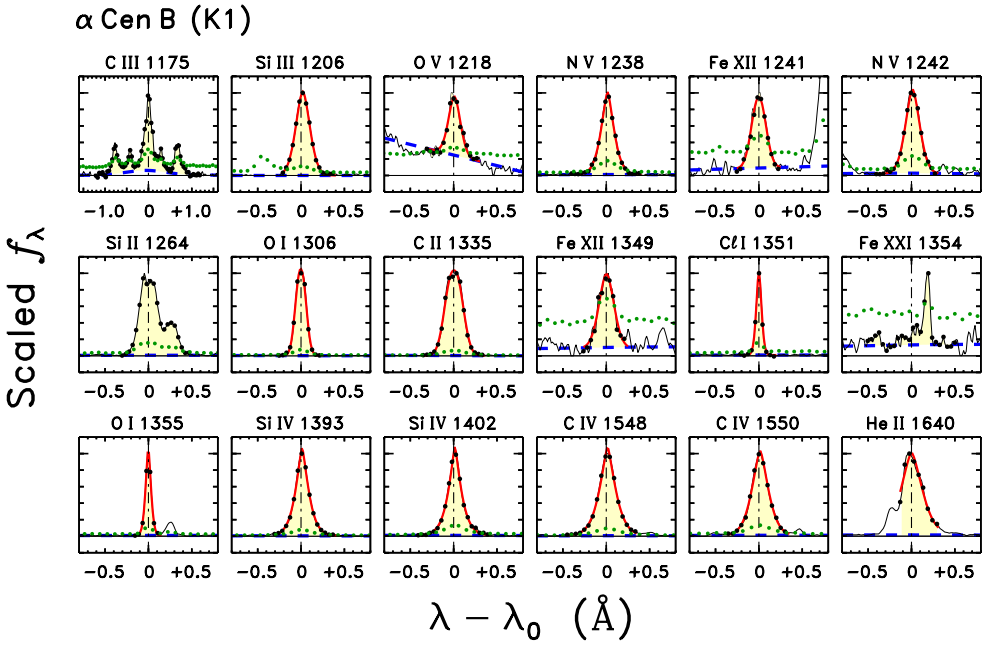

Figure B1b.

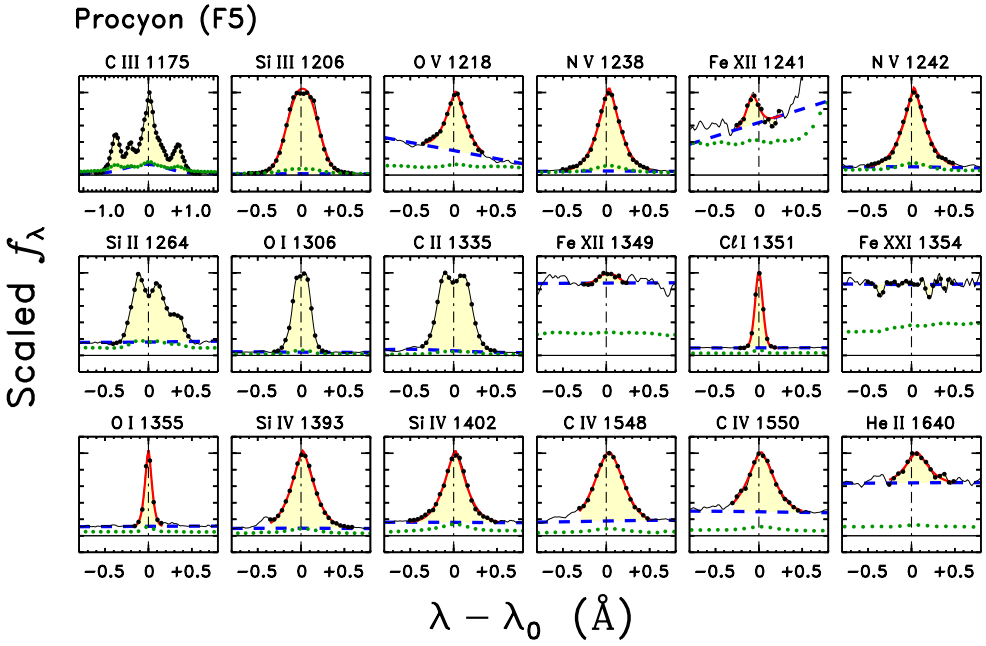

Figure B1c.

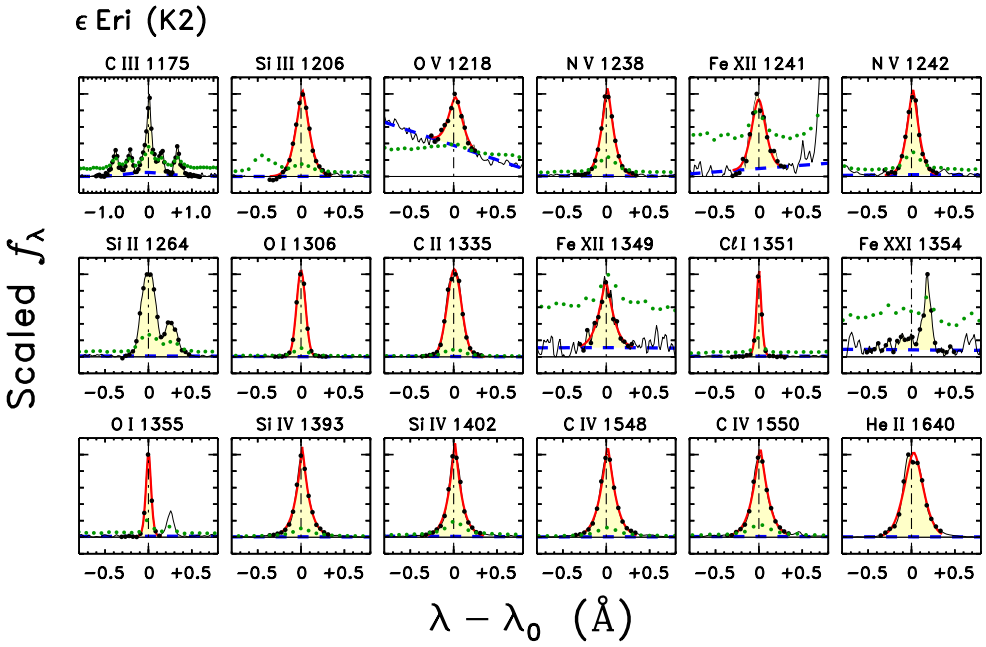

Figure B1d.

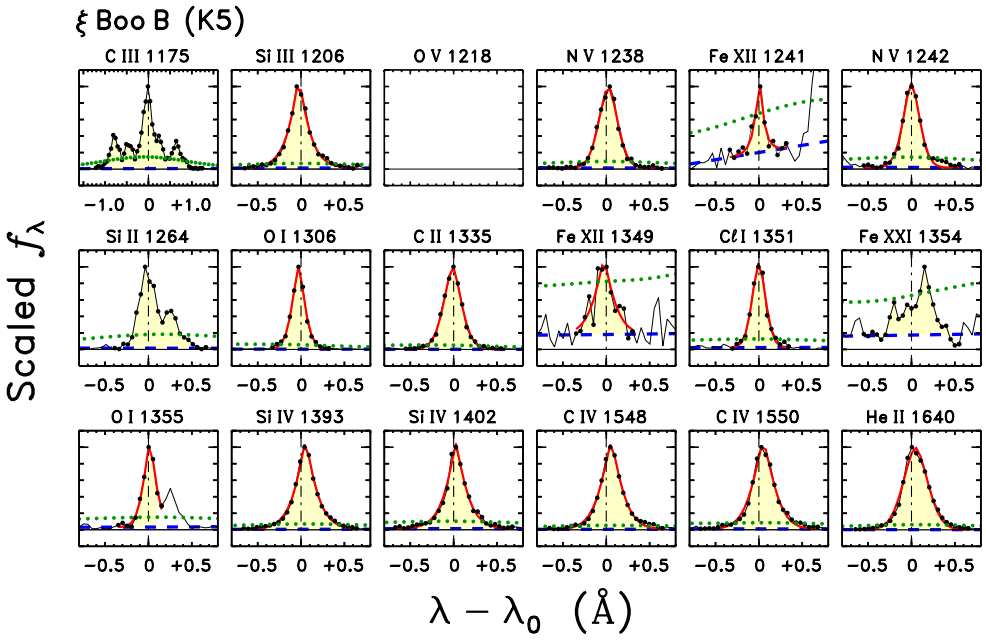

Figure B1e.

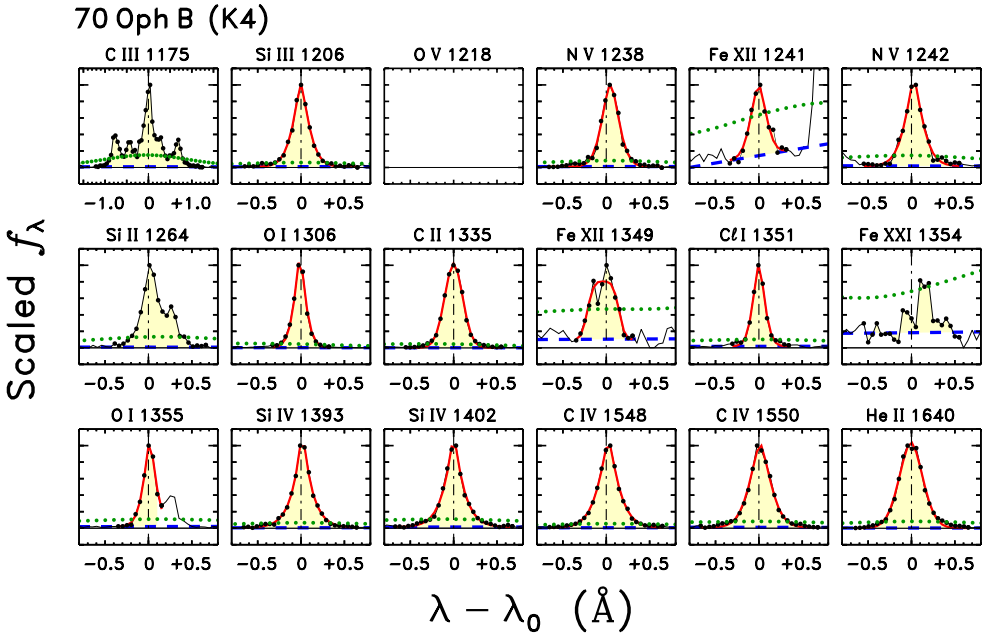

Figure B1f.

C. SUMMARY OF AVAILABLE ROTATION PERIODS FOR TOTAL ECLIPSS SAMPLE, FROM PHOTOMETRY AND LINE BROADENING

This Appendix provides further details concerning the summary rotation measures presented earlier in Table 9. Rotation periods from the TESS analysis of the present work, or from the HK Project (or other photometric sources), are considered the gold standard here. Projected rotational velocities are also summarized. A $v \sin i$ can help corroborate a rotation period, especially if the $\sin i$ factor of the star can be guessed from auxiliary information, say a visual binary orbit. In some cases, a reliable photometric period was not available from contemporary or historical records, often because a low-activity star might not have displayed sufficient rotational modulation contrast during a particular observational effort (for example, the Donahue et al. (1996) differential rotation study, which involved dedicated measurements of selected stars over several-week intervals each year for a decade, as part of the HK Project). In the (two) cases for which only an average $v \sin i$ was available (Procyon, α Cen A), the derived rotational period becomes sensitive to uncertainties in the stellar inclination. Fortunately, in both cases the stars are in visual binary systems of known orbital inclination, and thus the uncertainty mainly becomes a question of how well the stellar spin is aligned to the orbital axis. Finally, in one case—70 Oph B—there was not a reliable HK photometric period available (only an estimate from the Ca II rotation-activity connection: Baliunas et al. 1996); the likely period (more than a month) is out of reach with TESS; and there were no reasonable high-resolution $v \sin i$ measurements (especially challenging because the estimated $v_{\rm ROT}$ is less than 1 km s^{-1}). The HK flux-derived period reluctantly was adopted here, for lack of alternatives, but the corresponding point was flagged in the rotation-related diagrams to emphasize that the rotation measure is indirect. 70 Oph B was retained in these diagrams, nevertheless, because it is one of the key "Cycles" stars to illustrate possible long-term variability in coronal soft X-rays and FUV emission lines.

Table C1 summarizes the curated $P_{\rm ROT}$ and $v \sin i$ measurements, and abbreviated references to the original sources. An effort was made to retain unique values, not just duplicates repeated in subsequent studies. There are relatively few entries for the more distant, fainter, and generally more anonymous EclipSS subsample members; but usually many more values for the nearer, brighter Reference stars and Related objects. Multiple measurements, where available, were averaged to provide the summary $P_{\rm ROT}$ and $v_{\rm ROT}$ values listed in previous Table 9. In some cases, the measurements are divided into two groups. The first is a list of "preferred" values. The second is a list of values that were deprecated for one reason or another, usually because a spectroscopic line broadening was inconsistently large compared to a measured rotation period, typically because the spectral resolution was too low to yield a sensible value (in essence, the rotation period was used as a Bayesian prior to weed out nonsensical $v \sin i$ estimates). In the specific situation of the Donahue et al. (1996) and Baliunas et al. (1996) HK rotation periods, which were based on essentially the same observational material, generally the former were preferred, because the values were quoted with ranges (due mainly to differential rotation).

The adopted values of $P_{\rm ROT}$ and $v \sin i$ are italicized in the table. For each $P_{\rm ROT}$ there is a companion $v_{\rm ROT}$ in the adjacent column to the right, derived using the estimated stellar radius (listed in the cut-in heading for reference) according to:

$$v_{\rm ROT} \sim \frac{50.5}{P_{\rm ROT}} R_\star \ , \tag{C1}$$

where $v_{\rm ROT}$ is in km s^{-1}, $P_{\rm ROT}$ is in d, and the stellar radius, $R_\star$, is in solar units.

For each adopted $v \sin i$, a companion $v_{\rm ROT}$ is listed in the adjacent column to the right, based on an estimated inclination (usually from a visual binary orbit), but no entry if the inclination could not be estimated. In the two cases mentioned earlier for which only a $v \sin i$ is available, the corresponding $P_{\rm ROT}$ is listed in the Period column (Col. 1), but in parentheses. A cursory examination of the table finds many cases where the TESS or HK period is consistent with a measured $v \sin i$ (or derived $v_{\rm ROT}$, if $\sin i$ could be estimated). There are other cases where the $v \sin i$ is larger than expected from the $P_{\rm ROT}$, and, again, many of these inconsistencies can be traced to insufficient spectral resolution.

The abbreviated references of Table C1 are spelled out in the companion Table C2, together with additional notes concerning the observatories and resolving powers of the facility instruments used in each study.

Table C1. Total EclipSS Rotation Details

$P_{\rm ROT}$ (d)	Ref(P)	$v_{\rm ROT}$ (km s^{-1})	$v \sin i$ (km s^{-1})	Ref($v \sin i$)	$v_{\rm ROT}$ (km s^{-1})	Notes
1	2	3	4	5	6	7
HD 24636		SpTyp= F3 V	$R/R_\odot = 1.39$		Tuc-Hor Assoc: (10–30 Myr) (Ell14)	
0.82±0.03	∗	*86±3*				Broad FUV lines
0.839	Des21	···				
HD 38459		SpTyp= K1 V	$R/R_\odot = 0.85$			
10.2±0.4	∗	*4.2±0.2*				
			4.0±0.1	Iva17		
			4.1±0.1	Sot18		
			4.1±0.1			
			4	Nor04		
HD 39755		SpTyp= F2 V	$R/R_\odot = 1.43$			
1.16±0.04	∗	*62±2*				Broad FUV lines
HD 41004		SpTyp= K2 V (+dM)	$R/R_\odot = 0.93$			
1.30±0.05	∗	*36±1*				$v_{\rm ROT}$ for K2 primary
20–30	San02, Hen96	1.6–2.4				
			1.2	San02		

Table C1 *continued on next page*

Table C1 *(continued)*

$P_{\rm ROT}$ (d)	Ref(P)	$v_{\rm ROT}$ (km s^{-1})	$v \sin i$ (km s^{-1})	Ref($v \sin i$)	$v_{\rm ROT}$ (km s^{-1})	Notes
1	2	3	4	5	6	7
			1.0±1.2	Tor06		
			1.1±0.1			
			2	Nor04		
		HD 62850	SpTyp= G3 V		$R/R_\odot$ = 1.06	
3.7±0.1	∗	*14.5±0.4*				
3.66±0.11	Des15					
			14.3±1.0	Des15		
			15±1	Cut02		
			14	Nor04		
		HD 150706	SpTyp= G0 V		$R/R_\odot$ = 0.97	
10.0±0.2	∗	*4.9±0.1*				
			3.2	Bre16		
			6.1	Luc17		
			4.7±1.5			
			4.5±1	Sod82		
			4	Nor04		
			10	Whi07		
		HD 156559	SpTyp= F2 V		$R/R_\odot$ = 1.43	
0.62±0.03	∗	*116±6*				Very broad FUV lines
		HD 172669	SpTyp= G3 V		$R/R_\odot$ = 0.98	
9.5±0.2	∗	*5.2±0.1*				
	HD 180712	SpTyp= G1 V		$R/R_\odot$ = 0.99		Hyades stream/field (Pom11)
6.3±0.5	∗	*7.9±0.6*				
			3	Nor04		

Table C1 *continued on next page*

Table C1 *(continued)*

$P_{\rm ROT}$ (d)	Ref(P)	$v_{\rm ROT}$ (km s^{-1})	$v \sin i$ (km s^{-1})	Ref($v \sin i$)	$v_{\rm ROT}$ (km s^{-1})	Notes
1	2	3	4	5	6	7
		HD 185239	SpTyp= F5 V		$R/R_\odot = 1.35$	
2.3±0.3	∗	*30±4*				
			5	Nor04		
		HD 10700 (τ Cet)	SpTyp= G8 V		$R/R_\odot = 0.92$	
34.5	Saa97	*1.3*				
34	Bal96					
			1.1	Rue97		($\xi_{\rm mac} = 3.7$, $\xi_{\rm mic} = 1.0$)
			1.1	Saa97		
			1.8±0.1	Rei03		
			1.3	Val05		
			1.6	Jen11		
			1.0	Sis16		
			1.3±0.3			
			3.5	Sch09		
			3.3	Mar10		
			0.1	Bre16		
			3.6	Luc17		
			0.5	Cos20		
			0.6±0.8	Fek97		
		HD 20630 (κ Cet)	SpTyp= G5 V		$R/R_\odot = 0.97$	
9.2±0.3	Don96					
9.1±0.1	Gai00					
9.0±0.2	Hem16					
9.0±0.1	Ols18					
9.1±0.1		*5.4±0.1*				
9	Bal96					
			3.9±0.8	Fek97		
			4.5±0.3	Saa97		

Table C1 *continued on next page*

Table C1 *(continued)*

$P_{\rm ROT}$ (d)	Ref(P)	$v_{\rm ROT}$ (km s^{-1})	$v \sin i$ (km s^{-1})	Ref($v \sin i$)	$v_{\rm ROT}$ (km s^{-1})	Notes
1	2	3	4	5	6	7
			4.5±0.6	Gai00		
			5.2	Val05		
			5.7	Sch09		
			5.9	Mar10		
			5.2	Mis12		
			6.1	Luc17		
			4.5	Chav19		
			5.1±0.7			
HD 39587 (χ^1 Ori) SpTyp= G0 V (+dM) $R/R_\odot$ = 1.03						
5.4±0.4	Don96					
5.14±0.01	Hem16					
5.3±0.2		*9.8±0.4*				
5	Bal96					
			8.6±0.8	Fek97		
			8.2±0.1	Rei03		
			9.8	Val05		
			10.8	Mar10		
			8.9	Bre16		
			10.5	Luc17		
			9.5±1.0			
HD 72905 (π^1 UMa) SpTyp= G1 V $R/R_\odot$ = 0.97 UMa Stream						
4.7±0.1	Don96					
5.0±0.3	Gai00					
5.23±0.02	Hem16					
5.0±0.2		*9.8±0.4*				
5	Bal96					
			8.5±0.4	Gra84		
			9.7±0.4	Sod93		
			9.5±0.8	Fek97		
			8.7±0.6	Gai00		

Table C1 *continued on next page*

Table C1 *(continued)*

$P_{\rm ROT}$ (d)	Ref(P)	$v_{\rm ROT}$ (km s^{-1})	$v \sin i$ (km s^{-1})	Ref($v \sin i$)	$v_{\rm ROT}$ (km s^{-1})	Notes
1	2	3	4	5	6	7
			9.7	Mon01		
			9.7±1.0	Lop10		
			11.2	Mar10		
			9.6	Bre16		
			10.4	Luc17		
			9.6	Chav19		
			9.7±0.7			
HD 129333 (EK Dra) SpTyp= G2 V (+dM) $R/R_\odot = 0.98$						
2.8±0.3	Don96					
2.62±0.01	Hem16					
2.61±0.00	Jar18					
2.7±0.1		*18.3±0.7*				
3	Bal96					
			17.3	Mon01		
			16.8	Val05		
			19.7±1.0	Lop10		
			17.4	Bre16		
			17.5	Jar18		
			17.7±1.0			
			17	Nor04		
			23±2	Whi07		2 epochs
Sun SpTyp= G2 V $R/R_\odot = 1.00$ $i = 90°$						
25.4±1.0		*2.0±0.1*				Carrington, sidereal
22.9–26.6	Don96	1.9–2.2				sidereal
			2.1	Rue97	2.1	sidereal; ($\xi_{\rm mac} = 3.4$, $\xi_{\rm mic} = 1.0$)
			2.0±0.8	Saa97	2.0	sidereal; ($\xi_{\rm mac} = 2.8$, $\xi_{\rm mic} = 1.0$)
			1.8	Val05	1.8	sidereal; ($\xi_{\rm mac} = 4.0$, $\xi_{\rm mic} = 0.9$)
HD 22049 (ϵ Eri) SpTyp= K2 V $R/R_\odot = 0.81$ $i = 46°$ (Jef14)						

Table C1 *continued on next page*

Table C1 *(continued)*

$P_{\rm ROT}$ (d)	Ref(P)	$v_{\rm ROT}$ (km s^{-1})	$v \sin i$ (km s^{-1})	Ref($v \sin i$)	$v_{\rm ROT}$ (km s^{-1})	Notes
1	2	3	4	5	6	7
~~11.7±0.6~~	~~Don96~~					
11.5±0.1	Cro06					2 spot periods (different latitudes)
11.2	Gig16					modeling RV data and photometry
11.8±0.1	Hem16					
11.1±0.2	Ols18					
11.5±0.3		*3.6±0.1*				
12	Bal96					
			2.2±0.4	Gra84		
			2.0±0.8	Fek97		
			2.4	Val05		
			2.2	Bre16		
			2.9±0.5	Gig16		
			2.2±0.3	Hoj19		
			2.3±0.3		*3.2±0.4*	
			1.6	Rue97		($\xi_{\rm mac} = 4.3$, $\xi_{\rm mic} = 1.0$)
			1.6	Saa97		($\xi_{\rm mac} = 1.7$, $\xi_{\rm mic} = 1.0$)
			4.6	Sch09		
			4.1	Mart10		
			2.4	Chav19		
HD 61421 (α CMi A: Procyon))		SpTyp= F5 IV-V		$R/R_\odot = 2.03$		$i = 31.4°$ (orbit)
			2.8±0.3	Gra84		
			2.0±0.8	Fek97		
			3.2±0.5	All02		possibly 2.7 km s^{-1} (3D effects)
			2.8	Bru10		
(19±2)			*2.8±0.3*		*5.4±0.6*	$P_{\rm ROT}$ from $v_{\rm ROT}$
			5.7	Val05		
			3.9	Sch09		
			5.4	Mar10		
			7.4	Luc17		
HD 128620 (α Cen A)		SpTyp= G2 V		$R/R_\odot = 1.22$		$i = 79°$ (orbit)
29	Hal91					

Table C1 *continued on next page*

Table C1 *(continued)*

$P_{\rm ROT}$ (d)	Ref(P)	$v_{\rm ROT}$ (km s^{-1})	$v \sin i$ (km s^{-1})	Ref($v \sin i$)	$v_{\rm ROT}$ (km s^{-1})	Notes
1	2	3	4	5	6	7
			2.7	Rue97		($\xi_{\rm mac} = 4.9$, $\xi_{\rm mic} = 1.0$)
			2.7±0.7	Saa97		
			2.3	Val05		
			1.9±0.6	Bru10		
			2.6	Mart0		
(26±3)			*2.4±0.3*		*2.4±0.3*	$P_{\rm ROT}$ from $v_{\rm ROT}$
			4.5	Sch09		
	HD 128621	(α Cen B)	SpTyp= K1 V		$R/R_\odot = 0.86$	$i = 79°$ (orbit)
43	Char93					HK profile and flux modulations
42	Saa97					HK modulation
36±1	Dew10					
38±2	Dum12					RV modulation
40±3		*1.1±0.1*				
			1.2	Rue97		($\xi_{\rm mac} = 4.1$, $\xi_{\rm mic} = 0.9$)
			1.1±0.8	Saa97		
			0.9	Val05		
			1.0±0.6	Bru10		($\xi_{\rm mac} = 4.1$, $\xi_{\rm mic} = 0.9$)
			1.1±0.1		*1.1±0.1*	
			4.9	Sch09		
			3.5	Mar10		
	HD 131156A	(ξ Boo A)	SpTyp= G7 V		$R/R_\odot = 0.84$	$i = 140°$ (orbit)
6.3±0.3	Don96					
6.30±0.04	Hem16					
6.00±0.04	Ols18					
6.2±0.1		*6.8±0.1*				
6	Bal96					
			2.9±0.4	Gra84		
			3.2±0.8	Fek97		
			3.9±0.3	Rei03		
			4.6	Val05		

Table C1 *continued on next page*

Table C1 *(continued)*

$P_{\rm ROT}$ (d)	Ref(P)	$v_{\rm ROT}$ (km s^{-1})	$v \sin i$ (km s^{-1})	Ref($v \sin i$)	$v_{\rm ROT}$ (km s^{-1})	Notes
1	2	3	4	5	6	7
			3.3	Mar10		
			4.4	Bre16		
			3.7±0.6		*5.8±0.9*	
			6.0	Luc17		
	HD 131156B	(ξ Boo B)	SpTyp= K5 V		$R/R_\odot = 0.67$	$i = 140°$ (orbit)
11.9±1.1	Don96	*2.8±0.3*				
11	Bal96					
			5.1	Luc17		
	HD 165341A	(70 Oph A)	SpTyp= K0 V		$R/R_\odot = 0.86$	$i = 121°$ (orbit)
19.7	Noy84					
19.3±0.3	Ols18					
19.5±0.3		*2.23±0.03*				
20	Bal96					
			1.6±0.4	Gra84		
			3.1±0.8	Fek97		
			4.1	Mar10		
			2.6	Bre16		
			4.3	Luc17		
			3.1±1.0		*3.6±1.2*	
			4.6	Sch09		
			0.9	Bru10		outlier
	HD 165341B	(70 Oph B)	SpTyp= K4 V		$R/R_\odot = 0.72$	$i = 121°$ (orbit)
(34)	Bal96:	(1.1)				P from HK rotation-activity
(12)			2.1	Mor19	2.5	APO lower-R

Table C1 *continued on next page*

Table C1 *(continued)*

$P_{\rm ROT}$	Ref(P)	$v_{\rm ROT}$	$v \sin i$	Ref($v \sin i$)	$v_{\rm ROT}$	Notes
(d)		(km s^{-1})	(km s^{-1})		(km s^{-1})	
1	2	3	4	5	6	7

NOTE—Col. 1 is the photometric rotation period. Col. 2 is an abbreviated reference for that period (Table C2). Col. 3 is the associated rotational velocity. Col. 4 is the spectroscopic projected rotational velocity. Col. 5 is an abbreviated reference for the $v \sin i$ (Table C2). Col. 6 is the associated rotational velocity, if the inclination, i, could be estimated (e.g., from a visual orbit). Col. 7 lists any special notes for the value(s) in that row.

Table C2. References for Table C1

Abbrev.	Citation	Notes
$*$	TESS (this work)	
All02	Allende-Prieto et al. (2002)	McDonald 2dcoude: $R = 200{,}000$
Bal96	Baliunas et al. (1996)	Mt. Wilson: HK modulation
Bre16	Brewer et al. (2016)	Keck HIRES: $R = 70{,}000$
Bru10	Bruntt et al. (2010)	ESO HARPS: $R = 115{,}000$
Char93	Char et al. (1993)	ESO Coude Echelle: $R = 80{,}000$
Chav19	Chavero et al. (2019)	ESO FEROS: $R = 48{,}000$
Cos20	Costa-Silva et al. (2020)	ESO HARPS: $R = 115{,}000$
Cro06	Croll et al. (2006)	MOST photometry
Cut02	Cutispoto et al. (2002)	ESO Coude Echelle: $R = 80{,}000$; also, CORAVEL: $R = 20{,}000$
Des15	Desidera et al. (2015)	various (FEROS, HARPS, CORALIE)
Des21	Desidera et al. (2021)	TESS (in support of SHINE: SpHere INfrared survey for Exoplanets)
Dew10	DeWarf et al. (2010)	IUE SWP-LO: FUV modulation
Don96	Donahue et al. (1996)	Mt. Wilson: HK modulation
Dum12	Dumusque et al. (2012)	ESO HARPS: $R = 115{,}000$
Ell14	Elliott et al. (2014)	Search for Associations Containing Young Stars (SACY) V.
Fek97	Fekel (1997)	KPNO coude feed spectrograph: $R = 31{,}000$
Gai00	Gaidos et al. (2000)	Fairborn APT: optical photometry
Gig16	Giguere et al. (2016)	CTIO CHIRON: $R = 80{,}000$–$140{,}000$; MOST + APT photometry
Gra84	Gray (1984)	McDonald coude spectrograph: $R = 120{,}000$
Hal91	Hallam et al. (1991)	IUE SWP-LO: FUV modulation
Hem16	Hempelmann et al. (2016)	La Luz TIGRE: $R = 20{,}000$; HK modulation
Hen96	Henry et al. (1996)	CTIO Cassegrain spectrograph: $R = 2{,}500$; HK fluxes
Hoj19	Hojjatpanah et al. (2019)	ESO HARPS: $R = 115{,}000$
Iva17	Ivanyuk et al. (2017)	ESO HARPS: $R = 115{,}000$
Jar18	Jarvinen et al. (2018)	Fairborn Observatory APT: optical photometry
Jen11	Jenkins et al. (2011)	ESO FEROS: $R = 48{,}000$

Table C2 *continued on next page*

Table C2 *(continued)*

Abbrev.	Citation	Notes
Lop10	Lopez-Santiago et al. (2010)	various echelle spectrographs: R = 30,000–60,000
Luc17	Luck et al. (2017)	McDonald Cassegrain echelle spectrograph: R = 60,000
Mar10	Martinez-Arnaiz et al. (2010)	various echelle spectrographs: R = 40,000–57,000
Mis12	Mishenina et al. (2012)	OHP ELODIE: R = 42,000
Mon01	Montes et al. (2001)	various echelle spectrographs: R = 30,000–50,000
Mor19	Morris et al. (2019)	APO ARCES: R = 32,000
Nor04	Nordstrom et al. (2004)	CORAVEL (N+S): R = 20,000 ($v \sin i$ quoted to nearest km s^{-1})
Noy84	Noyes et al. (1984)	Mt. Wilson: HK modulation
Ols18	Olspert et al. (2018)	Mt. Wilson: HK modulation
Pom11	Pompeia et al. (2011)	Chemically Tagging the Hyades Stream
Rei03	Reiners & Schmitt (2003)	ESO Ces: R = 235,000 (highest resolution mode)
Rue97	Rueedi et al. (1997)	ESO Ces: R = 100,000
Saa97	Saar & Osten (1997)	ESO Ces: R = 100,000
San02	Santos et al. (2002)	CORALIE (R = 47,000) for $v \sin i$; HK rotation-activity for $P_{\rm ROT}$
Sch09	Schröder et al. (2009)	ESO FEROS: R = 48,000
Sis16	Sissa et al. (2016)	TNG SARG: R = 144,000
Sod82	Soderblom (1982)	Lick coude echelle spectrograph: R = 115,000
Sod93	Soderblom & Mayor (1993)	CORAVEL: R = 20,000
Sot18	Soto et al. (2018)	various echelle spectrographs: $R > 40{,}000$
Tor06	Torres et al. (2006)	FEROS, CORLIE: $R \sim$ 50,000; SACY I (young stars catalog)
Val05	Valenti & Fischer (2005)	various echelle spectrographs: R = 60,000–100,00
Whi07	White et al. (2007)	Palomar facility spectrograph in echelle mode: R = 16,000

NOTE—*Catalog of Stellar Rotational Velocities* (Glebocki et al. 2005) was the source of many of the pre-2005 entries.

REFERENCES

Airapetian, V. S., Barnes, R., Cohen, O., et al. 2020, International Journal of Astrobiology, 19, 136. doi:10.1017/S1473550419000132

Allende Prieto, C., Asplund, M., García López, R. J., et al. 2002, ApJ, 567, 544. doi:10.1086/338248

Ayres, T. R. 1997, J. Geophys. Res., 102, 1641. doi:10.1029/96JE03306

Ayres, T. R. 2014, AJ, 147, 59. doi:10.1088/0004-6256/147/3/59

Ayres, T. R. 2015, AJ, 150, 7. doi:10.1088/0004-6256/150/1/7

Ayres, T. R. 2020, ApJS, 250, 16. (Paper I) doi:10.3847/1538-4365/aba3c6

Ayres, T. R. 2021b, ApJ, 908, 205. (Paper II) doi:10.3847/1538-4357/abd095

Ayres, T. R. 2021a, ApJ, 910, 71. (Paper III) doi:10.3847/1538-4357/abd7a2

Ayres, T. R. 2021d, ApJ, 923, 192. (Paper V) doi:10.3847/1538-4357/ac1fec

Ayres, T. & Buzasi, D. 2021, Research Notes of the American Astronomical Society, 5, 243. doi:10.3847/2515-5172/ac3255

Ayres, T. & France, K. 2010, ApJL, 723, L38. doi:10.1088/2041-8205/723/1/L38

Ayres, T. R., Fleming, T. A., Simon, T., et al. 1995, ApJS, 96, 223. doi:10.1086/192118

Ayres, T. R., Brown, A., Harper, G. M., et al. 2003, ApJ, 583, 963. doi:10.1086/345409

Ayres, T. R., Judge, P. G., Saar, S. H., et al. 2008, ApJL, 678, L121. doi:10.1086/588581

Ayres, T., De Pontieu, B., & Testa, P. 2021, ApJ, 916, 36. (Paper IV) doi:10.3847/1538-4357/abfa92

Baliunas, S., Sokoloff, D., & Soon, W. 1996, ApJL, 457, L99. doi:10.1086/309891

Bressan, A., Marigo, P., Girardi, L., et al. 2012, MNRAS, 427, 127. doi:10.1111/j.1365-2966.2012.21948.x

Brewer, J. M., Fischer, D. A., Valenti, J. A., et al. 2016, ApJS, 225, 32. doi:10.3847/0067-0049/225/2/32

Bruntt, H., Bedding, T. R., Quirion, P.-O., et al. 2010, MNRAS, 405, 1907. doi:10.1111/j.1365-2966.2010.16575.x

Buzasi, D. 2018, 20th Cambridge Workshop on Cool Stars, Stellar Systems and the Sun, id.66. doi:10.5281/zenodo.1481994

Carlsson, M. & Stein, R. F. 1992, ApJL, 397, L59. doi:10.1086/186544

Casagrande, L., Lin, J., Rains, A. D., et al. 2021, MNRAS, 507, 2684. doi:10.1093/mnras/stab2304

Casagrande, L. & VandenBerg, D. A. 2014, MNRAS, 444, 392. doi:10.1093/mnras/stu1476 (BC data reported in: Casagrande, L. & VandenBerg, D. A. 2018, Astrophysics Source Code Library. ascl:1805.022)

Char, S., Foing, B. H., Beckman, J., et al. 1993, A&A, 276, 78

Chavero, C., de la Reza, R., Ghezzi, L., et al. 2019, MNRAS, 487, 3162. doi:10.1093/mnras/stz1496

Coffaro, M., Stelzer, B., Orlando, S., et al. 2020, A&A, 636, A49. doi:10.1051/0004-6361/201936479

Corsaro, E., Bonanno, A., Mathur, S., et al. 2021, A&A, 652, L2. doi:10.1051/0004-6361/202141395

Costa Silva, A. R., Delgado Mena, E., & Tsantaki, M. 2020, A&A, 634, A136. doi:10.1051/0004-6361/201936523

Croll, B., Walker, G. A. H., Kuschnig, R., et al. 2006, ApJ, 648, 607. doi:10.1086/505792

Cutispoto, G., Pastori, L., Pasquini, L., et al. 2002, A&A, 384, 491. doi:10.1051/0004-6361:20020040

Delorme, P., Collier Cameron, A., Hebb, L., et al. 2011, MNRAS, 413, 2218. doi:10.1111/j.1365-2966.2011.18299.x

De Pontieu, B., Title, A. M., Lemen, J. R., et al. 2014, SoPh, 289, 2733

Desidera, S., Covino, E., Messina, S., et al. 2015, A&A, 573, A126. doi:10.1051/0004-6361/201323168

Desidera, S., Chauvin, G., Bonavita, M., et al. 2021, A&A, 651, A70. doi:10.1051/0004-6361/202038806

DeWarf, L. E., Datin, K. M., & Guinan, E. F. 2010, ApJ, 722, 343. doi:10.1088/0004-637X/722/1/343

Donahue, R. A., Saar, S. H., & Baliunas, S. L. 1996, ApJ, 466, 384. doi:10.1086/177517

Douglas, S. T., Curtis, J. L., Agüeros, M. A., et al. 2019, ApJ, 879, 100. doi:10.3847/1538-4357/ab2468

Dudík, J., Dzifčáková, E., Meyer-Vernet, N., et al. 2017, SoPh, 292, 100. doi:10.1007/s11207-017-1125-0
Dumusque, X., Pepe, F., Lovis, C., et al. 2012, Nature, 491, 207. doi:10.1038/nature11572
Elliott, P., Bayo, A., Melo, C. H. F., et al. 2014, A&A, 568, A26. doi:10.1051/0004-6361/201423856
Favata, F., Micela, G., Orlando, S., et al. 2008, A&A, 490, 1121. doi:10.1051/0004-6361:200809694
Fekel, F. C. 1997, PASP, 109, 514. doi:10.1086/133908
Feldman, U., Doschek, G. A., & Cohen, L. 1982, ApJ, 255, 325. doi:10.1086/159833
Gaidos, E. J., Henry, G. W., & Henry, S. M. 2000, AJ, 120, 1006. doi:10.1086/301488
Giguere, M. J., Fischer, D. A., Zhang, C. X. Y., et al. 2016, ApJ, 824, 150. doi:10.3847/0004-637X/824/2/150
Glebocki, R. & Gnacinski, P. 2005, VizieR Online Data Catalog, III/244
Gray, D. F. 1976, A Wiley-Science Publication, New York: Wiley, 1976
Gray, D. F. 1984, ApJ, 281, 719. doi:10.1086/162149
Güdel, M., Guinan, E. F., & Skinner, S. L. 1997, ApJ, 483, 947. doi:10.1086/304264
Hallam, K. L., Altner, B., & Endal, A. S. 1991, ApJ, 372, 610. doi:10.1086/170005
Hartman, J. D., Bakos, G. Á., Kovács, G., et al. 2010, MNRAS, 408, 475. doi:10.1111/j.1365-2966.2010.17147.x
Hempelmann, A., Mittag, M., Gonzalez-Perez, J. N., et al. 2016, A&A, 586, A14. doi:10.1051/0004-6361/201526972
Henry, T. J., Soderblom, D. R., Donahue, R. A., et al. 1996, AJ, 111, 439. doi:10.1086/117796
Hojjatpanah, S., Figueira, P., Santos, N. C., et al. 2019, A&A, 629, A80. doi:10.1051/0004-6361/201834729
Ivanyuk, O. M., Jenkins, J. S., Pavlenko, Y. V., et al. 2017, MNRAS, 468, 4151. doi:10.1093/mnras/stx647
Järvinen, S. P., Strassmeier, K. G., Carroll, T. A., et al. 2018, A&A, 620, A162. doi:10.1051/0004-6361/201833496
Jenkins, J. S., Murgas, F., Rojo, P., et al. 2011, A&A, 531, A8. doi:10.1051/0004-6361/201016333
Johnstone, C. P., Bartel, M., & Güdel, M. 2021, A&A, 649, A96. doi:10.1051/0004-6361/202038407
Judge, P. G., Saar, S. H., Carlsson, M., et al. 2004, ApJ, 609, 392. doi:10.1086/421044
König, B., Fuhrmann, K., Neuhäuser, R., et al. 2002, A&A, 394, L43. doi:10.1051/0004-6361:20021377
König, B., Guenther, E. W., Woitas, J., et al. 2005, A&A, 435, 215. doi:10.1051/0004-6361:20040462
Kervella, P., Bigot, L., Gallenne, A., et al. 2017, A&A, 597, A137. doi:10.1051/0004-6361/201629505
Kim, Y.-C. & Demarque, P. 1996, ApJ, 457, 340. doi:10.1086/176733
Laming, J. M., Drake, J. J., & Widing, K. G. 1995, ApJ, 443, 416. doi:10.1086/175534
Landin, N. R., Mendes, L. T. S., & Vaz, L. P. R. 2010, A&A, 510, A46. doi:10.1051/0004-6361/200913015
Linsky, J. L. & Ayres, T. R. 1978, ApJ, 220, 619. doi:10.1086/155945
López-Santiago, J., Montes, D., Gálvez-Ortiz, M. C., et al. 2010, A&A, 514, A97. doi:10.1051/0004-6361/200913437
Luck, R. E. 2017, AJ, 153, 21. doi:10.3847/1538-3881/153/1/21
Martínez-Arnáiz, R., Maldonado, J., Montes, D., et al. 2010, A&A, 520, A79. doi:10.1051/0004-6361/200913725
Mishenina, T. V., Soubiran, C., Kovtyukh, V. V., et al. 2012, A&A, 547, A106. doi:10.1051/0004-6361/201118412
Montes, D., López-Santiago, J., Fernández-Figueroa, M. J., et al. 2001, A&A, 379, 976. doi:10.1051/0004-6361:20011385
Morris, B. M., Curtis, J. L., Sakari, C., et al. 2019, AJ, 158, 101. doi:10.3847/1538-3881/ab2e04
Namekata, K., Maehara, H., Honda, S., et al. 2021, Nature Astronomy. doi:10.1038/s41550-021-01532-8
Nordström, B., Mayor, M., Andersen, J., et al. 2004, A&A, 418, 989. doi:10.1051/0004-6361:20035959
Noyes, R. W., Hartmann, L. W., Baliunas, S. L., et al. 1984, ApJ, 279, 763. doi:10.1086/161945
Oetjens, A., Carone, L., Bergemann, M., et al. 2020, A&A, 643, A34. doi:10.1051/0004-6361/202038653

Olspert, N., Lehtinen, J. J., Käpylä, M. J., et al. 2018, A&A, 619, A6. doi:10.1051/0004-6361/201732525

Orlando, S., Favata, F., Micela, G., et al. 2017, A&A, 605, A19. doi:10.1051/0004-6361/201731301

Parker, E. N. 1970, ApJ, 162, 665. doi:10.1086/150697

Pevtsov, A. A., Fisher, G. H., Acton, L. W., et al. 2003, ApJ, 598, 1387. doi:10.1086/378944

Pineda, J. S., Youngblood, A., & France, K. 2021, ApJ, 911, 111. doi:10.3847/1538-4357/abe8d7

Pneuman, G. W. & Kopp, R. A. 1978, SoPh, 57, 49. doi:10.1007/BF00152043

Pompéia, L., Masseron, T., Famaey, B., et al. 2011, MNRAS, 415, 1138. doi:10.1111/j.1365-2966.2011.18685.x

Predehl, P., Andritschke, R., Babyshkin, V., et al. 2016, Proc. SPIE, 9905, 99051K. doi:10.1117/12.2235092

Rajpaul, V., Aigrain, S., & Roberts, S. 2016, MNRAS, 456, L6. doi:10.1093/mnrasl/slv164

Rebull, L. M., Stauffer, J. R., Bouvier, J., et al. 2016, AJ, 152, 113. doi:10.3847/0004-6256/152/5/113

Reiners, A. & Schmitt, J. H. M. M. 2003, A&A, 398, 647. doi:10.1051/0004-6361:20021642

Reiners, A., Schüssler, M., & Passegger, V. M. 2014, ApJ, 794, 144. doi:10.1088/0004-637X/794/2/144

Ricker, G. R., Winn, J. N., Vanderspek, R., et al. 2014, Proc. SPIE, 9143, 914320. doi:10.1117/12.2063489

Robrade, J., Schmitt, J. H. M. M., & Favata, F. 2005, A&A, 442, 315. doi:10.1051/0004-6361:20053314

Robrade, J., Schmitt, J. H. M. M., & Favata, F. 2012, A&A, 543, A84. doi:10.1051/0004-6361/201219046

Rueedi, I., Solanki, S. K., Mathys, G., et al. 1997, A&A, 318, 429

Saar, S. H. & Osten, R. A. 1997, MNRAS, 284, 803. doi:10.1093/mnras/284.4.803

Santos, N. C., Mayor, M., Naef, D., et al. 2002, A&A, 392, 215. doi:10.1051/0004-6361:20020876

Scharf, C. A. 2010, ApJ, 722, 1547. doi:10.1088/0004-637X/722/2/1547

Schröder, C., Reiners, A., & Schmitt, J. H. M. M. 2009, A&A, 493, 1099. doi:10.1051/0004-6361:200810377

Shine, R. A. 1983, ApJ, 266, 882. doi:10.1086/160835

Simon, T. & Drake, S. A. 1989, ApJ, 346, 303. doi:10.1086/168012

Sissa, E., Gratton, R., Desidera, S., et al. 2016, A&A, 596, A76. doi:10.1051/0004-6361/201628531

Soderblom, D. R. 1982, ApJ, 263, 239. doi:10.1086/160498

Soderblom, D. R. & Mayor, M. 1993, ApJL, 402, L5. doi:10.1086/186686

Soto, M. G. & Jenkins, J. S. 2018, A&A, 615, A76. doi:10.1051/0004-6361/201731533

Stepien, K. 1989, A&A, 210, 273

Torres, C. A. O., Quast, G. R., da Silva, L., et al. 2006, A&A, 460, 695. doi:10.1051/0004-6361:20065602

Valenti, J. A. & Fischer, D. A. 2005, ApJS, 159, 141. doi:10.1086/430500

van Leeuwen, F. 2007, A&A, 474, 653. doi:10.1051/0004-6361:20078357

Voges, W. 1993, Advances in Space Research, 13, 391. doi:10.1016/0273-1177(93)90147-4

Wahlstrom, C. & Carlsson, M. 1994, ApJ, 433, 417. doi:10.1086/174654

White, R. J., Gabor, J. M., & Hillenbrand, L. A. 2007, AJ, 133, 2524. doi:10.1086/514336

Wilson, O. C. 1978, ApJ, 226, 379. doi:10.1086/156618

Wood, B. E. 2018, Journal of Physics Conference Series, 1100, 012028. doi:10.1088/1742-6596/1100/1/012028

Wood, B. E., Laming, J. M., Warren, H. P., et al. 2018, ApJ, 862, 66. doi:10.3847/1538-4357/aaccf6

Wright, N. J., Drake, J. J., Mamajek, E. E., et al. 2011, ApJ, 743, 48. doi:10.1088/0004-637X/743/1/48

Youngblood, A., Pineda, J. S., Ayres, T., et al. 2022, arXiv:2201.01315

Zirin, H. 1975, ApJL, 199, L63. doi:10.1086/181849

Zucker, S., Mazeh, T., Santos, N. C., et al. 2003, A&A, 404, 775. doi:10.1051/0004-6361:20030499

Zucker, S., Mazeh, T., Santos, N. C., et al. 2004, A&A, 426, 695. doi:10.1051/0004-6361:20040384